5-2017

Spatial and Temporal Study of Heat Transport of Hydrothermal Features in Norris Geyser Basin, Yellowstone National Park

Ruba A. M. Mohamed
Utah State University

A STUDY OF SPATIAL AND TEMPORAL MASS AND HEAT TRANSPORT OF HYDROTHERMAL FEATURES IN NORRIS GEYSER BASIN, YELLOWSTONE NATIONAL PARK

by

Ruba A. M. Mohamed

A dissertation submitted in partial fulfillment
of the requirements of the degree

of

DOCTOR OF PHILOSOPHY

in

Civil and Environmental Engineering

Approved:

Christopher M. U. Neale Major Professor	Jagath J. Kaluarachchi Committee Member
David K. Stevens Committee Member	Lawrence E. Hipps Committee Member
Heng Ban Committee Member	Mark R. McLellan Vice President for Research and Dean of the School of Graduate Studies

UTAH STATE UNIVERSITY
Logan, Utah

2017

ABSTRACT

Spatial and Temporal Study of Heat Transport of Hydrothermal Features in Norris Geyser Basin, Yellowstone National Park

by

Ruba A. M. Mohamed, Doctor of Philosophy

Utah State University, 2017

Major Professor: Dr. Christopher M. U. Neale
Department: Civil and Environmental Engineering
Division: Water Resources Engineering

Monitoring the dynamic thermal activity in Yellowstone National Park is required by the United States Congress. The continuous monitoring is important to maintain the safety of the visitors and park service personnel, plan and relocate infrastructure, and study potential impact from nearby geothermal development including oil and gas industry. This dissertation is part of a study initiated in the early 2000s to monitor the thermal activity of dynamic areas within the Park, using airborne remote sensing imagery. This study was focused in Norris Geyser Basin, the hottest geyser basin in the park, located near the northwestern rim of the Yellowstone's caldera. The study is considered the first long-term comprehensive airborne remote sensing study in the basin which took place between August 2008 and October 2013. In this study, at least one 1-meter resolution thermal infrared image and three-band images (multispectral) were acquired and used to estimate year-to-year changes in radiant temperature, radiant flux, and radiant power from the thermal source in Norris.

Presence of residual radiant flux in the ground from absorbed solar radiation and atmospheric longwave radiation was the main challenge to compere year-to-year changes in the thermal activity. This residual flux is included in the total radiant flux calculated through the remote sensing images which gives false estimates of the flux generated from the underling thermal source. Two methods were suggested in Chapters 2 and 4 of this dissertation to estimate the residual radiant flux. A method was developed in Chapter 2 to estimate the residual radiant flux in a bare ground area covered with hydrothermal siliceous sinter deposit. The method compared ground-based measurements with high spatial resolution airborne remote sensing measurements to estimate the residual radiant flux. In Chapter 4, a method was developed to estimate the residual radiant flux in the six surface classes in Norris, including bare ground, bare ground with siliceous sinter deposit, lakes and pools, river, forest, and grass. The assumptions and implications of each method were discussed to suggest a reliable method to estimate the geothermal radiant flux after subtracting the absorbed residual radiant flux. Chapter 3 provides an analysis of the four components of heat flux in the ground surface, including conduction of sensible heat, convection of sensible heat by liquid water and water vapor, and convection of latent heat by water vapor. The main purpose from the analysis was to assess the hypothesis that the convection and latent heat flux are negligible which therefore supported the results obtained from the analysis in Chapters 2 and 4.

(200 pages)

PUBLIC ABSTRACT

Ruba A. M. Mohamed, Doctor of Philosophy

Monitoring thermal activity in Yellowstone National Park is required by the United States Congress to maintain the safety of the visitors and park service personnel and to protect the integrity of the park. This dissertation is part of a study initiated in the early 2000s to monitor the thermal activity in the park with focus on Norris Geyser Basin, the hottest geyser basin in the park. The study is considered the first multiple-year study in the basin which took place between August 2008 and October 2013. In this study, at least one thermal infrared image was acquired every year using airborne remote sensing tools to estimate the surface radiant temperature. The images were used to estimate and compare changes in surface radiant temperature and other radiant components including radiant flux and radiant power, which were estimated from the radiant temperature images over Norris.

To compare yearly changes in the radiant flux due to the thermal source alone, the stored solar flux was estimated and subtracted from the total radiant flux image. Two methods were suggested in this dissertation to estimate the stored solar flux which were addressed in Chapters 2 and 4. The assumptions and implications of each method were discuss to suggest a reliable method to estimate the geothermal heat flux.

ACKNOWLEDGMENTS

I would like to sincerely thank my advisor, Dr. Christopher Neale, for his direct and remote mentoring throughout the time of this research. This research would not come to an end without his expertise. I would like to specially thank Dr. Neale for hosting me at the Daugherty Water for Food Global Institute at the University of Nebraska in Lincoln, allowing me to complete my dissertation work.

Many thanks to my committee members, Dr. Jagath Kaluarachchi and Dr. David Stevens; and special thanks to Dr. Lawrence Hipps, Dr. John Shervais, Dr. Scott Jones, and Dr. Heng Ban for their mentoring and time to guide my research in their area of expertise.

Special thanks go to Dr. Henry Heasler and Dr. Cheryl Jaworowski, Yellowstone National Park Geologists, for their field support, technical advice on many aspects of this project and continuous belief in the value of the research.

Thanks are due to Dr. Paul Barr and the Department of Civil and Environmental Engineering for the continuous support at the later stages of my studies.

I am grateful to the staff of Daughterly Water for Food Global Institute at the University of Nebraska for generously hosting me during the last eight months of my PhD program.

I would like to thank many individuals who had technically contributed to this work through brain storming and discussions, Dr. Scott Jones, Ashish Masih, Tseganeh Zekiewos, Tian Jan, and Kshitij Parajuli.

My sincere gratitude to my family, especially my husband for his continuous support and encouragement, and my two sons, and for my family in Sudan, my father and my siblings, for their unconditional love and support. This research is dedicated to the memory of my mother, who was my role model in tolerance and resilience.

This research was partly funded by the National Park Rocky Mountain Cooperative Ecological Study Units Agreements (RM-CESU J1580050583, J1580050608, and J1580090425) and by the Department of Civil and Environmental Engineering at Utah State University, the Remote Sensing Services Laboratory, and the Utah Agricultural Experiment Station (UTA00793 and UTA01140). The LASSI LIDAR and imaging system was developed with funds from the Utah Science Technology and Research initiative (USTAR) at Utah State University.

Ruba A. M. Mohamed

CONTENTS

Page

LIST OF TABLES

LIST OF FIGURES

CHAPTER 1

INTRODUCTION

1.1. Background

Geothermal heat is generated from an underlying reservoir of high temperatures, steam, and hot water beneath the earth surface. The underlying heat and the existing ground water and surface water lead to the formation of different hydrothermal features including hot springs, geysers, mud pools, and fumaroles (Haselwimmer and Prakash, 2013). Frequent monitoring of the hydrothermal features and the surrounding heated ground in Yellowstone National Park (YNP) will help (1) update the existing information about the size and temperature of the features, (2) maintain the safety of the visitors and park service personnel, (3) plan new infrastructure and relocate existing ones, (4) foster research activities, and (4) study potential impact from nearby geothermal development including oil and gas industry (Heasler et al., 2009).

Different methods have been used to model the spatial and temporal changes of the geothermal system in YNP. In-depth studies include changes of the structural framework of the geothermal system including the size of the plume and the temporal distribution of the seismic activity (Shervais and Hanan, 2008). Some studies used surrogates of heat rate to study the temporal changes in the heat rate. For example, Fournier et al. (1976) were the first to use the chloride inventory method of Ellis and Wilson (1955). The method stated that thermal chloride is mainly generated from deep parent water of known heat content. It was applied through real-time measurement of

stream discharge and grab sampling of chloride to determine the chloride load as an indicative of the convective heat from the main rivers draining Yellowstone's caldera. The chloride load was found strongly correlated with the levels of groundwater that had dropped significantly during the past ten years due to inflation of the ground surface in some areas of the caldera (Friedman and Norton, 2007). Increased ground-water head generated by snowmelt releases the chloride stored in shallow groundwater systems. Thermal chloride has a steady flux that leaches from deep thermal aquifers that are not greatly affected by changes in the height of the water table. Other limitations related to the method include the installation and maintenance of the real-time instruments, and the frequent need to access the gauging stations (Heasler et al., 2009).

The use of remote sensing in YNP started as early as the 1960s with major limitations on technologies and methodologies at that time (McLerran and Morgan, 1900; White and Miller, 1969). With the latest developments of that technology, remote sensing has been frequently used to map the thermal anomalies in YNP. Examples of recent satellite remote sensing studies include Watson et al. (2008) and Vaughan et al. (2012) and of airborne remote sensing, Neale and Sivarajan (2011b); Jaworowski et al. (2013); and Neale et al. (2016). The goal of these studies was to estimate the infrared radiometric temperature of the surface through the thermal infrared radiometric images (TIR). Satellite remote sensing has the advantage of providing frequent coverage and relatively lower cost per unit area compared to airborne remote sensing (Franklin, 2001). However, satellite remote sensing provides relatively course pixel resolution and suffers from cloud

interference. Also the size of most of the hottest hydrothermal features in YNP are within a range of a few square meters which encouraged the use of airborne remote sensing methods to obtain high-resolution images of the features.

1.2. Problem Statement

In geothermal areas, three main heat sources contribute to the ground heat flux at and near the surface including the geothermal heat flux, the absorbed solar shortwave radiation (residual from the direct solar shortwave radiation and the reflected shortwave radiation by the ground surface), and the emitted atmospheric longwave radiation (emitted by clouds and greenhouse gases) absorbed by the surface. Latent heat flux and sensible heat flux are usually lost from the ground as ground temperatures are mostly greater than the surrounding atmosphere. Therefore the radiant temperature estimated through atmospherically corrected TIR images includes the three former heat fluxes. The main technical challenge in order to compare changes in the heat rate over time from the geothermal source is removing the radiant flux due to absorption of solar shortwave radiation and atmospheric longwave radiation. The incident solar radiation is a function of the atmospheric transmissivity and the geographic position of the study area. Whereas the atmospheric longwave radiation is a function of the atmospheric emissivity, which is influenced by the amount of atmospheric water vapor, carbon dioxide, oxygen, and by air temperature. Generally, TIR images are acquired during nighttime hours, under clear sky conditions, to minimize heat flux due to the latter two sources. However, quantifying the remaining heat flux from the two sources remained a challenge facing the recent remote sensing studies. Some methods were suggested to quantify the heat flux. However, most

of the suggested methods were approximate and based on general assumptions. For example, Vaughan et al. (2012) used ASTER and MODIS satellite data and subtracted the background solar radiant emittance from a nearby non-geothermal area with similar topographic and surface cover. Their method although conceptually simple, it can be uncertain due to the selection of the background area. Practically, it is not possible to select a background area that is perfectly suitable to remove the residual heat effect. Geothermal areas are characterized by unique mineral compositions and vegetation cover that are specific to these areas. Watson et al. (2008) used Landsat Enhanced Thematic Mapper to estimate the radiant geothermal heat flux in YNP. They used an empirical model to detect the heat flux due to solar radiation using a variable proportional to the absorbed solar radiation accounting for the exoatmospheric solar irradiance in bands 1-7, incidence angle of the sun, at-satellite spectral, and band width. However, their model did not account for atmospheric transmission of incoming radiation or diffuses sky irradiance of the surface.

1.3. Study Area

The focus of this study was in Norris Geyser Basin (NGB) which is known for the hottest and most dynamic hydrothermal features in YNP (White et al., 1988). The basin is located in the northwestern part of YNP centered at latitude 44.728546300 and longitude -110.7043754000, with an approximate area of 5.5 km^2. It was selected to conduct the thermal monitoring plan because the basin is a closed hydrological system. The Tantalus Creek, a tributary of the Gibbon River, drains the basin. The creek is monitored by USGS for water temperature, discharge, and gage height. Two towers were installed in bare

heated grounds southwest and northeast of an explosion crater pool in the gap area in NGB to monitor the radiation energy balance components of this particular area.

1.4. Objectives

This study was developed in 2005 as part of the CESU Task Agreement between Utah State University and the National Park Service. The main goal from the agreement was to explore the use of high resolution airborne remote sensing imagery to fulfill the need for accurate and continuous monitoring of the thermal activity in YNP (Neale and Sivarajan, 2011a). The study is considered the first in NGB to monitor the heat transport over multiple years using a consistent method. The agreement included acquisition of annual, and in some years, biannual TIR images, and multispectral and LiDar images of the hydrothermal areas in the park. The first three years of the monitoring program have resulted in improvements in image acquisition, processing and calibration methods that have led to the production of highly accurate and precise images (Neale et al., 2016).

In addition to the remote sensing campaign, the agreement included ground-based measurement of weather and soil parameters to help estimate the heat flux due to solar radiation and atmospheric longwave radiation. Accordingly, two towers were installed close to an explosion crater pool in the Gap area in Norris Geyser Basin (NGB), to provide real-time measurements of different weather and soil parameters. The measured parameters included air temperature, relative humidity, four-way radiations, wind speed and direction, besides soil parameters that included soil heat flux, soil temperature and water content.

In Chapter 2 of the dissertation an approach was used to estimate order-of-magnitude radiant geothermal heat flux for a bare ground covered with thermal siliceous sinter deposit, using the ground-based measurements and three TIR images acquired for NGB. The ground-based parameters used on that approach included surface radiation fluxes, ground heat flux, and ground skin temperature and the temperature measured at 0.05 m depth. The approach was based on a simple comparison of the average conductive ground heat flux measured on sunny summer days and overcast winter days. The conductive ground heat flux used for the comparison was measured during times with expected minimal solar heat effect (i.e. net radiation flux was lost from the ground and the temperature gradient of the top soil layer was from the subsurface to the ground surface). To account for the heat loss due to snow melt during the winter days, the Utah Energy Balance Snow Accumulation and Melt Model developed by Tarboton and Luce (1996) was used. The radiant flux due to solar radiation was estimated using the assumed proportionality between the conductive heat flux due to solar radiation and radiant flux due to solar radiation with the total measured conductive heat flux and total radiant flux. Since the conductive heat flux was measured on a bare ground soil covered siliceous sinter deposit, the approach can be spatially applied on areas cover with that type of deposit, which represent the majority of the soil in NGB. To validate the estimated residual heat the results were compared to values estimated in areas with non-geothermal background under similar conditions.

Chapter 3 of the dissertation addresses the contribution of four heat flux

mechanisms, including conduction, convection of sensible heat by liquid water and water vapor, and convection of latent heat by water vapor, on the top layer of the soil and at the ground surface. The chapter also estimated and compared the rate of heat transport from each of the mechanisms. The study was done to test the hypothesis that latent heat flux and sensible heat flux were of least significance to the overall heat flux and that heat conduction was dominant. The numerical model HYDRUS-1D, developed by Šimunek et al. (1998) was used to simulate the coupled movement of heat transport, and water and water vapor flow in the soil. HYDRUS-1D implements an inverse solution to estimate soil hydraulic and thermal parameters from measured transient flow and transport data including water content, pressure head, and temperature (Deb et al., 2011; Saio et al., 2006). Kool et al. (1985) applied the inverse approach by numerical solution of the Richards equation for a one-step outflow experiment and concluded that variation of the estimated parameters can be minimized if the experiment is designed to cover a wide water content range. In this study, days with variable water content were used for model calibration and validation to optimize the estimates of soil hydraulic parameters that were not measured on site.

Chapter 4 addresses the study of the spatial and temporal changes in radiant flux and changes in the extent of the geothermal region within NGB using the high resolution remote sensing imagery obtained in five consecutive years between 2009 and 2013. The chapter also addressed year-to-year comparison of the geothermal radiant flux after removing the heat flux due to solar radiation from the radiant flux images. The surface in

NGB is comprised of seven different classes, including bare soil, soil covered with siliceous sinter deposit, lakes and pools, river, forest (pine trees), grass, and mud pools. For bare soil and siliceous sinter soil, the heat flux from solar radiation is a function of elevation, slope, and aspect (Chen et al., 2013). In this study, the surface was classified into groups of aspects (north, northeast, east, southeast, south, southwest, west, and northwest) for six ranges of slopes from 0° to 61° using 10° increment. The heat flux due to solar radiation was estimated for each group assuming that ratios of beam solar irradiance received at each group and beam irradiance of a background area with flat aspect and 0° slope was similar to the ratio between the radiant temperatures of these groups and the radiant temperature of the background area. That background area was chosen outside of the identified geothermal polygon in NGB. The beam solar irradiance for NGB was estimated using the Solar Irradiance and Irradiation Model available in Grass GIS 7.2 software (Team, 2016). The model accounts for surface elevation, terrain aspect and slope, atmospheric turbidity, ground albedo, and clouds and haze effect (Hofierka and Suri, 2002; Šúri and Hofierka, 2004). The radiant flux due to solar radiation was removed from the other five classes by subtracting the radian heat flux of a background area out of the hydrothermal polygon. Subtracting the heat flux from a background non-geothermal area is commonly used in areas with geothermal heat source (Seielstad and Queen, 2009; Vaughan et al., 2012).

References

Chen, X., Su, Z., Ma, Y., Yang, K., Wang, B., 2013. Estimation of surface energy fluxes under complex terrain of Mt. Qomolangma over the Tibetan Plateau. Hydrology and earth system sciences, 17(4), 1607-1618.

Deb, S. K., Shukla, M. K., Sharma, P., Mexal, J. G., 2011. Coupled liquid water, water vapor, and heat transport simulations in an unsaturated zone of a sandy loam field. Soil Science, 176(8), 387-398.

Ellis, A. J., Wilson, S. H., 1955. The heat from the Wairakei-Taupo thermal region calculated from the chloride output. NZJ Sci. Technol. Sect. B, 36, 622-631.

Fournier, R. O., White, D. E., Truesdell, A. H., 1976. Convective heat flow in Yellowstone National Park.

Franklin, S. E., 2001. Remote sensing for sustainable forest management: CRC Press.

Friedman, I., Norton, D. R., 2007. Is Yellowstone Losing Its Steam?—Chloride Flux out of Yellowstone National Park.

Haselwimmer, C., Prakash, A., 2013. Thermal infrared remote sensing of geothermal systems Thermal Infrared Remote Sensing (pp. 453-473): Springer.

Heasler, H. P., Jaworowski, C., Foley, D., 2009. Geothermal systems and monitoring hydrothermal features. Geological Monitoring, 105-140.

Hofierka, J., Suri, M., 2002. The solar radiation model for Open source GIS: implementation and applications.

Jaworowski, C., Heasler, H., Neale, C., Saravanan, S., Masih, A., 2013. Temporal and seasonal variations of the Hot Spring Basin hydrothermal system, Yellowstone National Park, USA. Remote Sensing, 5(12), 6587-6610.

Kool, J. B., Parker, J. C., Van Genuchten, M. T., 1985. Determining soil hydraulic properties from one-step outflow experiments by parameter estimation: I. Theory and numerical studies. Soil Science Society of America Journal, 49(6), 1348-1354.

McLerran, J. H., Morgan, J. O., 1900. Thermal Mapping of Yellowstone National Park.

Neale, C. M. U., Jaworowski, C., Heasler, H., Sivarajan, S., Masih, A., 2016. Hydrothermal monitoring in Yellowstone National Park using airborne thermal infrared remote sensing. Remote Sensing of Environment, 184, 628-644.

Neale, C. M. U., Sivarajan, S., 2011a. Integrated Study of Systematic Monitoring and Mapping Thermal Springs and Features in Yellowstone National Park. Report to Yellowstone Ecolocical Unit

Saito, H., Šimůnek, J., Mohanty, B. P., 2006. Numerical analysis of coupled water, vapor,

and heat transport in the vadose zone. Vadose Zone Journal, 5(2), 784-800.

Seielstad, C., Queen, L., 2009. Thermal Remote Monitoring of the Norris Geyser Basin, Yellowstone National Park. Final Report for the National Park Service Cooperative Ecosystem Studies Unit, Agreement(H1200040001), 38.

Shervais, J. W., Hanan, B. B., 2008. Lithospheric topography, tilted plumes, and the track of the Snake River–Yellowstone hot spot. Tectonics, 27(5).

Šimunek, J., van Genuchten, M. T., Senja, M., 1998. The HYDRUS-1D software package, code for simulating the one-dimensional movement of water, heat and multiple solutes in variably saturated porous media, version 2.01: IGWMC-TPS-53, Int. Ground Water Modeling Cent., Golden, Colo. School of Mines, Golden, USA.

Šúri, M., Hofierka, J., 2004. A new GIS- based solar radiation model and its application to photovoltaic assessments. Transactions in GIS, 8(2), 175-190.

Tarboton, D. G., Luce, C. H., 1996. Utah energy balance snow accumulation and melt model (UEB): Citeseer.

Team, G. D., 2016. Geographic Resources Analysis Support System (GRASS), GNU General Public License. Retrieved from http://grass.osgeo.org

Vaughan, R. G., Keszthelyi, L. P., Lowenstern, J. B., Jaworowski, C., Heasler, H., 2012. Use of ASTER and MODIS thermal infrared data to quantify heat flow and hydrothermal change at Yellowstone National Park. Journal of Volcanology and Geothermal Research, 233, 72-89.

Watson, F. G. R., Lockwood, R. E., Newman, W. B., Anderson, T. N., Garrott, R. A., 2008. Development and comparison of Landsat radiometric and snowpack model inversion techniques for estimating geothermal heat flux. Remote Sensing of Environment, 112(2), 471-481.

White, D. E., Hutchinson, R. A., Keith, T. E. C., 1988. Geology and remarkable thermal activity of Norris Geyser Basin, Yellowstone National Park, Wyoming. US Geol. Surv., Prof. Pap.;(United States), 75(1456).

White, D. E., Miller, L. D., 1969. CALIBRATION OF GEOTHERMAL INFRARED ANOMALIES OF INTENSITY IN TERMS OF HEAT FLOW YELLOWSTONE NATIONAL PARK.

CHAPTER 2

USING HIGH RESOLUTION THERMAL INFRARED IMAGES TO ESTIMATE RADIANT GEOTHERMAL FLUX FROM MEASUREMENT OF CONDUCTIVE HEAT FLUX AT NORRIS GEYSER BASIN, YELLOWSTONE NATIONAL PARK

Abstract

In geothermal areas, the ground heat flux at and near the surface is mainly a combination of near-surface geothermal heat flux and the heat flux from absorbed solar shortwave radiation and atmospheric longwave radiation. In these areas, latent heat flux and sensible heat flux are mostly lost to the atmosphere as the ground temperature was mostly much higher than the surrounding atmosphere. Challenges still remain in removing the radiant flux due to absorbed solar radiation from thermal infrared remote sensing imagery that are mostly acquired during nights of mostly sunny days to avoid the effect of clouds. Removing the absorbed solar radiant effect from the images will allow for a more precise spatial estimate of radiant output due to the geothermal source allowing for temporal monitoring of the geothermal system. In this study a simple method based on a comparison of continuous measurement of conductive soil heat flux, surface four-way radiations, and ground temperature at and near the ground surface is propose to estimate the conductive heat flux due to solar radiation in a daily and seasonal basis. The heat flux due to solar radiation was estimated by comparing the average conductive heat flux at the surface when net radiation values (R_n) were negative and the ground temperature gradient values (ΔT) were positive (heat flows from the subsurface towards the surface), among selected overcast winter days and sunny summer days after

accounting for the heat lost by snow melt during the winter days. To results were validated through comparison with literature values estimated in non-geothermal grounds with similar surface albedo and atmospheric conditions, where the ground heat flux is mainly from solar and atmospheric longwave radiations. The estimated conductive heat flux from solar radiation was used to estimate the radiant geothermal flux assuming that the ratio between the estimated conductive heat flux and radiant flux from absorbed solar and atmospheric radiations equals the ration between the estimated total conductive heat flux and radiant flux estimated from high resolution thermal infrared imagery acquired for Norris Geyser Basin. This assumption assumes that the ratio between the conductive ground heat flux at the surface and the radiant flux at the same location is constant.

2.1. Introduction

Yellowstone National Park (YNP) is characterized with increased heat rate from the underline active magmatic system (Allaby, 2013). The heat is transferred to the ground surface through different mechanisms including conduction, convection, and radiation. From the earth interior, the heat transfers by conduction through molten rocks and by convection through hot water and steam. From the ground surface-atmosphere interface, heat transfers through convection as sensible flux and latent heat flux to the atmosphere. Heat also radiates from the ground surface to the cool atmosphere in the thermal region of the electromagnetic spectrum (Lombardo and Buongiorno, 2013).

Studying the heat transport rate from hydrothermal areas and surrounding heated ground in YNP has been continuously conducted to determine possible changes due to natural or anthropogenic sources (Sorey, 2000). Different methods have been used to

directly measure the heat transport rate using surface and near-surface temperature measurements (Stein, 1995). These methods measure surface temperature and the temperature gradient near the surface to estimate near-surface geothermal heat flux. Recently; Hurwitz et al. (2012a) used manual data loggers to measure the temperature gradient in more than 600 locations at a vapor dominated area with low permeable bedrock in YNP. Fournier et al. (1976) and Friedman and Norton (2007) used an indirect method to estimate the geothermal heat flux rate from thermal chloride load on rivers and streams draining YNP. In geothermal areas, thermal chloride is mainly generated from deep parent water of known heat content (Lowenstern and Hurwitz, 2008). The method was applied through real-time measurement of stream discharge and grab-sampling of chloride to estimate the chloride load and the subsequence convective heat power. The previous methods, although they can be mostly accurate, require frequent physical access to potential remote hydrothermal grounds which makes it almost impossible to cover large areas.

Remote sensing imagery are increasingly used in YNP to provide large spatial estimate of radiant flux with less need to access the remote hydrothermal areas in the park. Watson et al. (2008); Vaughan et al. (2012); Neale et al. (2011); and Jaworowski et al. (2013) reported recent satellite and airborne remote sensing studies in YNP. One of the main technical challenges to estimate the radiant flux from the geothermal source through thermal infrared images (TIR) is the presence of radiant flux from absorbed solar shortwave radiation and atmospheric longwave radiation at the surface. The term ‘residual heat flux’ is used in this study to refer to the conductive heat flux in the ground surface from absorbed solar shortwave radiation and atmospheric longwave radiation.

Generally, airborne TIR images are acquired at late night hours on days with mostly clear skies, to maintain minimal effect from the residual heat flux. However, the quantity of the remaining residual heat flux remains unknown. Researchers used different methods to estimate the radiant residual flux using remote sensing platforms. For example, Vaughan et al. (2012) subtracted the radiant flux of a nearby non-geothermal area using ASTER and MODIS satellite TIR images. Their method although conceptually simple, may be uncertain in relation to the selection of a non-geothermal background area. Practically, it is not possible to select background area that is perfectly suitable to remove the residual heat flux. Geothermal areas are characterized by unique mineral deposits and vegetation. Watson et al. (2008) used Landsat Enhanced Thematic Mapper to estimate the radiant geothermal heat flux. They used an empirical model to estimate the residual solar flux using a variable proportional to the absorbed solar radiation. However, their model ignored the atmospheric transmission of incoming radiation or diffused sky irradiance of the surface. Seielstad and Queen (2009) conducted an airborne remote sensing study in NGB in 2005 and 2006. They estimated a background radiant flux from solar radiation as 200 $W \cdot m^{-2}$ and a range of radiant geothermal heat flux between 150 $W \cdot m^{-2}$ and 300 $W \cdot m^{-2}$ for the entire basin. The authors classified the basin into five land-cover types (forest, water, sinter soil, and road) and then estimated weighted mean flux within each land-cover class, outside a defined hydrothermal polygon in NGB. Our observation of the radiant temperature outside the previously defined geothermal polygon indicated presence of areas with high temperatures that matches the temperature of some of the areas within the geothermal polygon and cooler areas adjacent to the Gibbon River plain . Using the weighted mean flux to estimate the heat flux out of the background areas raised

a question about the bias associated with the presence of the hot and cool areas within the defined background areas.

In this study, the conductive heat flux due to solar radiation was estimated using continuous measurement of soil heat flux, soil temperature, ground skin temperature, and weather data, measured at a bare ground area, covered with hydrothermal siliceous sinter deposits, near the explosion crater pool in Norris Geyser Basin (NGB). The continuous measurement was part of airborne remote sensing cooperative agreement between Utah State University and the National Park Service (Neale and Sivarajan, 2011a). The agreement included acquisition of high resolution (approximately 1 m * 1m) airborne TIR images of NGB (Neale et al., 2011). The ground-based measurement was established in the summer of 2009 to 1) obtain information about weather and atmospheric conditions during the time of TIR image acquisition, 2) estimate the conductive heat flux due to solar radiation from measurement of four-way radiations, weather parameters, soil heat flux, and soil temperature at multiple depths. The estimates of conductive heat flux due to solar radiation was validated by comparing the results with previous studies that measured or estimated soil heat flux in non-geothermal grounds with similar soil albedo and weather conditions. This study proposes a method to estimate the radiant flux due to solar radiation by assuming that the ratio between the estimated conductive heat flux due to solar radiation and the estimated total ground heat flux at the surface equals the ratio between the radiant flux due to solar radiation and total radiant flux estimated from the TIR images.

2.2. Study Area

Norris Geyser Basin is located in the northwestern part of YNP covering an area of about 5.5 km^2 (Fig. 2.1). The basin includes zones of faults and volcanic vents and encompasses one of the most dynamic hydrothermal areas in the park (White et al., 1988). The study area is located close to the explosion crater pool in the Gap area. Two ground-based measurement towers were mounted northeast and southwest of the pool (Fig. 2.2). The collected ground-based data included surface radiation fluxes, meteorological and soil data, which are described in details in the next paragraph (Neale, 2014).

2.3. Methods

2.3.1. Data

The two ground-based towers were installed within approximately 20 m northeast (44.729567° N/110.715756° W) and southwest (44.728975° N/110.716011° W) of the crater pool. The data used for this study were collected between August 15, 2009 and July 2, 2012. Data acquisition and storage were managed by two Campbell Scientific data loggers (CR1000 and CR3000). The data were collected at five-minute intervals (Figs. A-1 to A-8 in appendix A) using the sensors and probes described in Table (2.1). The two sites are herein referred to as CR3000 site and CR1000 site according to the associated data logger.

Variables measured at the CR3000 site included air temperature (T_a), relative humidity (*RH*), precipitation, and wind speed (*WS*) and direction. These measurements

were collected over bare ground surface that had a daily average summer surface temperature of 25 ºC. The four components of radiation (i.e. downwelling solar radiation (R_S), upwelling solar radiation (R_s'), downwelling longwave radiation (R_l), and upwelling longwave radiation (R_l'), were also measured at about 2 m above the ground surface. Net radiation (R_n) was determined from the four components of radiation. Soil parameters including ground heat flux at 0.1 m depth (G_Z), and soil temperature (T_Z) and volumetric water content (θ_Z) at 0.05 m depth, were also measured. The data collected at the CR1000 site were from a relatively cooler area, compared to the CR3000 site. With a daily average surface temperature as 20 ºC in summer months. Similar to the CR3000 site, T_a, RH, and R_n were also measured at approximately 2 m above the ground surface, G_Z was measured at 0.1 m depth, and T_Z and θ_Z were measured at 0.05 m depth. The data collected at CR1000 site were used in this study for comparison purpose, to observe inconsistencies in the trend of the data collected at the CR3000 site (Fig. A-5 to Fig. A-8 in Appendix A). The instrument and sensors used for data collection, accuracy of the measurement, and the manufacturers are summarized in Table (2.1).

The three hourly precipitation data used to estimate the heat loss from snow meltwater was obtained from SNOTEL station located at west Yellowstone operated by the National Water and Climate Center from the US Department of Agriculture (USDA) (U.S. Department of Agriculture and Service, 2016)

2.3.2. Estimation of Ground Skin Temperature (T_s)

In this study, the difference (ΔT) between ground skin temperature (T_S) and the subsurface temperature measured at 0.05 m depth (T_Z) was used to determine the

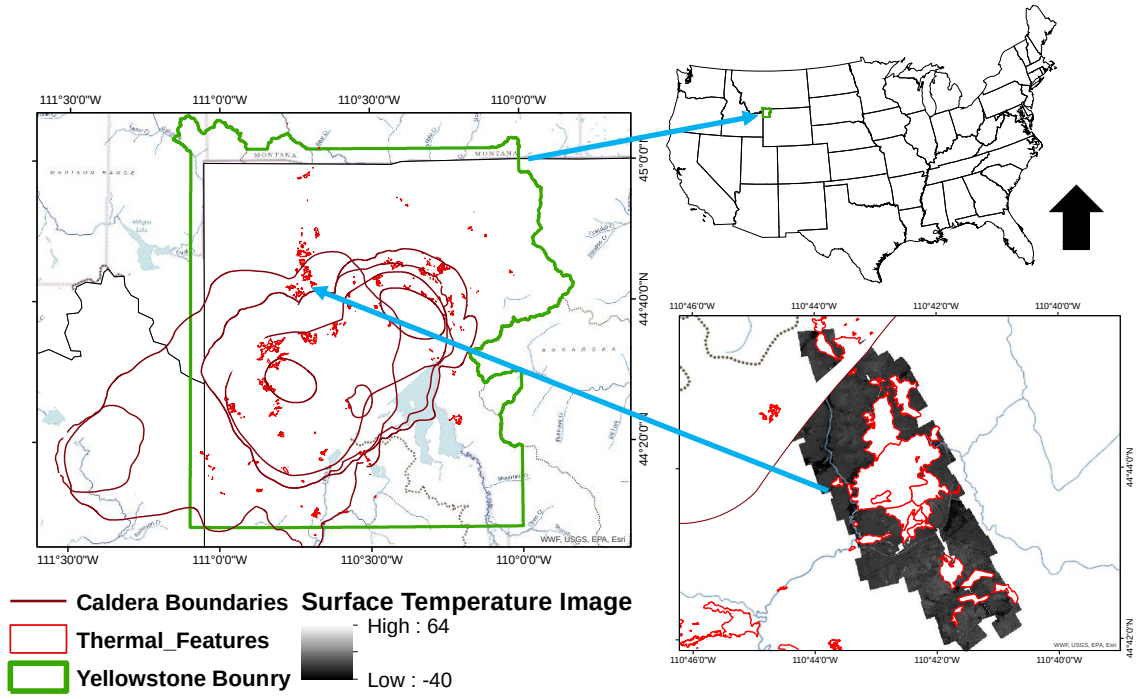

Fig. 2.1. Norris Geyser Basin (NGB) in northwestern Yellowstone National Park and the TIR image by USU showing the radiant temperature of NGB on April 2013.

direction of the heat flow in the soil. Understanding the direction of heat flow can help determine the time with possible effect from absorbed solar radiation, as heat flows in the direction of decreased temperature. The ground skin temperature was estimated using the measured upwelling longwave radiation, ($R_l^{'}$) using Stefan-Boltzmann equation

$$R_l^{'} = \varepsilon\sigma T_s^4 \quad (1)$$

where ε is the surface emissivity for bare soil, σ is Stefan-Boltzmann constant ($5.67*10^{-8}$ $W \cdot m^{-2} \cdot K^{-4}$), and T_s (K) is the ground skin temperature (K). Surface emissivity, ε, was obtained from the Advanced Spaceborne Thermal Emission and Reflection Radiometer (ASTER) Global Emissivity Dataset (GED) Product by the National Aeronautics and Space Administration (NASA) (Abrams, 2000). The dataset is available on $1^o \times 1^o$ tiles at 100-meter resolution. ASTER GED was created by processing millions of ASTER data

during cloud free times between 2000 and 2008. The average emissivity of the surface was then calculated at the five ASTER TIR wavelengths (Bands 10, 11, 12, 13, and 14). The average emissivity value at the CR3000 tower for all wavelengths was 0.89 with 0.001 standard deviation. An uncertainty in emissivity value is expected due to the coarse spatial resolution of ASTER GED image. A sensitivity analysis for the typical range of siliceous sinter soils (0.86-0.89) revealed that the maximum difference in T_S was about 2.67 °C for $\varepsilon = 0.86$ and $\varepsilon = 0.89$.

2.3.3. Correction of Measured Ground Heat Flux (G_z)

The ground heat flux, G_z, was measured at 0.1 m depth, using a model HFT3 REBS soil heat flux plate (Fig. 2.3). The heat flux plate contains a thermopile that measures the temperature at the two sides of the plate (Scientific, 2003). With a known thermal conductivity of the plate (1.22 $W \cdot m^{-1} \cdot K^{-1}$), the heat flux through the plate is calculated by multiplying the temperature gradient by the plate thermal conductivity. The heat flux plate method is widely used due to its simplicity; however, heat flow distortion may be introduced due to unmatched thermal conductivities of the plate and the surrounding soil (Mayocchi and Bristow, 1995; and Sauer et al., 2003). Soil thermal conductivity varies with physical soil properties (i.e. particle size, soil minerals, density, and water content); however, the thermal conductivity of the plate is fixed for a known design ranges. The method developed by Philip (1961) was used to correct the heat flux values for heat flow distortion given the plate dimensions and thermal conductivity. A correction factor (f) for the measured heat flux and the ground heat flux in the surrounding soil media is given by

$$f = \frac{k_p / k_s}{\left(1 + \left(k_p / k_s - 1\right) H\right)} \quad (2)$$

$$H = 1 - 1.92 \frac{t}{D} \quad (3)$$

where k_p ($W \cdot m^{-1} \cdot K^{-1}$) is the thermal conductivity of the plate, k_s ($W \cdot m^{-1} \cdot K^{-1}$) is the thermal conductivity of the surrounding soil, H is a factor depends on the shape and geometry of the heat flux plate, t is the plate thickness (3.91 mm), and D is the plate diameter (38.2 mm). In this study the correction factor, f, used to correct soil heat flux measurements varied between 0.91 and 0.79. The variability of f was controlled by the variability of the soil water content between the residual water content (0.15 $gm \cdot gm^{-1}$) and the saturation water content (0.38 $gm \cdot gm^{-1}$).

2.3.4. Estimation of Ground Heat Flux at the Surface (G_s)

The ground heat flux estimated at the surface (G_s) is often underestimated due to ignoring the heat flux stored in the soil above the heat flux sensor (Mayocchi and Bristow, 1995). Potential effect of latent heat flux on the soil heat flux measurements is not expected to be significant in this study since the plate was buried in a relatively deep depth (Gentine et al., 2012). To estimate the conductive heat flux at the soil surface, heat storage in the soil layer above the plate, ΔS, and ground surface heat flux, G_s, were estimated using the calorimetric heat storage method (Fuchs and Tanner, 1968; Ochsner et al., 2007).

$$G_z(t) = G_s(t) + \Delta S(t) \quad (4)$$

$$\Delta S(t) = C_s(t) \cdot z \cdot \Delta T_z / \Delta t \quad (5)$$

$$C_s(t) = \rho_b C_d + \theta(t) \cdot \rho_w(t) \cdot C_w(t) \quad (6)$$

$$C_W(t) = 4.2174 - 3.270283 * 10^{-3} \cdot T_S(t) + 1.412855 * 10^{-4} \cdot T_S^2(t) - 2.654387 * 10^{-6} \cdot T_S^3(t) + 2.93236 * 10^{-8} \cdot T_S^4(t) \quad (7)$$

$$\rho_W(t) = 999.842594 + 6.793952 * 10^{-2} \cdot T_S(t) - 9.095290 * 10^{-3} \cdot T_S^2(t) + 1.001685 * 10^{-4} \cdot T_S^3(t) - 1.120083 * 10^{-6} \cdot T_S^4(t) + 6.536335 * 10^{-9} T_S^5(t) \quad (8)$$

$$\varepsilon = 0.89 \pm 0.001 \quad (9)$$

where z is the depth above the plate (0.1 m); ΔT is the change in temperature at depth z over time, C_s ($J \cdot m^{-3} \cdot {}^oC^{-1}$) is the heat capacity of moist soil, ρ_b ($g \cdot cm^{-3}$) is the bulk density of dry soil; C_d ($J \cdot g^{-1} \cdot {}^oC^{-1}$) is the specific heat of dry soil, C_w ($J \cdot g^{-1} \cdot {}^oC^{-1}$) is the specific heat of water calculated using a numerical equation (eq. 7) described in Millero, Perron, and Desnoyers (1973), and ρ_w ($g \cdot cm^{-3}$) is the density of water calculated using eq. (8) as in Gill (1982). The parameter C_s is generally a function of the water content of the soil; however, ρ_b and C_d are assumed specific to the type of soil. The average ρ_b for soil samples collected on site at depth ranged between 5 and 13 cm was 1.31 $g \cdot cm^{-3}$. The average C_S measured on site using KD2 probe at the same depth range was $2.43 * 10^6$ $J \cdot m^{-3} \cdot {}^oC^{-1}$ and the average θ was 0.15 $g \cdot g^{-1}$. Using eq. (6), the average C_d was calculated as 1.24 $J \cdot g^{-1} \cdot {}^oC^{-1}$ by substituting the values of C_S, ρ_b, θ and C_w. Given that C_d does not vary greatly for the soil type, $C_s(t)$ was estimated as a function of $\theta(t)$, $\rho_w(t)$, and $C_w(t)$ for the period of measurement.

2.3.5. Estimation of Advective Heat Flux from Snow Melt (Q_m)

The advective heat removed by meltwater of snow (Q_m) was numerically estimated using the Utah Energy Balance Snow Accumulation and Melt Model (UEB)

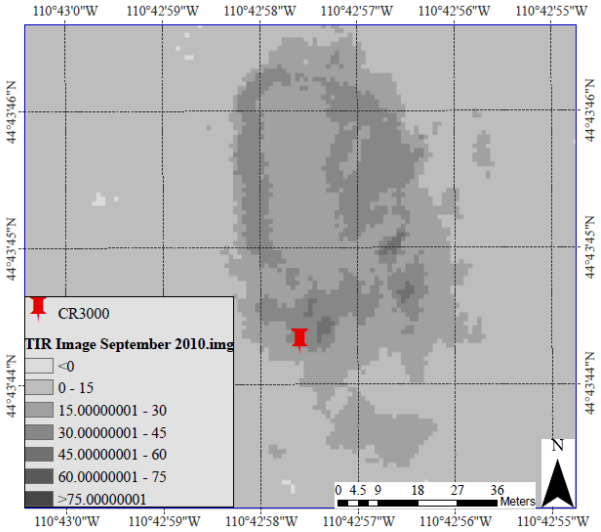

a. TIR image acquired by USU for NGB in September 2010 showing the radiant temperature and location of the CR3000 tower

c. CR1000 site at the northeast side of the explosion crater pool in NGB Photo date May 2009

b. Google map for the explosion crater pool and the location of the two towers CR1000 and CR3000 (1 inch =30.48 m)

d. CR3000 at the southwest side of the explosion crater pool in NGB Photo date May 2009

Fig. 2.2. The explosion crater pool in Norris Geyser Basin and the energy balance experiment towers CR3000 and CR1000.

Table 2.1.

Summary of parameters and instruments used for data collection.

Variable	Sensor Model	Accuracy	Manufacturer/Warranty
Ground Heat Flux, ,G_z ($W \cdot m^{-2}$)	HFT3 Soil Heat Flux Plate	Better than 5% of reading	REBS Inc., Seattle, WA
Soil Water Content, θ_z (wfv)	Steven Hydra Probe II	± 0.03 wfv ($m^3 \cdot m^{-3}$)	Stevens Water Monitoring System Inc. Portland, OR
Ground Temperature, T_z (°C)	Steven Hydra Probe II	± 0.6 Degrees Celsius (From -10° C to 36° C)	Stevens Water Monitoring System Inc. Portland, OR
Air Temperature, T_a (ºC)	HMP45C Temperature and Relative Humidity Sensor	0.8º C @ -40º C 0.6º C @ 60º C	Vaisala Company, Finland
Relative Humidity, *RH* (%)	HMP45C Temperature and Relative Humidity Sensor	± 2% RH (0 to 90% RH) ± 3% RH (90 to 100% RH)	Vaisala Company, Finland
Short Wave Radiation (R_s and R_s'), long wave radiation (R_l and R_l') ($W \cdot m^{-2}$)	NR01 Four-Component Net Radiation Sensor	± 10% for 12 hours totals, day and night	Hukseflux Thermal Sensors B.V., Delft, Netherlands
Net Radiation, R_n ($W \cdot m^{-2}$)	NR-Lite Net Radiometer	0.001 ºC for the thermopile which is proportional to R_n	Kipp & Zonen, Bohemia, NY
Wind Speed ($m \cdot s^{-1}$)	RM Young Wind Sentry Set	± 0.5 $m \cdot s^{-1}$	R. M. Young Company, Traverse City, MI
Wind Direction	RM Young Wind Sentry Set	± 5º	R. M. Young Company. Traverse City, MI
Rain (mm)	TE525 Tipping Bucket Rain Gauge	Up to 1 $in \cdot hr^{-1}$: ± 1% 1 to 2 $in \cdot hr^{-1}$: +0, -3% 2 to 3 $in \cdot hr^{-1}$: +0, -5%	Texas Electronics Inc. Huston, TX
Thermal conductivity ($W \cdot m^{-1} \cdot K^{-1}$), diffusivity ($mm^2 \cdot s^{-1}$), and heat capacity ($MJ \cdot m^{-3} \cdot K^{-1}$)	KD2 Pro Thermal Properties Analyzer	±5 to ±10% Thermal Conductivity/Resistivity ±10% Specific Heat ±10% Thermal Diffusivity	Decagon Devices Inc. Pullman, WA

developed by Tarboton and Luce (1996). The model assumes that the snowpack is characterized by water equivalence W (m), energy content U (kJ·m^{-2}), and snow age at the surface. The model numerically solves the energy balance equation (eq. 9) and mass balance equation (eq. 10) using inputs of air temperature, wind speed, relative humidity, precipitation, incoming solar radiation and longwave radiation, and ground heat flux, which were all measured on site.

$$\frac{dU}{dt} = Q_{sn} + Q_{li} + Q_P + Q_g + Q_h + Q_e - Q_m \tag{9}$$

$$\frac{dW}{dt} = P_r + P_s - M_r - E \tag{10}$$

The energy balance terms are in units of energy per horizontal area (i.e. kJ·m^{-2}·hr^{-1}); where, Q_{sn} is net shortwave radiation; Q_{li} net incoming longwave radiation; Q_p is advected heat from precipitation; Q_g is ground heat flux; Q_h is sensible heat flux; Q_e is latent heat flux due to sublimation/condensation; and Q_m is advected heat removed by meltwater. In the mass balance equation all terms are in m·hr^{-1} of water equivalence; where, P_r is rainfall rate; P_s is snowfall rate; M_r is meltwater outflow from snowpack; and E is sublimation from the snowpack. Many of these fluxes depend functionally on the state and input driving variables. In this study the model was applied from the beginning of the snow season on October 1st for each year from 2009 to 2012. The initial condition of snow age, energy content, and snow water equivalent were assumed to be zero. The model estimated Q_m as

$$Q_m = \rho_w h_f M_I \tag{11}$$

where ρ_w is water density (1000 kg·m^{-3}) and h_f is heat of fusion (333.5 kJ.kg^{-1}).

Sublimation is defined as vapor transport away from the surface and is described as

$$M_e = K_e \rho_a (q_s - q) \tag{12}$$

$$K_e = \frac{k^2 V}{\left[\ln h / z_0\right]} \tag{13}$$

where q_s is the surface specific humidity, K_e the vapor conductance ($m \cdot hr^{-1}$), ρ_a is air density ($kg \cdot m^{-3}$), k is van Karman's constant (0.4), V is wind speed ($m \cdot hr^{-1}$) at height h (m), and z_0 is height at which the velocity is zero (assumed 0.1 h for bare ground). The water equivalence depth of sublimation is described as

$$E = \frac{M_e}{\rho_w} \tag{14}$$

2.3.6. Estimation of Average Diurnal and Seasonal Heat Flux from Solar Radiation

To estimate the conductive heat flux due to solar radiation, the time with potential minimum heat flux due to solar radiation was determined using the direction of net radiation (R_n) and the temperature gradient in the soil. The temperature difference (ΔT) between the temperature measured at 0.05 m depth (T_z) and ground skin temperature (T_s), was used to determine the direction of the heat flow in the soil (Fig. 2.3). Generally, when ΔT is negative ($T_s > T_z$), heat flowing downward from the ground surface towards the cooler subsurface indicates heat gain from solar radiation and/or atmospheric longwave radiation. This scenario generally peaks during the day on clear and sunny days. When ΔT is positive ($T_s < T_z$), heat flowing upward from the subsurface towards the cooler atmosphere indicates heat loss from the soil which generally occurs under clear skies

shortly after sunset due to the radiation cooling effect.

The sign of net radiation, R_n, determines the direction of the radiative energy at the ground surface with positive values indicate that the incoming radiative energy exceeds the reflected and emission losses at the surface and negative values indicate that the energy loss exceeds the gain $\left(R_s + R_l < R_s^{'} + R_l^{'}\right)$. At the time when R_n is negative and ΔT is positive, the heat from the subsurface is a combination of the heat flux due to solar radiation and atmospheric radiations stored in the ground and the near-surface geothermal heat.

A diurnal cycle of R_n and ΔT were compared among a set of overcast winter days and mostly clear and sunny days. Overcast winter days with notably low measured incoming shortwave radiation and mostly negative R_n were observed during winter months of December 2009 and January 2011. On these days, air temperature was below freezing and R_n was negative during the entire day indicating that the heat flux due to solar radiation was minimal. However, during these days the ground temperature was predominantly greater that air temperature. For that latent and sensible heat fluxes were lost from the ground to balance the energy input from the geothermal source. The average ground heat flux relative to $-R_n$ and $+\Delta T$ during the previous days was compared with that of mostly sunny summer days, where the heat flux from solar radiation was expected to be high. The difference between the averages represent the lower bound of the conductive heat flux in the soil due to solar radiation effect. The method does not separate the effect of solar radiation from the atmospheric radiation. The night-time remote sensing TIR imagery are usually acquired on mostly clear and sunny days to

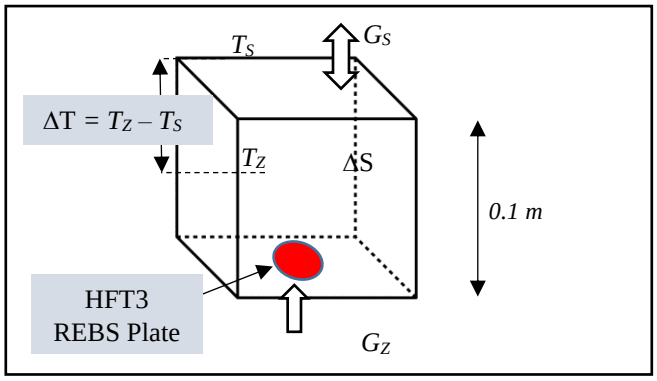

Fig. 2.3. Simulation shows the HUKSEFLUX plate at 0.1 m measuring G_z, G_s estimated at the surface, T_s estimated at the surface, and T_z measured at 0.05 m.

minimize the radiative effect due to clouds. This method represent a simplified method to estimate the average heat flux due to solar radiation. However, the heat from solar radiation varies greatly with the intensity and duration of solar radiation and with the cloud condition and time of the day.

2.4. Results

2.4.1. Observed Variability

The 5-minute measurements collected at the CR3000 site and the CR1000 site between August 15, 2009 and July 2, 2012 are presented in Figs. A-1 to A-4 and A-5 to A-8 in appendix A, respectively. The observed ground heat flux measured at 0.1 m depth, G_z, was mostly negative in the two sites indicating that the geothermal heat was dominant over the heat stored from solar and atmospheric longwave radiation. The largest G_z values occurred mostly during the night (low negative values). During the day, G_z changed gradually and became less negative as R_s increased. On sunny days with clear skies, G_z values were either low positive or large negative due to the increase in solar

heating. For example, 22 September 2009 was mostly sunny with maximum G_z value as -77.6 $W \cdot m^{-2}$ around noon and minimum value during the night as -223.2 $W \cdot m^{-2}$ around 11 pm. As the HTF3 heat flux plate thermopile measures the differential temperature across the ceramics-plastic body of the plate and generates a voltage proportional to the heat flux, G_z negative reading suggested that the differential temperature was lower during the day when solar radiation was present, which explains the low positive or high negative G_z values close to noontime on sunny days. Positive G_z values indicate that the temperature above the ceramics-plastic composite body was greater than the temperature below the body. The condition which occurred few times during the course of the study, on mostly clear sunny days.

The heat loss from snow meltwater during snow season explains some of the seasonal variability in G_z between summer and winter months. Fig. (2.4) shows the results from the UEB model including the cumulative precipitation (m), cumulative total outflow (m), cumulative snow sublimation (m), and cumulative melt energy ($W \cdot m^{-2}$). The total outflow represented more than 60% of the snow loss compared to less than 40% for sublimation.

Anomalous spikes in G_z (up to -400 $W \cdot m^{-2}$) were observed at the CR3000 site after precipitation, mainly during summer months where the form of precipitation was rain (Figs. A-1 to A-4 in Appendix A). This phenomena was clearly observed in 2009 between September 30th and October 31st when more than 50 mm of rain was recorded (Fig. A-1 in Appendix A). Similar increase in G_z after precipitation was also observed at the CR1000 site; however, the increase was less compared to that at CR3000 site. Also,

an anomalous increase in G_z occurred at the CR3000 site between January 11 and February 1, 2010, and September 6 and 20, 2010. During these days were also anomalous increase in the ground temperature, T_z, and the upwelling longwave radiation, R_l, were observed. This parallel increase in G_z, T_z, and R_l at CR3000 site, was neither observed at CR1000 site nor in the temperature of the nearby explosion crater pool.

2.4.2. Variability during Selected Summer and Winter Days

In this study, selected mostly sunny summer days and overcast winter days were used to demonstrate the diurnal variation of the heat flux due to solar radiation. The diurnal variability of some of the parameters measured at the CR3000 site for three consecutive sunny days of September 22-24, 2009, mostly cloudy winter days of January 10-12, 2010, and overcast winter days of December 29-31, 2009, and January 4-6, 2011, is observed in Figs. 2.5 and 2.6. The days of September 22-24, 2009 were mostly sunny (maximum $R_s \approx 720$ W·m^{-2}) (Fig. 2.5.a). On these days, net radiation (R_n) was positive during the day and negative shortly before sunrise and after sunset. Ground skin temperature (T_s) gradually increased at sunrise and was greater than the temperature measured at 0.5 m depth (T_z) at about an hour after sunrise. At about an hour after sunset T_s decreased and became lower than T_z resulting in negative temperature gradient ($-\Delta T$) until sunrise of the following day. Maximum T_s and T_z values during these days ranged between 34 and 37 °C and between 28 and 32 °C, respectively, and minimum values ranged between 12 and 16 °C and between 17 and 19 °C, respectively. Maximum and minimum T_a values ranged between 19 and 24 °C and between -3 and 10 °C, respectively.

Sunshine hours on January 10-12, 2010 was about nine hours compared to 12 hours on September 22-24, 2009 (Fig. 2.5.b). Fluctuations in R_s and R_n during January 10-12, 2010, were partly due to presence of snow clouds. About 0.2 inches of snow precipitated on each of the three days. Maximum heat loss due to snow meltwater was estimated at 48.7 $W \cdot m^{-2}$. Maximum and minimum T_s values were about 15 °C cooler during January 10-12, 2010 compared to September 22-24, 2009, and T_a was below freezing. Similar to September 22-24, 2009, T_a and T_s continued to gradually decrease after sunset until the following sunrise.

Weather conditions were similar during 29-31 December 2009 and 04-06 January 2011, generally cloudy with low R_s values and freezing air temperatures. About 0.2 inches of snow precipitated on 31 December 2009, and about a similar amount precipitated on each of the days of 04-06 January 2011. The radiant energy loss was mostly greater than the gain as indicated by the negative sign of R_n. Due to the cloudy condition during December 2009 and January 2011 days, the maximum R_s values at the ground surface were less than 200 $W \cdot m^{-2}$. On 30 and 31 December, and 04 and 05 January, R_n was negative throughout the day; and maximum R_n was noticeably low in December 29th and January 06th (Fig. 2.5.d).

2.4.3. Snowmelt and Advective Heat Loss

Snow water equivalent was zero during December 29 and 30, 2009 (Fig. 2.7). Maximum heat loss of 31.4 $W \cdot m^{-2}$ occurred on December 31, 2009, following a snow storm in the afternoon of that day. Increased surface temperature during that time resulted in almost immediate meltdown increasing the heat loss from the ground. During January

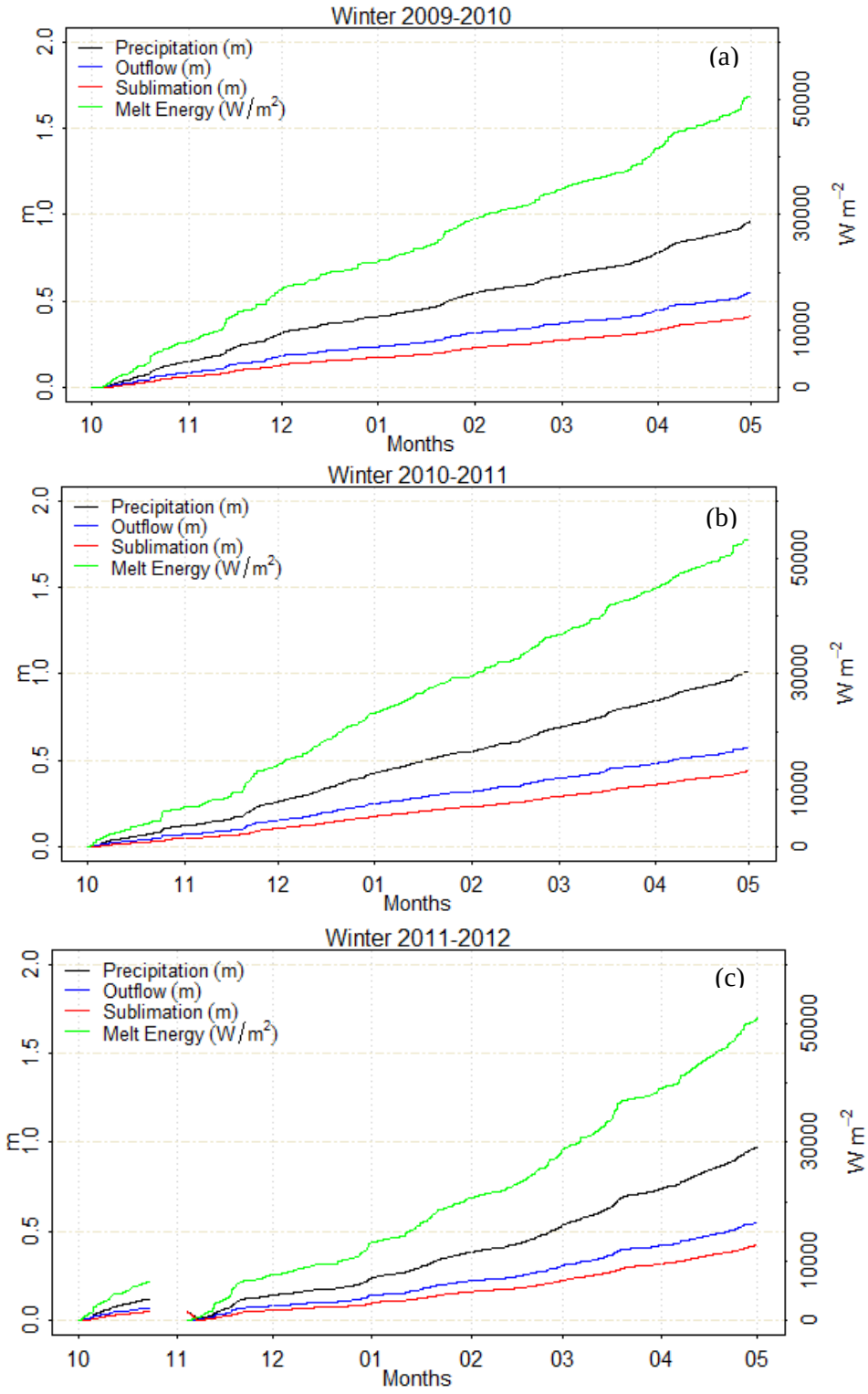

Fig. 2.4. results from the UEB Model showing accumulated snow outflow (m), accumulated sublimation (m), and accumulated melt energy ($W \cdot m^{-2}$) during a) 2009-2010 winter, b) 2010-2011 winter, and c) 2011-2012 winter.

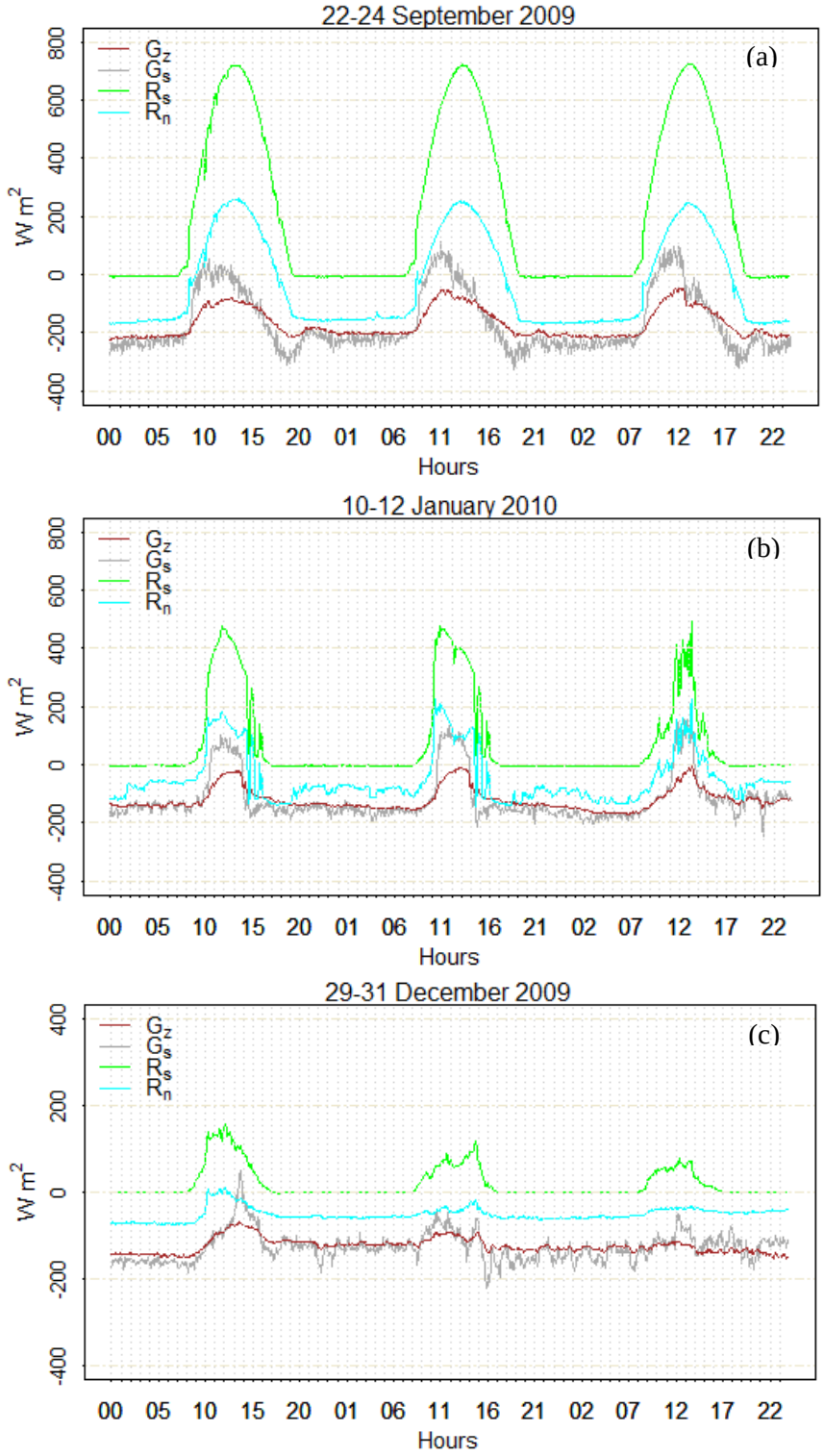

Fig. 2.5. Observed R_s, R_n, G_s and G_z values on the selected consecutive days (a) September 22-24, 2009 (b) January 10-12, 2010 (c) December 29-31, 2009 (d) January 4-6, 2011.

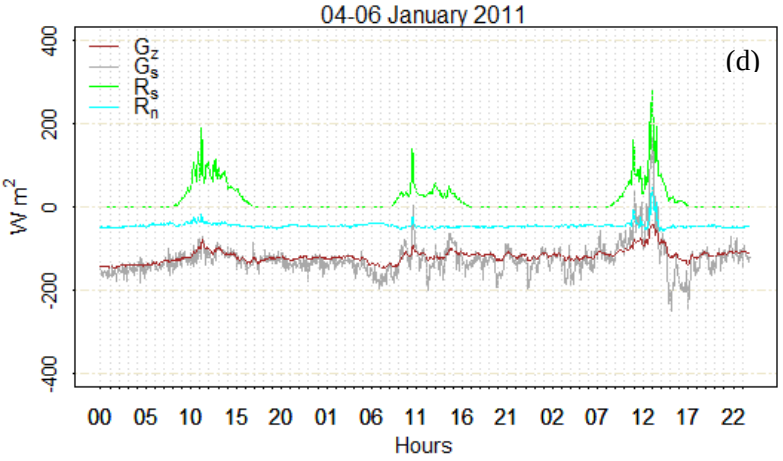

Fig. 2.5. (continued).

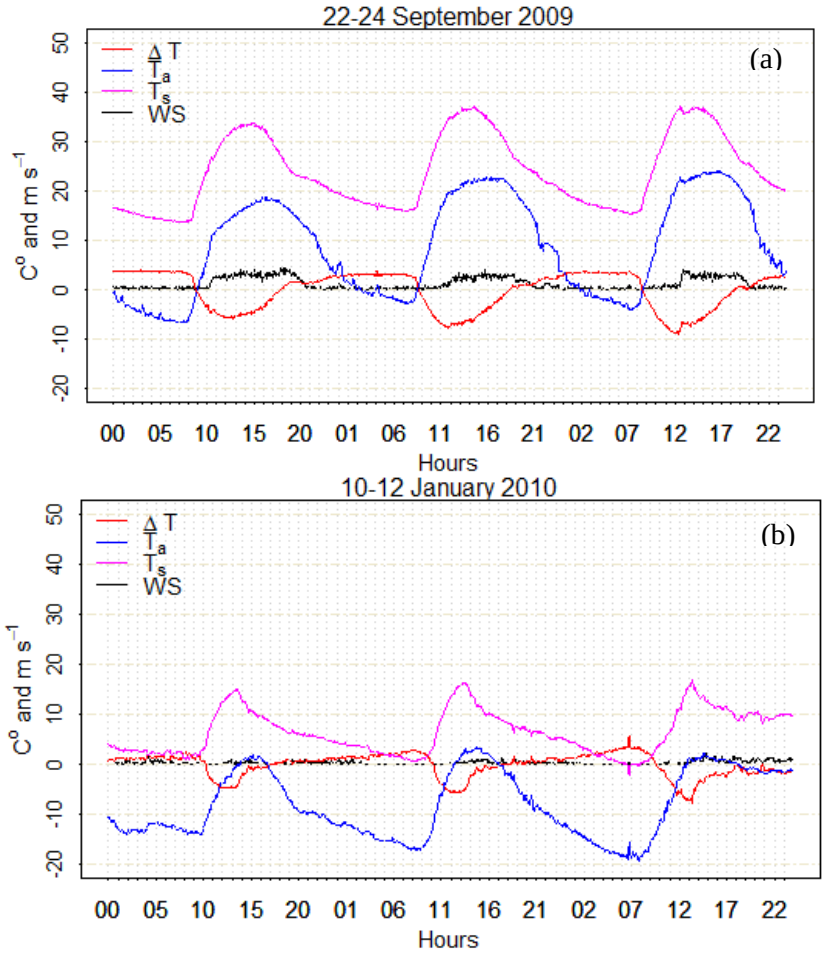

Fig. 2.6. Observed T_a (°C), T_s (°C), ΔT (°C), and WS (m·s^{-1}) values on the selected consecutive days (a) September 22-24, 2009 (b) January 10-12, 2010 (c) December 29-31, 2009 (d) January 4-6, 2011.

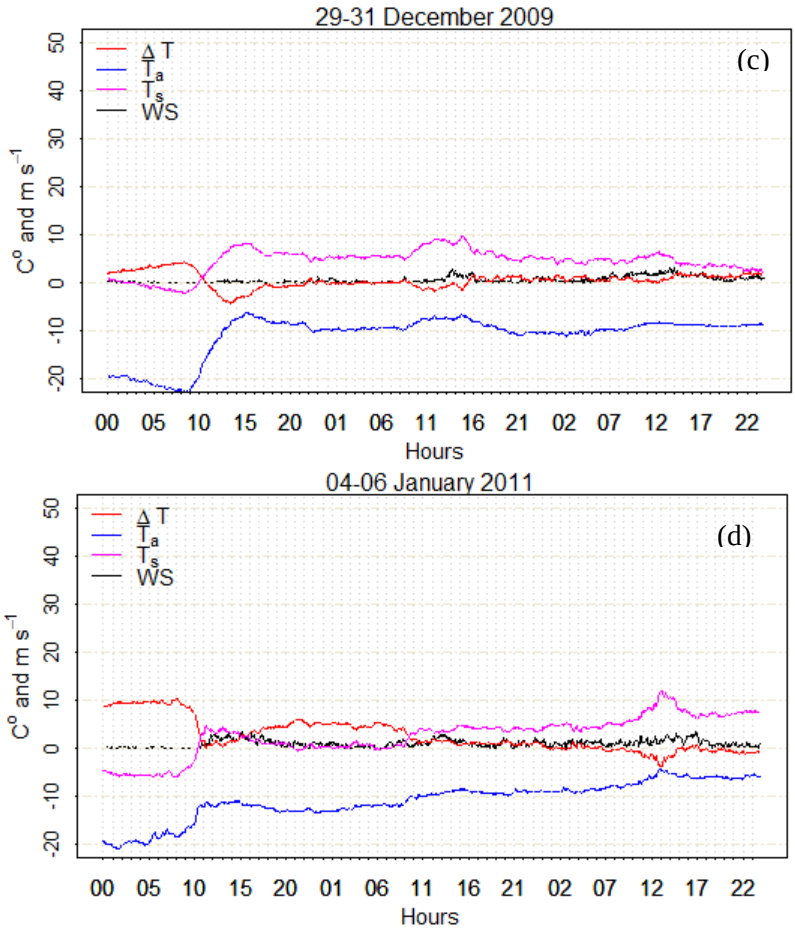

Fig. 2.6. (continued).

10-2, 2010, maximum heat loss of 47.1 W·m^{-2} occurred on January 11 following two events of precipitation. Precipitation depth during January 04-06, 2011, was similar as the former January 2010 days. Maximum heat loos occurred during January 06 as ground temperature was relatively high compared to the previous two days and heat loss through sublimation was notably lower compared to the former days (Fig. 2.7).

2.5. Discussion

The ground heat flux, G_z, measured at the CR3000 and CR1000 sites was generally consistent (Figs. A-1 to A-8 in Appendix A). The heat flux values had similar

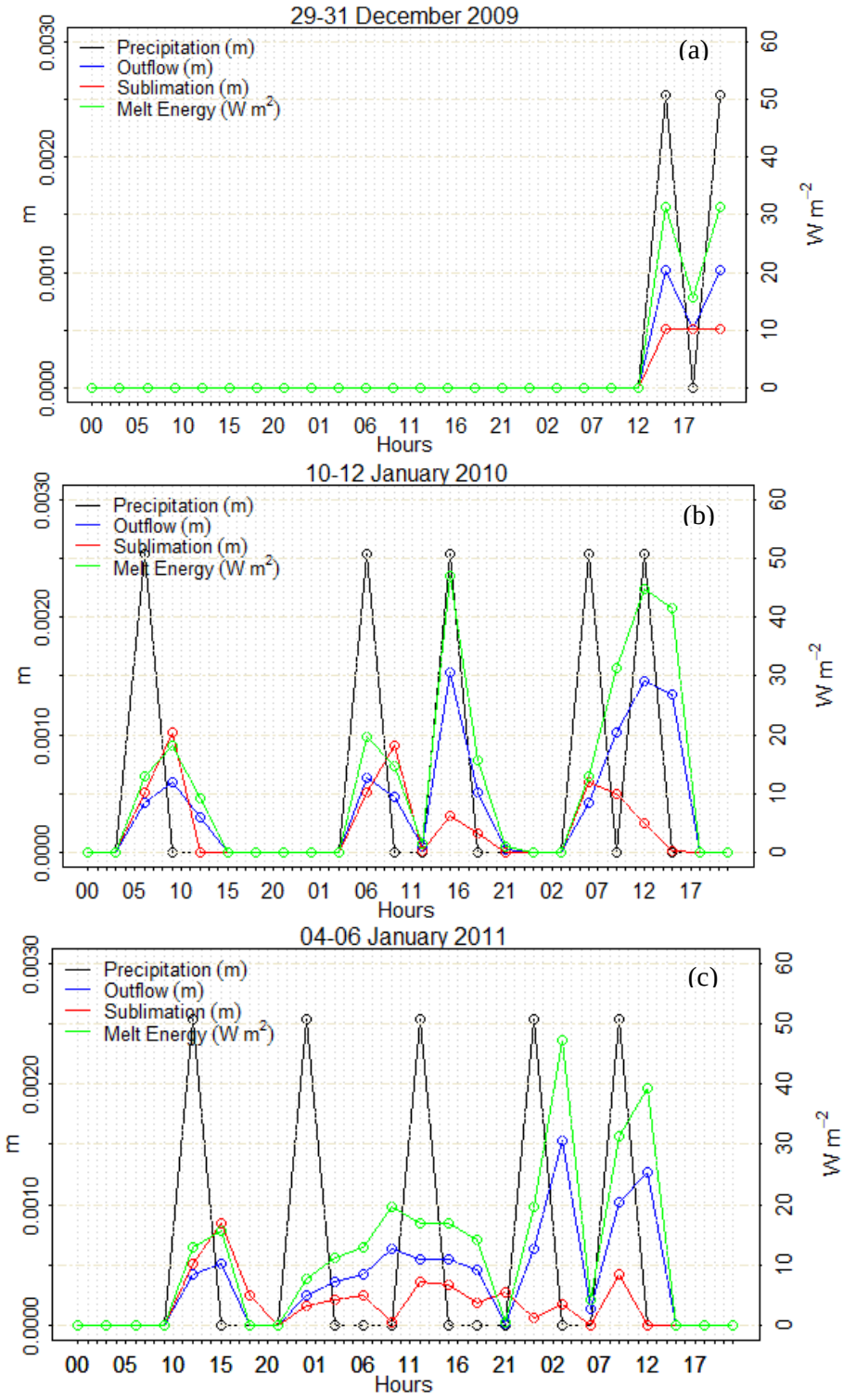

Fig. 2.6. results from the Utah Energy Balance Snow Accumulation and Melt Model showing precipitation (m), outflow, sublimation (m), and melt energy ($W \cdot m^{-2}$) during a) 29-31 December, 2009, b) 10-12 January, 2010, and c) 04-06 January, 2011.

trend and seasonal patterns except for the anomalous spikes observed at the CR3000 site after precipitation (up to -400 $W \cdot m^{-2}$ on some days). The abrupt increase in water content and/or change in soil temperature after precipitation may explain the spikes in G_z. Several soil characteristics may affect the movement of water in the soil, including soil texture and soil aggregation. The soil at the CR3000 site was a hydrothermally altered siliceous sinter rock and contained relatively large rocks. The grain size distribution of that soil was 52.4% sand, 30.7% silt, and 16.9% clay and was classified as loam. The soil at the CR1000 site was a formation of sediment with visibly finer particles compared to that at the CR3000 site. The grain size distribution of that soil was 35.4% sand, 34.2% clay, and 30.4% silt, and was classified as clay loam. The presence of rocks in the soil at the CR3000 site and the increased percentage of sand particles may have enabled abrupt increase in water content and decrease in soil temperature above the impervious plate that may be related to the spikes in G_z values. On the other hand, the parallel anomalous increase in G_z, T_z and R_l observed on the days between January 11 and February 1, 2010 and on the days between September 6 and 20, 2010, occurred only at the CR3000 site. The parallel increase of these three parameters indicate a local increase in the thermal heat at the CR3000 site. An increase in thermal activity may be related to the swarm of small earthquakes of magnitude 2.7 occurred on the evening of January 17 and morning of January 18, 2010, at west Yellowstone as reported by Utah Seismograph Stations (Utah, 2007). The swarm was located about 10 miles northwest of Old Faithful, 9 miles southeast of West Yellowstone. This swarm continued until February 3, 2010. The anomalous increase of G_z, T_z, and R_l at only the CR3000 site observed between the weeks

of January 11, 2010 and February 1, 2010 may relate to the increase thermal activity during this period. However, no major increase in seismic activity was observed between September 6 and 20, 2010.

2.5.1. Diurnal Heat Flux from Solar and Atmospheric Radiations during Selected Summer and Winter Days

The average value of the conductive heat flux due to solar and atmospheric longwave radiation was estimated by comparing the ground surface heat flux, G_s, on selected summer and winter days during times with no or low energy gain through the surface ($-R_n$ and $+\Delta T$). In this case, G_s flowing from the subsurface to the ground surface was comprised of the conductive heat stored in the ground from solar and atmospheric radiation and the near-surface geothermal heat flux. In Fig. (2.8), the blue dots represent G_s during times with $-R_n$ and $+\Delta T$, the red dots represent G_s during times with $+R_n$ and $-\Delta T$, and the green dots represent G_s during times when both R_n and ΔT were positive or negative. For example, when R_n and ΔT were both positive on 22-24 September 2009, temperature at 0.05 m depth was higher than the surface temperature although the ground surface gained heat. This condition occurred during the time lag needed for the soil layer above the temperature probe to warm up after sunrise and to cool down after sunset.

On September 22-24, 2009, the average G_s values during times with $+R_n$ and $-\Delta T$ (red dots) were -62.0 ± 97.8 W·m^{-2}, -52.7 ± 93.9 W·m^{-2}, and -60.0 ± 99.6 W·m^{-2}, respectively (Fig. 2.8.a). The large variability is explained by the variability of the incoming solar radiation during these days. After sunset, the average G_s during times with $-R_n$ and $+\Delta T$ (blue dots) were -230.3 ± 30.9 W·m^{-2}, -229.2 ± 26.3 W·m^{-2}, and -237.5

± 24 $W \cdot m^{-2}$, respectively. The standard deviation values were low compared to those observed during the day, indicating that the heat loss through the ground surface to the atmosphere was relatively stable.

The conductive heat flux stored in the soil from solar radiation was expected to be low during the overcast days of January 10-12, 2010 compared to the former sunny summer days due to low R_s values (maximum was about 500 $W \cdot m^{-2}$), and short sunshine hours. After adding the heat loss from meltwater (Q_m) to G_s values, the difference between the averages of the new G_s during times with $-R_n$ and $+\Delta T$ was about 48 $W \cdot m^{-2}$. This difference can be related to the difference in the heat flux stored in the ground from solar and atmospheric radiation since both latent heat and sensible heat are lost to the atmosphere.

On December 30, 2009 and January 4-5, 2011, maximum R_s values were less than 200 $W \cdot m^{-2}$, and R_n was negative and ΔT was positive for the entire day. Average G_s during times with $-R_n$ and $+\Delta T$ were -150.5 ± 22.1 $W \cdot m^{-2}$ on December 30, 2009; and -139.1 ± 19.3 $W \cdot m^{-2}$ and -146.1 ± 18.4 $W \cdot m^{-2}$, on January 4 and 5, 2011, respectively (Fig. 2.9). These values were statistically similar and fell within the same interquartile range. Since R_n was continuously negative during these days and air temperature was below freezing, the increased subsurface temperature was attributed to the geothermal gradient. Given the previous weather and surface radiation conditions on December 30, 2009 and January 4-5, 2011, the stored heat flux from solar and atmospheric radiation was expected to be a negligible fraction of the measured ground heat flux. The average of G_s values during times with $-R_n$ and $+\Delta T$ on the former days was 142.7 ± 25.2 $W \cdot m^{-2}$. The

result from this study reveal a difference between the averages of G_s values during times with $-R_n$ and $+\Delta T$ on the sunny clear summer days of September 22-24, 2009 and on December 30, 2009 and January 04-06, 2011, as -89.2 ± 21.0 $W \cdot m^{-2}$. This range was assumed representative of the average heat flux stored at the ground surface due to solar and/or atmospheric radiation, during the former sunny summer days. The standard deviation associated with this value (21.0 $W \cdot m^{-2}$) was calculated as the average of the two standard deviations associated with average G_s values estimated for the sunny and overcast days (20.7 $W \cdot m^{-2}$ and 25.2 $W \cdot m^{-2}$). If the standard deviation is calculated as the square root of the two variances, the average G_s is -89.2 ± 32.6 $W \cdot m^{-2}$.

2.5.2. Seasonal Heat Flux from Solar and Atmospheric Radiation

Seasonal analysis of G_s during times with potential low heat flux from solar and atmospheric radiation ($-R_n$ and $+\Delta T$), after adding Q_m values was estimated for the period between August 15, 2009 and July 2, 2012. The values were classified into meteorological seasons of northern hemisphere (i.e. spring between March 1 and May 31, summer between June 1 and August 31, fall between September 1 and November 30, and winter between December 1 and February 28). The average values of Q_m, estimated from the hourly outflow values, was assumed uniformly distributed during that hour. These values were added to the values of G_s to compensate for the heat loss from snowmelt. The histograms of the averages showing the frequencies of the G_s values with $-R_n$ and $+ \Delta T$, after adding Q_m, are displayed in Fig. (2.10). The breakpoints in the histograms were set to a range of 100 $W \cdot m^{-2}$. Lower ranges generally represent values during times with cloudy conditions when incident solar radiation was likely low. Alternatively, higher

ranges are equivalent to sunny days with clear skies or to times with anomalous increase in G_s. For summer months, the range between -200 and -300 $W \cdot m^{-2}$ had the highest frequency with approximately 52−84% of the observations fell within that range. In winter months, the range between -100 and -200 $W \cdot m^{-2}$ had approximately 72−89% of the observations. The range between -200 and -300 $W \cdot m^{-2}$ had lower frequencies with approximately 8 to 16% of the observations fell in that range. In the fall months of 2009 and 2011, more than 50% of the observations fell between -200 and -300 $W \cdot m^{-2}$. In Fall of 2010, more than 15% of the values were greater than 300 $W \cdot m^{-2}$ which is explained by the anomalous increase in G_z, T_s, and R_l' between September 6 and 20, 2010. The seasonal analysis suggests that the difference between the values during summer months and winter months was in the range of 100 $W \cdot m^{-2}$. This difference was consistent with the diurnal average of the values (-89.2 ± 21.0 $W \cdot m^{-2}$) suggesting that the seasonal difference was due to effect from solar radiation.

2.5.3. Comparison of Ground Heat Flux with Previous Studies

To validate the estimated average heat flux due to solar radiation (-89.2 ± 21.0 $W \cdot m^{-2}$), this average was compared to the average of values measured or estimated on previous studies on non-geothermal grounds. Studies on soil heat flux in non-geothermal grounds are available in the literature for different types of soil, climate and topography. Soil temperature and energy exchanges between the soil and the atmosphere are affected by soil physical, thermal, and hydraulic properties and meteorological conditions. Surface albedo is an important parameter in the energy balance at the ground-atmosphere boundary as it controls the fraction of solar energy reflected from the ground surface back

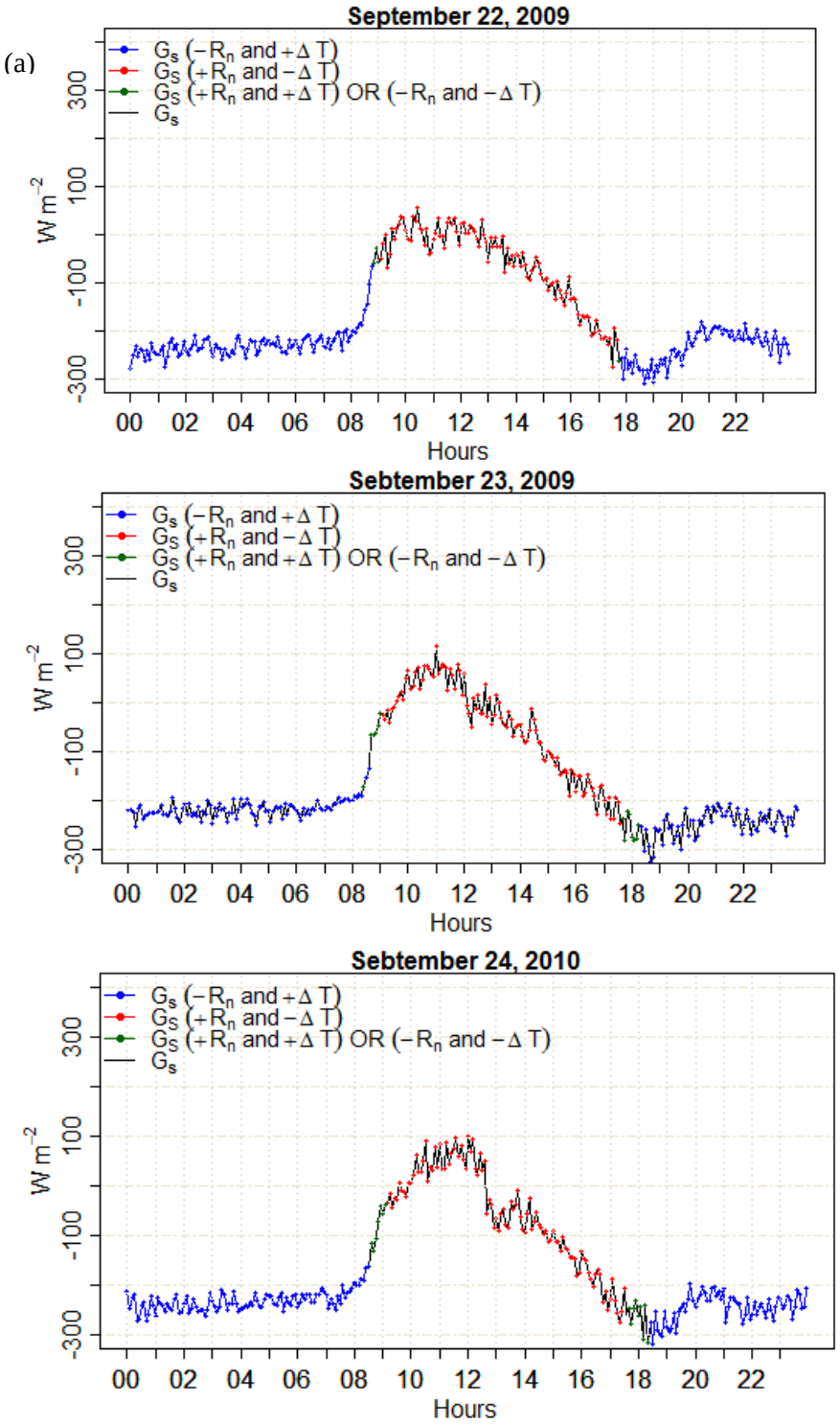

Fig. 2.7. Plots show G_s corresponding to $+R_n$ and $-\Delta T$ (blue), G_s corresponding to $-R_n$ and $+\Delta T$ (red), and G_s corresponding to $+R_n$ and $+\Delta T$ or $-R_n$ and $-\Delta T$ (green), (a) 22-24 Sep 2009, (b) 10-12 Jan 2010, (c) 29-31 Dec 2009, (d) 04-06 Jan 2011. The black line represent G_s before adding the energy loss by snowmelt.

(b)

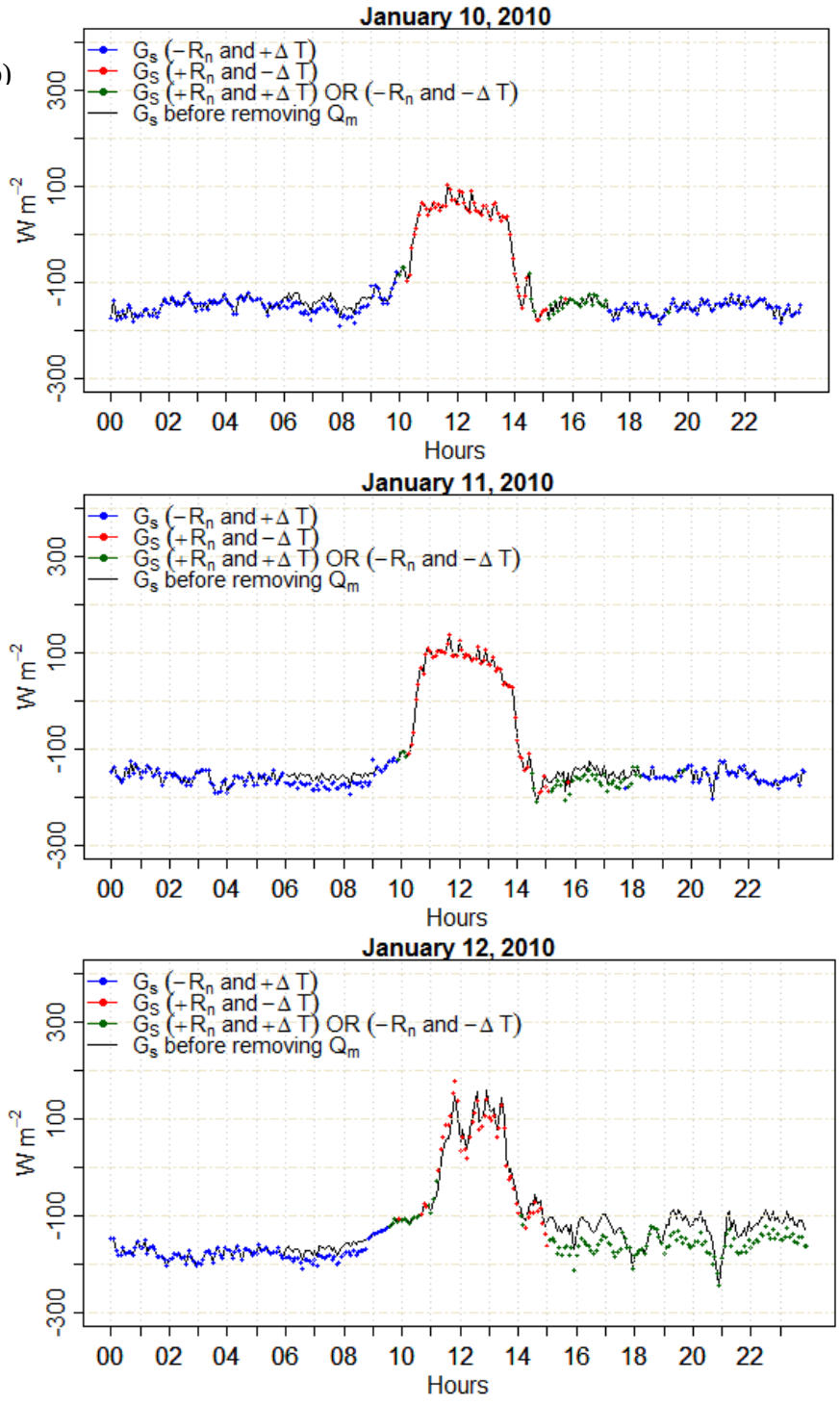

Fig. 2.8. (continued).

(c)

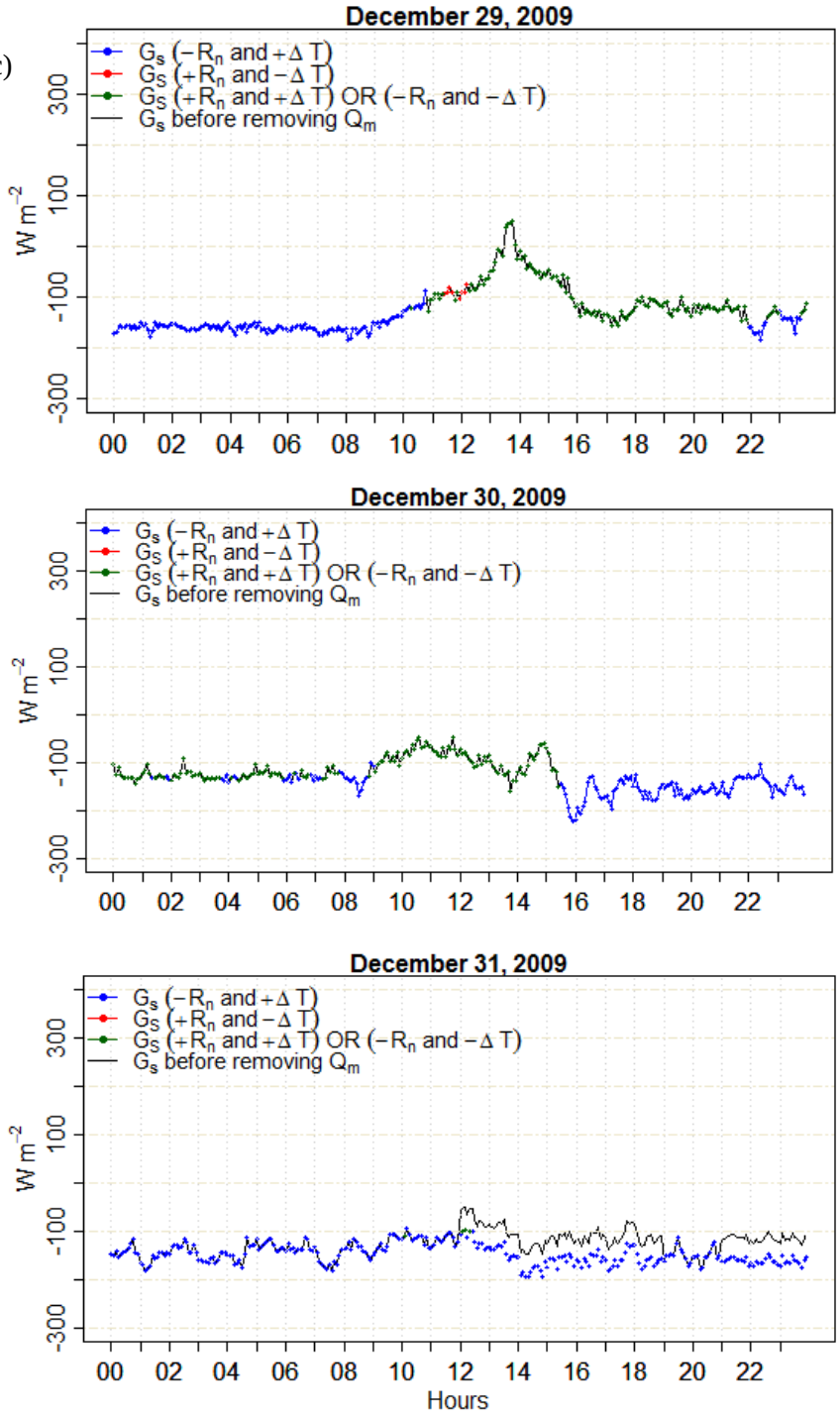

Fig. 2.8. (continued).

(d)

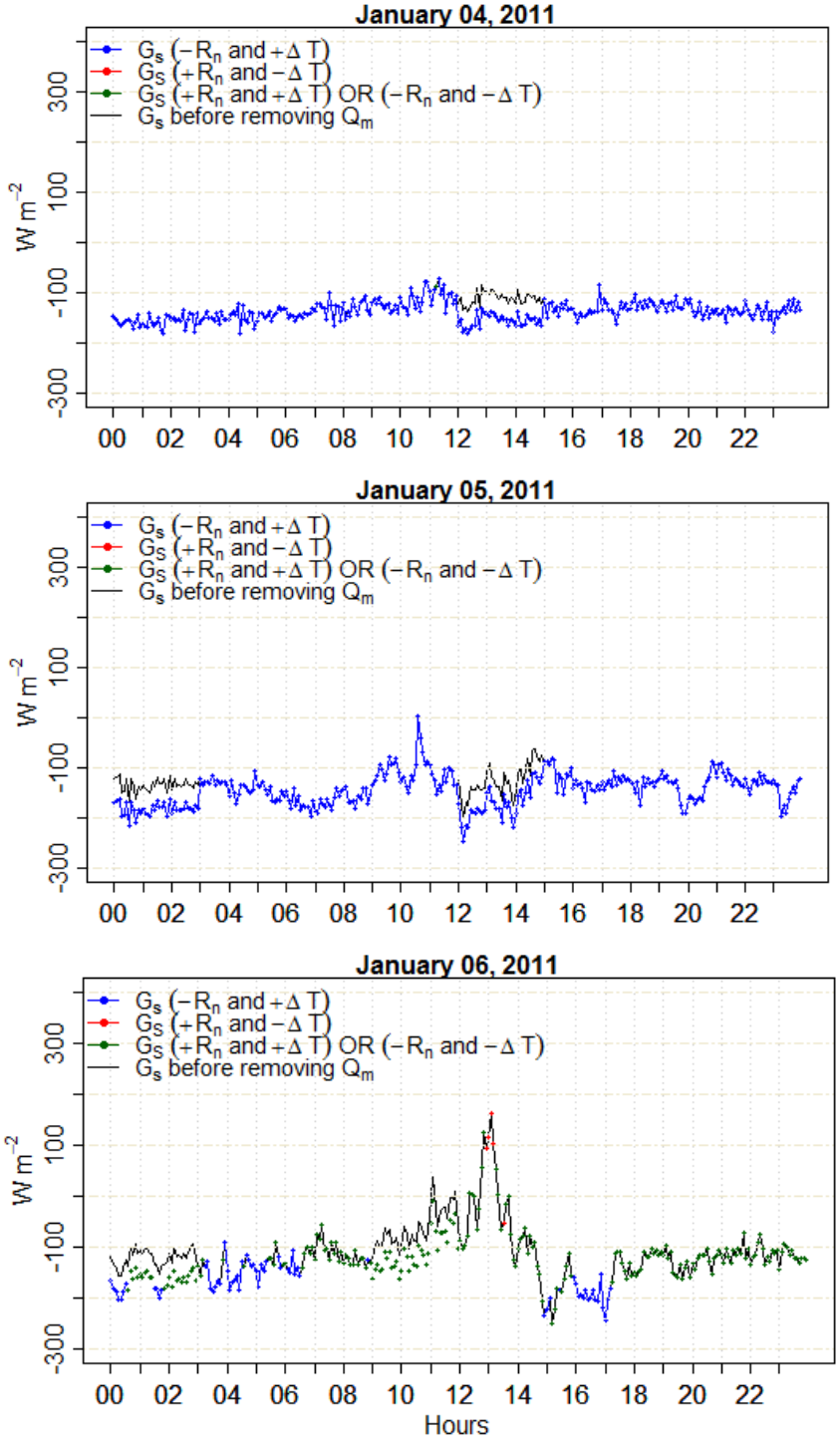

Fig. 2.8. (continued).

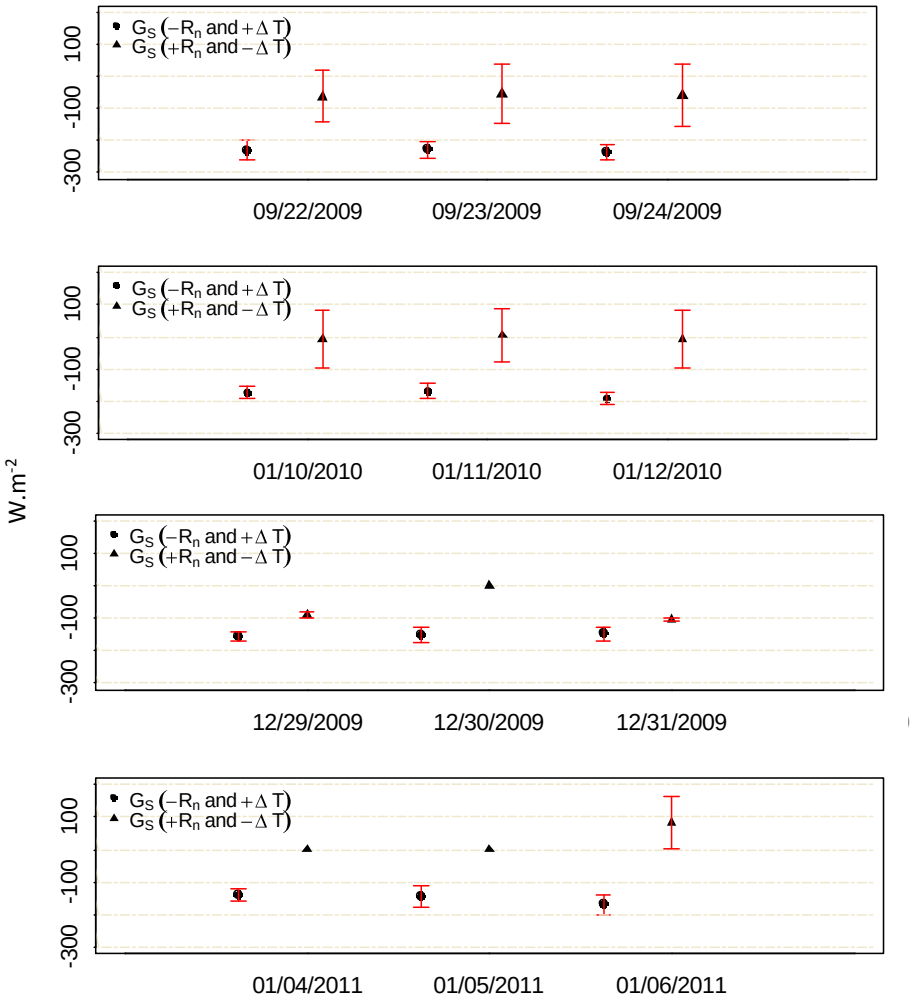

Fig. 2.8. The average ground heat flux (G_s) during times with -R_n and +ΔT (circle) and +R_n and -ΔT (triangle). The error bar represents the standard deviation.

to the atmosphere. Cellier et al. (1996) measured soil heat flux in bare ground near Laon, France. The albedo of the chalky soil in their study site was similar to the albedo of the siliceous sinter soil at the CR3000 site (Table 2.2). Maximum solar radiation on the sunny day of measurement on April 28, 1991, was approximately 805 W·m^{-2}. The Minimum soil heat flux measured during the night at the ground surface was approximately -75 W·m^{-2}. Another study of soil heat flux on non-vegetated area was

conducted by Heusinkveld et al. (2004) in Negev, Israel. Maximum solar radiation on the mostly sunny day of October 16, 2000, was about 770 $W \cdot m^{-2}$. The soil had high albedo similar to the soil at the CR3000 site. The minimum soil heat flux values during the night of that day was approximately -70 $W \cdot m^{-2}$. The soil from Santanello Jr and Friedl (2003) had relatively lower albedo compared to the soil at

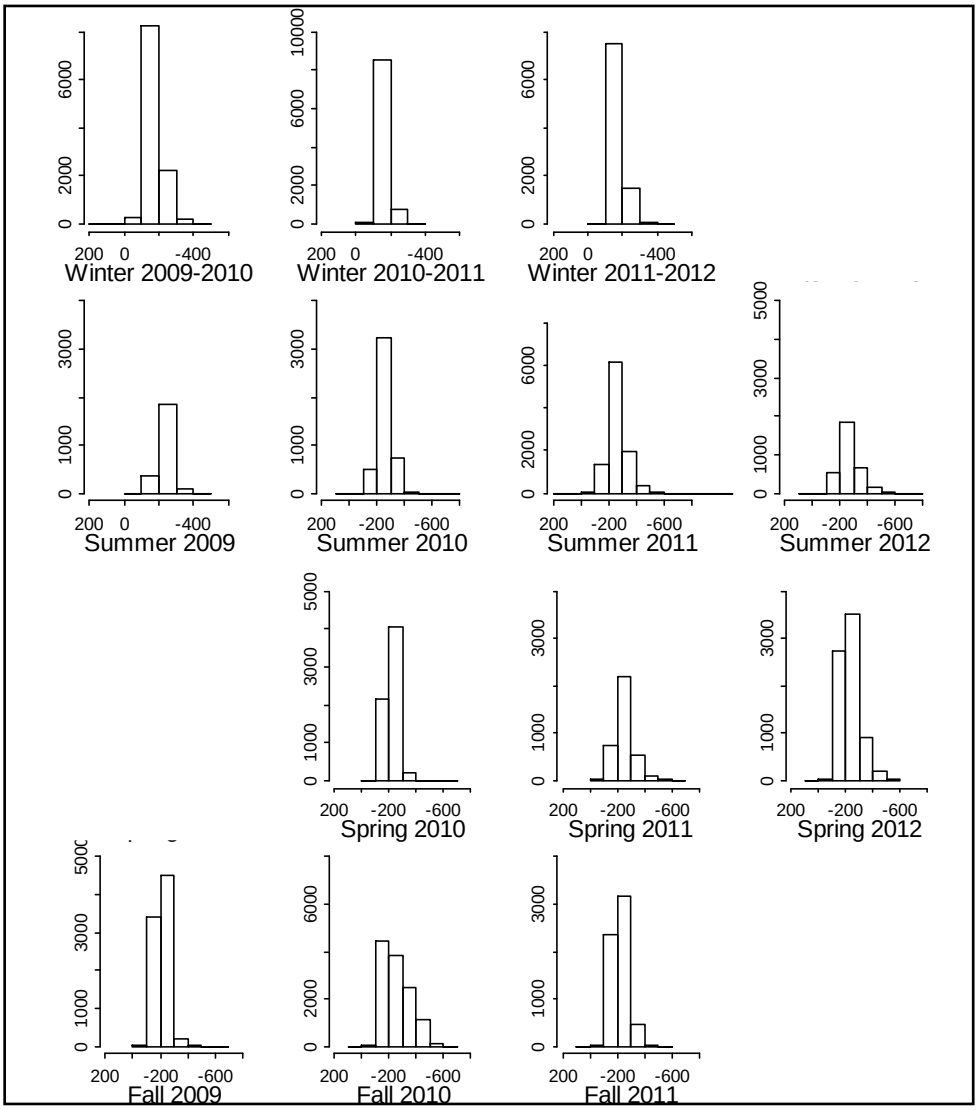

Fig. 2.9. Seasonal histogram showing the frequencies of G_s corresponding to $-R_n$ and $+\Delta T$ after adding Q_m. Seasons were classified according to the meteorological seasons for the northern hemisphere from August 2009 to July 2012.

CR3000 (Table 2.2). Maximum incoming solar radiation during the time of measurement on August 9, 1991 was ~1000 $W \cdot m^{-2}$. The minimum soil heat flux during the night of that day was approximately -90 $W \cdot m^{-2}$. Although the previous studies were conducted in different geographic areas with different climate and altitude and in different months, the ground heat flux had a range of minimum soil heat flux between -70 and -90 $W \cdot m^{-2}$ for a range of surface albedo between 0.4 and 0.22; and a range of incoming solar radiation between 770 and 1000 $W \cdot m^{-2}$. In non-geothermal grounds, soil heat flux measured during the night is solely due to the effect of solar and atmospheric radiation. The later range (~70-90 $W \cdot m^{-2}$) fell within the average of G_s during $-R_n$ and $+\Delta T$ (-89.2 ± 21.0 $W \cdot m^{-2}$) estimated from the comparison between the sunny summer days and the overcast winter days as discussed previously.

2.5.4. Estimation of Average Radiant Geothermal Heat Flux using Thermal Infrared Remote Sensing Images

The main purpose of this study was to develop a method to estimate the conductive heat flux stored in the ground due to solar and atmospheric radiations using surface and near-surface measurements. The ground-based experiment was conducted to help remove the radiant effect due to solar and atmospheric radiations from the remote sensing TIR images in NGB. The TIR images are usually acquired during night time hours of mostly sunny days to avoid the effect from clouds and atmospheric longwave radiation. The total radiant flux estimated from the TIR images is a combination of the radiant flux due to solar and atmospheric radiations and the radiant geothermal flux. Estimation of the radiant geothermal flux may be achieved assuming that the ratio between the estimated conductive heat flux and radiant flux due to solar and atmospheric

Table 2.2.

Soil thermal properties and albedo from different previous studies

Reference	Site	Date of Measurement	Elevation ASL (m)	Maximum R_s ($W \cdot m^{-2}$)	Maximum Albedo	Minimum G_s ($W \cdot m^{-2}$)
This Study	Norris, WY	September 22, 2009	2279.3	770	0.36	~ -230.1
Cellier et al. (1996)	Laon, France	April 28, 1991	104.2	~805	0.31	~ -75
Heusinkveld et al. (2004)	Negev, Israel	October 16, 2000	198.7	~770	0.4	~ -70
Santanello Jr and Friedl (2003)	Walnut Gulch, Arizona	August 09, 1991	1179.6	~1000	0.22	~ -90

radiation equals the ratio between the estimated conductive heat flux at the ground surface and the total radiant flux estimated from the TIR images.

$$\frac{Conductive\ Heat\ Flux\ due\ to\ solar\ radiation}{Radiant\ Flux\ due\ to\ solar\ radiation} = \frac{Ground\ \ Heat\ Flux\ at\ the\ surface\ (G_S)}{Total\ Radiant\ Flux\ from\ TIR\ Images} \quad (15)$$

And

$$\frac{Conductive\ Geothermal\ Heat\ Flux\ at\ the\ surface}{Radiant\ Geothermal\ Flux} = \frac{Ground\ \ Heat\ Flux\ at\ the\ surface\ (G_S)}{Total\ Radiant\ Flux\ from\ TIR\ Images} \quad (16)$$

The ratio between the estimated conductive heat flux at the ground surface (G_s) and the radiant flux estimated from the TIR image (G) at and around the pixel where the heat flux plate was installed was approximately consistent (Table 2.3). However, in this study the radiant flux in the ground from stored solar radiation was estimated for soil with siliceous sinter characteristics, therefore this method is suggested for bare sinter soil areas with similar albedo as the siliceous sinter in the study site. In general, areas covered with siliceous sinter soil surround hot hydrothermal features in YNP. Therefore, study of the temporal changes in the radiant temperature and/or radiant flux on areas covered with

siliceous sinter, after removing the radiant effect from stored solar and atmospheric radiations, can provide an indication of changes within the adjacent hydrothermal systems. Multispectral images in multiple wavelengths of the visible and near infrared spectrum can be used to classify the surface into different classes with similar reflectance values including the siliceous sinter (Yuan and Bauer, 2006). Estimating the radiant geothermal flux is essential to study possible temporal and/or spatial changes within the geothermal system after removing the radiant flux from solar and atmospheric radiations.

Two examples of TIR images were used to estimate the average value of the radiant geothermal flux. The images were acquired in NGB on September 10, 2009, after midnight, and on March 9, 2012, at around 9 pm. The TIR images had a spatial resolution of approximately 1 m*1 m. To account for the spatial error within the image, the average radiant flux (G) was calculated for the six pixels around the location of the heat flux plate.

The ground-based measurements were collected during the day prior to image acquisition, on September 9, 2009, and on March 9, 2012, as displayed in Fig. (2.11) and Table (2.3). September 9, 2009, was mostly sunny. On the night of the TIR image acquisition on September 10, 2009, the average G_s during $-R_n$ and $+\Delta T$ was -234.1 ± 20.6 $W \cdot m^{-2}$. This value was statistically similar to the average value estimated during September 22-24, 2009 (-231.8 ± 20.7 $W \cdot m^{-2}$). Therefore, the residual conductive heat from stored solar and atmospheric radiations was expected to be in the same range of the former days (89.2 ± 21.0 $W \cdot m^{-2}$). The average radiant flux (G) from 2009 image was estimated as 425.3 ± 0.4 $W \cdot m^{-2}$. The ratio between the average G_s and G was

approximately 0.55. Using eq. (15), the average residual radiant flux is estimated at 162.1 $W \cdot m^{-2}$ (with range between 124 $W \cdot m^{-2}$ and 200.2 $W \cdot m^{-2}$). This range is larger (i.e. between 102.8 $W \cdot m^{-2}$ and 221.4 $W \cdot m^{-2}$) if the standard deviation was calculated as the square root of the two variances of G_s values corresponds to $-R_n$ and $+\Delta T$, estimated for the sunny and overcast days as explained in the previous section. The maximum radiant residual flux value in this case is 221.4 $W \cdot m^{-2}$. The minimum radiant geothermal flux was estimated as approximately 203.8 $W \cdot m^{-2}$ after subtracting the maximum radiant flux value (221.4 $W \cdot m^{-2}$) from the total radiant flux (425.3 $W \cdot m^{-2}$). Using eq. (16), the minimum conductive geothermal heat flux was then estimated as 112.1 $W \cdot m^{-2}$ which is in the lower range of G_s value during $-R_n$ and $+ \Delta T$ estimated on December 30, 2009, and January 4 and 5, 2011 (142.7 ± 25.2 $W \cdot m^{-2}$).

On March 9, 2012, the difference between the average G_s during $-R_n$ and $+\Delta T$ (-169.2 ± 15.5 $W \cdot m^{-2}$) and the average estimated on December 30, 2009 and January 4 and 5, 2011 (142.7 ± 25.2 $W \cdot m^{-2}$) was (approximately 26.5 ± 23.9 $W \cdot m^{-2}$). According to the comparison method this difference represents the average heat flux due to solar and atmospheric radiation. Using this average value and the ratio between G_s and G in eq. (15), the average radiant flux due to solar and atmospheric radiation was 46.6 $W \cdot m^{-2}$. The range of the radiant flux due to solar and atmospheric radiation was 4.7 $W \cdot m^{-2}$ and 88.5 $W \cdot m^{-2}$. Subtracting the maximum radiant flux value (88.5 $W \cdot m^{-2}$) from the total radiant flux (297.6 $W \cdot m^{-2}$) gives an estimate of the minimum radiant geothermal heat flux as approximately 209.1 $W \cdot m^{-2}$. Using eq. (16), the minimum conductive geothermal heat flux was then estimated as 119.2 $W \cdot m^{-2}$ which is in the lower range of G_s value during -

R_n and $+\Delta T$ estimated on December 30, 2009, and January 4 and 5, 2011 (142.65 ± 25.21 $W \cdot m^{-2}$). Given the variability of weather conditions and the between-acquisitions difference, the estimated values of minimum conductive geothermal heat flux during the two flight periods (112.1 $W \cdot m^{-2}$ and 119.2 $W \cdot m^{-2}$) and radiant geothermal heat flux (203.8 $W \cdot m^{-2}$ and 209.1 $W \cdot m^{-2}$), are considered fairly similar.

2.5.5. Possible Sources of Uncertainty

The comparison method suggested in this study to estimate the heat stored in the soil due to solar radiation assumed that the geothermal heat flux was constant and the bulk of the change in ground heat flux was due to surface energy. The seasonal comparison of ground heat flux during times with $-R_n$ and $+\Delta T$ suggested that this assumption might be true as the seasonal difference in the ground heat flux values was mostly consistent. However, in Norris Geyser Basin, change in geothermal heat can be rabid and unpredictable.

In this study, uncertainty in the data can be related to, first, the ground-based experiment and, second, the remote sensing method. The uncertainty related to the ground-based experiment includes using the calorimetric heat storage method to estimate soil heat storage above the heat flux plate. This method integrates the ground temperature over the depth overlaying the heat flux plate to estimate the heat storage above the plate. The accuracy of the estimates of the ground heat storage increases when soil temperature is measured at multiple depths. Massman (1992) stated that the standard calorimetric correction may have ±3% to 10% errors when assuming the change in temperature of the soil layer above the plate is approximated by the average temperature at the midpoint. In

Table 2.3.

Average of ground-based data (T_a, T_s, and G_s) during the night before the flight overpass, during $-R_n$ and $+\Delta T$; and radiant flux (G) estimated using the TIR images

Date of Flight Overpass	Time of Flight Overpass	T_a (°C)	T_s (°C)	G_s (W·m-2)	G (W·m^{-2})	G_s/ G
Sep 10, 2009	3:36-3:53 am	11.51 ± 6.23	25.62 ± 3.41	-234.12 ± 20.57	425.25 ± 0.35	0.55
Mar 9, 2012	21:23-21:44 pm	-4.35 ± 8.81	8.93 ± 4.05	-169.19 ± 15.46	297.55 ±1.79	0.57

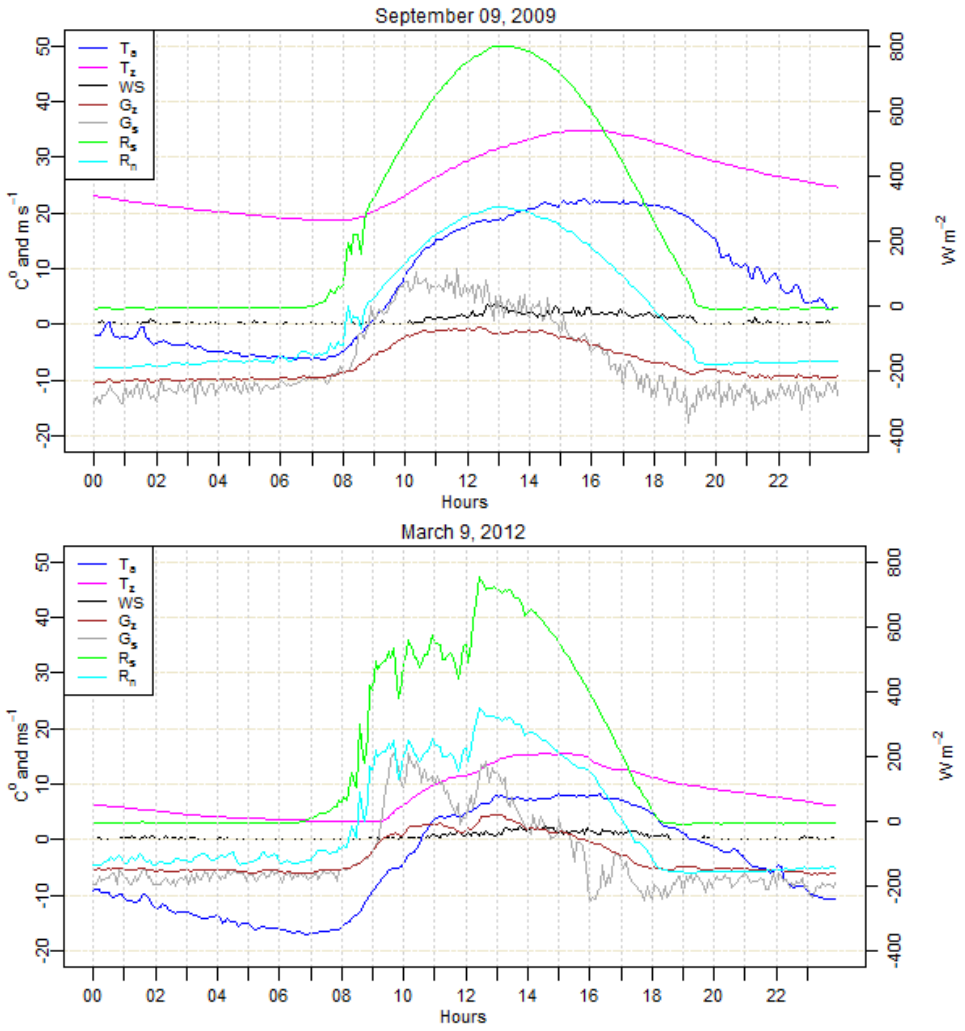

Fig. 2.11. Temperature and flux data for the days of airborne TIR remote sensing image acquisition over NGB

this study, the temperature measured at 0.05 m depth is assumed representative of the average temperature between the heat flux location at 0.1 m depth and the ground surface. More accurate results of heat storage and surface ground heat flux surface can be obtained by incorporating temperature at multiple depths in the heat storage calculation (Weber, 2006).

Uncertainty can be introduced, when surface skin temperature is estimated using estimates of surface emissivity from ASTER GED database. An uncertainty is expected

from using the emissivity images which had a course resolution of approximately 100 m compared to the relatively small area represented by the heat flux plate. The sensitivity analysis for a range of surface emissivity between 0.86 and 0.89 showed about 2.67 °C difference in the estimated skin temperature. This error may have implication on determining the temperature gradient in the soil and therefore *Gs* values during time with $+\Delta T$.

Uncertainty related to the remote sensing TIR images includes spatial accuracy of the features, temporal consistency of the TIR images, and relevance of the estimated radiometric temperatures to the measured kinetic temperatures. Neale et al. (2016) explained the methods used to produce consistent and accurate TIR images including the methods used for image processing and correction for atmospheric disturbance and emissivity. The spatial accuracy of the TIR images varied in year to year with maximum spatial displacement of 5 m (Neale et al., 2016). To reduce this uncertainty, the radiant flux (G) was calculated for six pixels around the pixel that theoretically overlay the heat flux plate.

2.6. Summary and Conclusions

Frequent monitoring of the thermal activity in active geothermal areas, like Yellowstone National Park, is required to determine possible temporal and/or spatial changes within the system. Airborne remote sensing images have recently been used in YNP to estimate and compare the surface radiant temperature and radiant flux. The challenge remained in comparing year-to year changes in the radiant temperature and radiant flux due to the geothermal source and removing the stored radiant flux resulting

from solar shortwave radiation and atmospheric longwave radiation in the top layer of the ground. In this study, a simple approach was proposed to estimate and remove the stored radiant flux which enabled the estimation of the radiant geothermal flux allowing for comparison among several years of monitoring. Previous methods that were used to estimate the absorbed residual radiant flux, used remote sensing images to estimate the radiant flux from a non-geothermally active area, assuming the source of the radiant flux is solely from stored solar radiation and atmospheric longwave radiation. This method, if applied through airborne remote sensing, will require additional images outside the area of interest, which will add to the overall project cost. Selection of the background non-geothermal area has also been an area of research as it is somewhat challenging to select a background area with surface characteristics similar to the geothermal area which is typically composed of sintered soils. The method used in this chapter was based on a simple comparison between estimates of surface and near-surface conductive heat flux and radiant flux estimated through airborne remote sensing remote sensing. Although the proposed method was based on comparison of average values, the results of the estimated radiant geothermal flux were statistically close. The radiant geothermal flux was estimated using the remote sensing TIR image acquired on 09 September 2009 as 203.8 $W \cdot m^{-2}$ and on 09 March 2011 image as 209.1 $W \cdot m^{-2}$. Given the variability of season and overall weather conditions in between-acquisitions, the difference between the two former values is negligible. The ratio between the conductive heat flux measured by the plate and the radiant flux over the same area surrounding the plate is consistent among the years. So future remote sensing studies can assume that this ratio will hold allowing

the estimates of the solar contributed fluxes to be removed without need for ground measurements. The standard deviation values associated with the conductive heat flux measurements were generally high due to variability in weather conditions. This variability suggested that measurement of the ground heat flux and/or the temperature profile below the diurnal radiant flux zone is important to better quantify changes related to the geothermal source, and to test the proposed method in this chapter to separate surface geothermal heat flux and the residual heat flux. The estimated radiant residual flux values were specific to the days in the analysis and not to all sunny and clear days, as different weather condition (i.e. air temperature and clouds) may have different effect on the ground heat flux.

The results revealed an average of 89.16 ± 21.0 $W \cdot m^{-2}$ as the conductive heat flux due to solar radiation on mostly clear sunny days of 22-24 September 2009. This range was close to the range estimated in previous studies on non-geothermal grounds with similar surface albedo. However, the effect of solar radiation and atmospheric longwave radiation varies according to solar intensity and duration as well as cloud cover. In addition, increase in underlying geothermal heat flux can represent a challenge to distinguish the flux due to solar and atmospheric radiations and the signal from geothermal heat flux.

The continuous monitoring of the ground heat flux and surrogate parameters of heat like surface temperature and upwelling longwave radiation can indicate anomalies in the thermal activity if they occur in a measurable level. Reported seismic activity may be tied to the hydrothermal activity between January 11, 2010 and February 1, 2010.

However, between September 6, 2010 and September 20, 2010 the potential increase in thermal activity was not tied with reported seismic activity and this reasoning might need extra investigation.

References

Abrams, M., 2000. The Advanced Spaceborne Thermal Emission and Reflection Radiometer (ASTER): data products for the high spatial resolution imager on NASA's Terra platform. International Journal of remote sensing, 21(5): 847-859.

Allaby, M., 2013. A dictionary of geology and earth sciences. Oxford University Press.

Cellier, P., Richard, G., Robin, P., 1996. Partition of sensible heat fluxes into bare soil and the atmosphere. Agricultural and forest meteorology, 82(1): 245-265.

Fournier, R.O., White, D.E., Truesdell, A.H., 1976. Convective heat flow in Yellowstone National Park, pp. 731-739.

Friedman, I., Norton, D.R., 2007. Is Yellowstone Losing Its Steam?—Chloride Flux out of Yellowstone National Park.

Fuchs, M., Tanner, C.B., 1968. Calibration and field test of soil heat flux plates. Soil Science Society of America Journal, 32(3): 326-328.

Gentine, P., Entekhabi, D., Heusinkveld, B., 2012. Systematic errors in ground heat flux estimation and their correction. Water Resources Research, 48.

Gill, A.E., 1982. Atmosphere-ocean dynamics. Academic press.

Haselwimmer, C., Prakash, A., 2013. Thermal infrared remote sensing of geothermal systems, Thermal Infrared Remote Sensing. Springer, pp. 453-473.

Heusinkveld, B.G., Jacobs, A.F.G., Holtslag, A.A.M., Berkowicz, S.M., 2004. Surface energy balance closure in an arid region: role of soil heat flux. Agricultural and forest meteorology, 122(1): 21-37.

Hurwitz, S., Harris, R.N., Werner, C.A., Murphy, F., 2012. Heat flow in vapor dominated areas of the Yellowstone Plateau Volcanic Field: Implications for the thermal budget of the Yellowstone Caldera. Journal of Geophysical Research: Solid Earth (1978–2012), 117.

Jaworowski, C., Heasler, H., Neale, C., Saravanan, S., Masih, A., 2013. Temporal and Seasonal Variations of the Hot Spring Basin Hydrothermal System, Yellowstone National Park, USA. Remote Sens-Basel, 5(12): 6587-6610.

Lombardo, V., Buongiorno, M.F., 2013. Analysis of Lava Flow Effusion Rate Using High Spatial Resolution Infrared Data, Thermal Infrared Remote Sensing: Sensors, Methods, Applications. Springer, Oberpfaffenhefen, Germany, pp. 397-401.

Lowenstern, J.B., Hurwitz, S., 2008. Monitoring a supervolcano in repose: Heat and volatile flux at the Yellowstone Caldera. Elements, 4(1): 35-40.

Massman, W.J., 1992. Correcting Errors Associated with Soil Heat-Flux Measurements and Estimating Soil Thermal-Properties from Soil-Temperature and Heat-Flux Plate Data. Agricultural and forest meteorology, 59(3-4): 249-266.

Mayocchi, C.L., Bristow, K.L., 1995. Soil surface heat flux: some general questions and comments on measurements. Agricultural and forest meteorology, 75(1): 43-50.

Millero, F.J., Perron, G., Desnoyers, J., 1973. Heat capacity of seawater solutions from 5° to 35° C and 0.5 to 22‰ chlorinity. Journal of Geophysical Research, 78(21): 4499-4507.

Neale, C.M., Sivarajan, S., Masih, A., Jaworowski, C., Heasler, H., 2011. Estimating heat flow of thermal features in Yellowstone National Park using airborne thermal infrared remote sensing, pp. 1225.

Neale, C.M.U., 2014. Integrated Study of Systematic Monitoring and Mapping Thermal Springs and Features in Yellowstone National Park, Utah State University, Logan, UT.

Neale, C.M.U., Jaworowski, C., Heasler, H., Sivarajan, S., Masih, A., 2016. Hydrothermal monitoring in Yellowstone National Park using airborne thermal infrared remote sensing. Remote Sensing of Environment, 184: 628-644.

Neale, C.M.U., Sivarajan, S., 2011. Integrated Study of Systematic Monitoring and Mapping Thermal Springs and Features in Yellowstone National Park, Remote Sensing Services Lab, Utah State University, Logan, UT.

Ochsner, T.E., Sauer, T.J., Horton, R., 2007. Soil heat storage measurements in energy balance studies. Agronomy journal, 99(1): 311-319.

Santanello Jr, J.A., Friedl, M.A., 2003. Diurnal covariation in soil heat flux and net radiation. Journal of Applied Meteorology, 42(6): 851-862.

Scientific, C., 2003. HFT3 soil heat flux plate instruction manual. Campbell Scientific Inc., Logan, UT.

Seielstad, C., Queen, L., 2009. Thermal Remote Monitoring of the Norris Geyser Basin, Yellowstone National Park. *Final Report for the National Park Service Cooperative Ecosystem Studies Unit, Agreement*(H1200040001), 38.

Sorey, M.L., 2000. Geothermal Development and changes in surfi cial features:, World Geothermal Congress, pp. 705-711.

Stein, C.A., 1995. Heat flow of the Earth. American Geophysical Union Washington DC, pp. 144.

Tarboton, D.G. Luce, C.H., 1996. Utah energy balance snow accumulation and melt model (UEB). Citeseer.

U.S. Department of Agriculture, N.R. and Service, C., 2016. West Yellowstone SNOTEL.

Utah, U.o., 2007. www.seis.utah.edu/EQCENTER/PRESS/yell_press.htm. In: E.I. Center (Editor), www.seis.utah.edu.

Vaughan, R.G., Keszthelyi, L.P., Lowenstern, J.B., Jaworowski, C. Heasler, H., 2012. Use of ASTER and MODIS thermal infrared data to quantify heat flow and hydrothermal change at Yellowstone National Park. Journal of Volcanology and Geothermal Research, 233: 72-89.

Watson, F.G.R., Lockwood, R.E., Newman, W.B., Anderson, T.N., Garrott, R.A., 2008. Development and comparison of Landsat radiometric and snowpack model inversion techniques for estimating geothermal heat flux. Remote Sensing of Environment, 112(2): 471-481.

Weber, S., 2006. Comparison of in-situ measured ground heat fluxes within a heteorogeneous urban ballast layer. Theoretical and applied climatology, 83(1-4): 169-179.

White, D.E., Hutchinson, R.A., Keith, T.E.C., 1988. Geology and remarkable thermal activity of Norris Geyser Basin, Yellowstone National Park, Wyoming. US Geol. Surv., Prof. Pap.;(United States), 75(1456).

Yuan, F., Bauer, M.E., 2006. Mapping impervious surface area using high resolution imagery: A comparison of object-based and per pixel classification

CHAPTER 3

NUMERICAL SIMULATION OF SOIL WATER AND HEAT TRANSPORT WITH VAPOR FLOW IN BARE GROUND IN NORRIS GEYSER BASIN, YELLOWSTONE NATIONAL PARK

Abstract

Studies about heat transport mechanisms and rates in the subsurface of geothermally heated grounds in Yellowstone National Park (YNP) are limited. Such studies are important to determine the contribution of each mechanism in the overall heat transport in these areas as it can related to the magmatic activity in the area. In this study HYDRUS-1D numerical model was used to evaluate the four heat transport mechanisms including conduction of sensible heat, convection of sensible heat by liquid water and water vapor, and convection of latent heat by water vapor in the top 15 cm of siliceous sinter deposit in Norris Geyser Basin (NGB). The model was calibrated to optimize soil hydraulic parameters including the empirical parameters n and α, and saturated hydraulic conductivity (K_s) used in the van Genuchten hydraulic model (Van Genuchten, 1980). The model was calibrated using measured soil water content and soil temperature at 5 cm depth during a 10-days in September 2009 and validated during 10-days in September 2010 and 2011. The results showed that the conductive heat flux dominated the convective heat flux by liquid water and water vapor and latent heat flux by water vapor. The results of the conductive heat flux estimated at the surface matched the results obtained using the calorimetric heat storage method used in Chapter 2. This results

allowed us to better understand the relative importance of the four heat transport mechanisms in the study site. This understanding has implications for the heat budget of Yellowstone's magmatic system and for monitoring the unique hydrothermal activity in YNP.

3.1. Introduction

Understanding the magmatic activity in YNP requires knowledge of the mechanisms and rates of heat transport between the magma and the ground surface. This study provides an evaluation of the heat transport in the top 15 cm of a bare ground covered by thermal siliceous sinter deposit near the explosion crater pool in NGB. The mechanisms of heat transport include, conduction of sensible heat, convection of sensible heat by liquid water and water vapor, and convection of latent heat by water vapor (De Vries, 1958). This study defines these mechanisms and estimate the rates of heat transport below the ground surface resulted partly from the magmatic activity in NGB and from the sun as another source of energy at the ground surface. Also this study provides estimates of the conductive heat flux at multiple depth of the soil profile as part of the total heat flux simulation. Comparison of these results with the estimated ground surface heat flux using the calorimetric heat storage method from Chapter 2, provides an assessment of the two methods. The combined results enable us to better understand the relative significance of each heat transport mechanism in the study site at NGB.

Previous studies on heat transport in YNP estimated the rate of heat transport through a particular mechanism. For example the chloride inventory method has long been used to estimate the rate of heat transport through convection (Fournier et al., 1976;

Friedman and Norton, 2007) . In this method the load of thermal chloride in rivers draining YNP is used as a surrogate of the convective heat power. Remote sensing based studies were successfully implemented to estimate the heat transport through radiation from estimates of radiant surface temperature and surface albedo (Haselwimmer et al., 2011; Neale et al., 2011). Fewer studies estimated the rate of heat transport through multiple mechanisms, as these studies require additional financial and technical arrangements. Recently Hurwitz et al. (2012b) conducted a study in Obsidian Pool Thermal Area and Solfatara Plateau Thermal Area in YNP, to estimate the conductive and advective heat flux trough a low permeability layer capping large vapor reservoir. Their method was implemented by measuring soil temperature profile down to 1 m and analyzing soil samples for different thermal and hydraulic properties along the soil profile, including soil thermal conductivity, porosity, and water saturation. Their method also required measurement of water and water vapor flux through the soil using a weighing and heating method. Collecting the soil core samples for laboratory analysis required extra care to preserve the samples and extra time for the analysis.

Numerical models have been continuously modified to simulate the coupled water flow and heat transport in the vadose zone (Šimůnek and van Genuchten, 2008; Simunek et al., 2005a; Simunek et al., 2005b). In this study the HYDRUS-1D numerical model version 4.16, originally developed by Šimunek et al. (1998), was used to simulate the coupled movement of heat transport, and water and water vapor flow in the top 15 cm of a soil covered with siliceous sinter soil in NGB. Surface energy balance is influenced by liquid water flow and water vapor flow which are strongly coupled with the temperature

of the soil. The heat transport model considers movement of soil heat by conduction, convection of sensible heat by liquid water flow, convection of latent heat by diffusion of water vapor, and convection of sensible heat by diffusion of water vapor as described by De Vries (1958). The model uses various types of meteorological data to evaluate surface and near-surface water and energy balance.

The HYDRUS-1D provides solutions to both direct and inverse problems. Direct problems describe the condition where the initial and boundary conditions and corresponding model hydraulic and/or thermal parameters are known; whereas inverse problems represent the condition where some of the parameters were not determined experimentally (Hopmans et al., 2002; Simunek and Van Genuchten, 1999). HYDRUS-1D implements the Marquardt-Levenberg type parameter estimation technique for inverse estimation of selected soil hydraulic and thermal parameters from measured transient flow and transport data including water content, pressure head, and temperature. The Levenberg-Marquardt function expresses the difference between the observed and predicted parameters and iteratively improve the predicted parameters during a minimization process until a desired degree of precision is obtained (Marquardt, 1963). It was used successfully to optimize hydraulic and thermal parameters when the initial parameters were close to the actual parameters of the soil (Schelle et al., 2012; Wildenschild et al., 2001). Kool et al. (1985) applied the inverse approach by numerical solution of the Richards equation for a one-step outflow experiment. They concluded that uniqueness of the estimated parameters can be lowered if the experiment was designed to cover a wide range of water content. They recommended that initial parameter estimates

must be reasonably close to their true values and that outflow measurement errors must be small. HYDRUS-1D additionally calculates statistical information about the fitted parameters such as the mean, standard error, T-value, and the lower and upper confidence limits

In this study HYDRUS-1D provided a method to optimize several hydraulic parameters including the empirical parameters (n) and (α), and the saturated hydraulic conductivity (K_s) used in van Genuchten model. Initial inputs of hydraulic parameters, thermal parameters estimated from field observations, and meteorological information were used in the model. The results of the optimization have increased our understanding of the hydraulic characteristics of the siliceous sinter deposit at different conditions. The simulated temperature and water content results were evaluated against field soil temperature and water content measurements collected near the explosion crater pool in NGB.

3.1.1. Objectives

This study has three main objectives including 1) optimize and estimate soil hydraulic parameters under different meteorological conditions, 2) estimate the contribution of the different heat transport mechanisms in the overall heat transport in that soil layer, 3) evaluate the calorimetric heat storage method used in Chapter 2 by comparing the conductive heat flux at the ground surface estimated using that method with that estimated using the output parameters from HYDRUS-1D.

3.2. Methods

3.2.1. Study Area

NGB is located in the northwest side of YNP. The explosion crater pool in NGB is located in the western part of the basin near the gap area. The basin is characterized with variable surficial geology and heterogeneous bedrock (Ball et al., 2002a). Lava Creek Tuff accumulates at the ground surface at some location and other locations are covered by clay minerals, siliceous sinter, and ice-contact deposits. The explosion crater pool has a blue-green color which characterizes acid-sulfate waters (Livo et al., 2007; White et al., 1988). The temperature of the pool varies between 30 °C and 43 °C in the summer and between 22 °C and 35 °C in the winter. The soil at and around the study site in the southwest side of the pool is covered by whitish-color siliceous sinter deposits. The siliceous sinter is a deposit of opaline or amorphous silica that occurs around hot springs and geysers as a result of incrustation processes (Campbell et al., 2015). The siliceous sinter is deposited due to the action of algae and other forms of vegetation around the hydrothermal features including fumaroles and hot springs. The maximum soil temperature measured at 5 cm depth in the summer was about 56 °C and in the winter was about 2 °C. The difference in elevation between the bare soil surface and the water surface in the pool was estimated at approximately 1 m during summer months.

3.2.2. Data and Spatial Discretization

Continuous soil and weather data was collected at 5-minute interval at the bare ground located at about 20 m southwest the explosion crater pool (Fig. 3.1). Soil temperature and water content were measured at 5 cm depth and soil heat flux was

measured at 10 cm depth. Soil surface temperature was estimated using 5-minute measurement of upwelling longwave radiation and estimated average surface albedo from ASTER GED database (Abrams, 2000). Air temperature, relative humidity, precipitation, and 4-way radiation, were measured at about 2 m above the location where the soil heat flux and soil temperature and water content were measured. The sensors were mounted on a tripod controlled by a CR3000 data logger manufactured by Campbell Scientific Inc. Soil thermal conductivity, diffusivity, and heat capacity were measured at 9 and 13 cm depth during a site visit in October 2010 using a hand-held KD2 probe. During the same visit, core soil samples were collected at 9 and 13 cm to measure soil water content, porosity, and bulk density. As the siliceous sinter deposit was very dense, it was very hard to collect core soil samples at multiple depth to enable further measurements. The grain size distribution of the soil showed that the soil was loam with percent fractions of 52.4% sand, 30.7% silt, and 16.9% clay. Information about the sensors used for the measurements and their accuracy is given in Table (3.1).

Soil profile was discretized into 101 nodes with 0.15 cm each from the ground surface to the depth of water table at about 1 m (Fig. 3.1). The nodal density was decreased at the top of the profile by a factor of 0.5 to increase the accuracy of the simulation. Four nodes were added to the profile at 0 cm, 5 cm, 10, cm, and 15 cm, to represent the locations where soil temperature and/or water content were measured or estimated (Fig. 12). The profile module in HYDRUS-1D was used to define the spatial distribution of parameters characterizing the flow domain including the initial and boundary conditions.

3.2.3. Numerical Model for Water Flow and Heat Transport

The model solve for the movement of liquid water, water vapor, and heat transport in the subsurface by simultaneously solving the modified Richards equation (eq. 1) for one-dimensional uniform water movement in a partially saturated rigid porous medium, and the one-dimensional heat transfer equation with vapor transfer (eq. 2). The modified Richards equation in partially saturated soil was described by Saito et al. (2006) as

$$\frac{\partial \theta_T(h)}{\partial t} = \frac{\partial}{\partial x}(K + K_{vh})\left(\frac{\partial h}{\partial x} + \cos\beta\right) + (K_{LT} + K_{vT})\frac{\partial T}{\partial x} \quad (1)$$

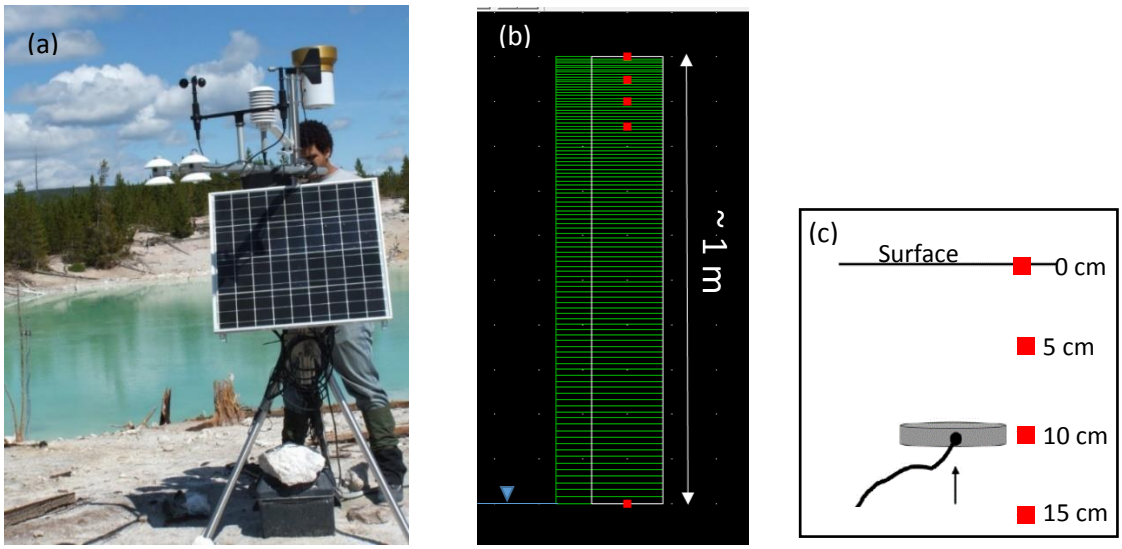

Fig. 3.1. (a) A tripod with weather and radiation sensors installed above a bare ground where soil heat flux is measured at 10 cm depth and soil content and temperature were measured at 5 cm depth, (b) HYDRUS-1D soil profile showing the nodes and water table, (c) simulation of the depth of the four nodes and soil heat flux plate.

where θ_T (m^3/m^3) is total volumetric water content (the sum of the volumetric liquid water content, θ, and the volumetric water vapor content, θ_v), h (m) is pressure head, K (m/s) is unsaturated soil hydraulic conductivity, K_{vh} (m/s) is isothermal vapor hydraulic conductivity, β is the angle between the flow direction and the vertical axis (equals 0° for vertical flow), K_{LT} (W/m/K) is thermal hydraulic conductivity of the liquid phase, K_{vT} (W/m/K) is thermal vapor hydraulic conductivity. The overall water flow in eq. (1) is given as the sum of isothermal liquid flow, isothermal vapor flow, gravitational liquid flow, thermal liquid flow, and thermal vapor flow. Since the thermal terms in eq. (1) are a function of temperature, the modified Richards equation is solved numerically with the heat transport equation (eq. 2) to account for temporal and spatial changes in water content as related to soil temperature. The governing equation for heat transport with water vapor diffusion is given by Saito et al. (2006)

$$C_p(\theta)\frac{\partial T}{\partial t} + L_0\frac{\partial \theta_V}{\partial t} = \frac{\partial}{\partial x}\left(\lambda(\theta)\frac{\partial T}{\partial x}\right) - C_w q\frac{\partial T}{\partial x} - C_v\frac{\partial q_v T}{\partial x} - L_0\frac{\partial q_v}{\partial x} \tag{2}$$

where C_p ($J/m^3/K$) is the volumetric heat capacity of soil; L_0 (J/m^3) is volumetric latent heat of vaporization of liquid water; q and q_v (m/s) are liquid water and water vapor flux densities, $\lambda(\theta)$ (W/m/K) is coefficient of the apparent thermal conductivity of the soil; C_w and C_v ($W/m^2/K$) are volumetric heat capacity of liquid and vapor.

The volumetric heat capacity of the soil is defined by DeVries (1963) as

$$C_p(\theta) = C_n\theta_n + C_O\theta_O + C_w\theta + C_a a_v \tag{3}$$

Table 3.1.

Summary of the parameters and instruments used for data collection

Variable	Sensor Model	Accuracy	Manufacturer
Ground Heat Flux, G_z (W/m^2)	HFT3 Soil Heat Flux Plate	Better than 5% of reading	REBS Inc., Seattle, WA
Soil Water Content, θ_z (m^3/m^3)	Steven Hydra Probe II	± 0.03 (m^3/m^3)	Stevens Water Monitoring System Inc. Portland, OR
Soil Temperature, T_z (°C)	Steven Hydra Probe II	± 0.6 Degrees Celsius (From -10^o C to 36^o C)	Stevens Water Monitoring System Inc. Portland, OR
Air Temperature, T_a (ºC)	HMP45C Temperature and Relative Humidity Sensor	0.8 ºC @ -40 ºC 0.6 ºC @ 60 ºC	Vaisala Company, Finland
Relative Humidity, *RH* (%)	HMP45C Temperature and Relative Humidity Sensor	± 2% RH (0 to 90% RH) ± 3% RH (90 to 100% RH)	Vaisala Company, Finland
Short Wave Radiation (R_s and R_s'), long wave radiation (R_l and R_l') (W/m^2)	NR01 Four-Component Net Radiation Sensor	± 10% for 12 hours totals, day and night	Hukseflux Thermal Sensors B.V., Delft, Netherlands
Wind Speed (m/s)	RM Young Wind Sentry Set	± 0.5 m/s	R. M. Young Company, Traverse City, MI
Rain (mm)	TE525 Tipping Bucket Rain Gauge	Up to 1 in/hr: ± 1% 1 to 2 in/hr: +0, -3% 2 to 3 in/hr: +0, -5%	Texas Electronics Inc. Huston, TX
Thermal conductivity (W/m/K), diffusivity (mm^2/s), and heat capacity (MJ/m^3/K)	KD2 Pro Thermal Properties Analyzer	±5 to ±10% Thermal Conductivity/Resistivity ±10% Specific Heat ±10% Thermal Diffusivity	Decagon Devices Inc. Pullman, WA

where C_n, C_o, C_w and C_a (J/m^3/K) are volumetric heat capacity of solid phase, organic matter, water and air, and θ_n, θ_o, θ are volumetric fraction of solid phase, organic matter,

and liquid phase. The volumetric heat capacity of air represents a small fraction of the total volumetric heat capacity of soil and was ignored by HYDRUS-1D. The organic matter constituent in the siliceous sinter was ignored as the deposit was formed at temperatures above 70 °C (Cady and Farmer, 1996). Therefore eq. (3) can be rewritten as

$$C_p = C_n(1-\varphi) + C_w\theta \tag{4}$$

where Φ (m^3/m^3) is porosity. On October 30th, 2014, soil core samples were taken at 9 cm and 13 cm depths to measure soil water content (θ) and porosity (φ). The average water content and porosity values were 0.15 ± 0.05 m^3/m^3 and 0.2 ± 0.05 m^3/m^3, respectively. Using eq. (4), the average fraction of the solid phase was estimated as 0.8 ± 0.05 m^3/m^3. The volumetric heat capacity of water vapor (C_v) was estimated by multiplying the specific heat capacity of water vapor (1996 J/kg/K) by the density of the water vapor (ρ_v) which is a function of soil temperature and the saturated vapor density as

$$\rho_v = \rho_{vs} H_r \tag{5}$$

$$\rho_{vs} = \frac{\exp\left(31.37 - \frac{6014.79}{T} - 7.92*10^{-3}T\right)}{10^3 T} \tag{6}$$

where T (K) is the soil temperature. The relative humidity (H_r) can be calculated from the pressure head, h (cm), using a thermodynamic relationship between liquid water and water vapor in soil pores as described by Philip and De Vries (1957)

$$H_r = \exp\left(\frac{hMg}{RT}\right) \tag{7}$$

where M is the molecular weight of water (0.018 kg/mol), g is the gravitational acceleration (9.81 m/s^2), and R is the universal gas constant (8.314 J/mole/K)

The liquid water and water vapor fluxes in the vertical profile are described as

$$q = -K\left(\frac{\partial h}{\partial x} - 1\right) - K_{lT}\frac{\partial T}{\partial x} \tag{8}$$

$$q_v = -K_{vh}\left(\frac{\partial h}{\partial x} + 1\right) - K_{vT}\frac{\partial T}{\partial x} \tag{9}$$

where K and K_{lT} (m/s) are isothermal water hydraulic conductivity and thermal water hydraulic conductivity, and K_{vh} and K_{vT} (m/s) are isothermal vapor hydraulic conductivity and thermal vapor hydraulic conductivity. The apparent thermal conductivity and thermal conductivity of the porous medium are defined as

$$\lambda(\theta) = \lambda_0(\theta) + \beta_t C_w |q| \tag{10}$$

$$\lambda_0(\theta) = b_1 + b_2\theta + b_3\theta^{0.5} \tag{11}$$

where β (m) is the thermal dispersivity, and b_1, b_2, and b_3 (W/m^3/K) are empirical parameters. The total heat transport equation is defined as the sum of the conduction of sensible heat as described by Fourier's law (first term in the right side), convection of sensible heat by liquid water and water vapor (second and third terms), and convection of latent heat by vapor flow (fourth term).

3.2.3.1. Initial Conditions

The initial conditions were provided by specifying the soil pressure head and soil temperature along the profile at time 0-minute. The initial condition for pressure head was not directly measured on site. Since the simulation started with a dry day, the initial pressure head in the profile was assumed to linearly decrease with depth to the depth of the water table at 1 m. The initial condition for temperature was determined by linearly

connecting the temperature estimated at 0 cm, temperature measured at 5 cm, and temperature estimated at 15 cm, at 0-minute of the simulation. Connecting these three temperature values revealed a linear increased in soil temperature with depth at the top 15 cm of the soil.

3.2.3.2. Boundary Conditions for Water Flow

The upper boundary condition for water flow in the experiment site in NGB was a system dependent boundary that was controlled by the atmospheric conditions, with a surface runoff characteristics. HYDRUS-1D specifying the boundary condition as a surface runoff as the model does not allow water to accumulate at the surface after precipitation. The boundary condition was obtained by limiting the absolute value of the flux by the following two conditions described in (Neuman et al., 1974) as

$$\left| -K\frac{\partial h}{\partial x} - K \right| \le E \qquad \text{at x = L} \tag{12}$$

$$h_A \le h \le h_S \qquad \text{at x = L} \tag{13}$$

where E (m/s) is the maximum potential rate of infiltration or evapotranspiration under the current atmospheric conditions, h (m) is the pressure head at the soil surface, and h_A and h_S (m) are minimum and maximum pressure heads allowed under the prevailing soil conditions. When one of the end points of eq. (12) and (13) is reached, a prescribed head boundary condition is used to calculate the actual surface flux. The bottom boundary condition for water flow was set as a variable pressure head to account for the effect of water table at approximately 1 m depth at bottom of the profile.

3.2.3.3. Boundary Conditions for Heat Transport

The upper and lower boundary conditions for heat transport were set as a time-dependent temperature boundary conditions. The temperature in the upper boundary represents the skin temperature of the ground surface estimated from the measured incoming longwave radiation (R_l) and estimated average surface emissivity (ε) using Stefan Boltzmann equation as

$$R_l = \varepsilon \sigma T_s^4 \tag{14}$$

where σ is Stefan-Boltzmann constant ($5.681*10^{-8}$ W/m^2/K^4), and T_s (K) is the ground skin temperature. The temperature in the lower boundary at 15 cm was estimated using the measured conductive heat flux at 10 cm (G_z) through the heat flux plate and soil temperature measured at 5 cm using Fourier law as follows

$$G_z = -\lambda \frac{\partial T}{\partial x} \tag{15}$$

where ∂T is the difference between the temperature measured at 5 cm and the temperature estimated at 15 cm, ∂x is the depth between the two points (i.e. 10 cm), λ is average thermal conductivity at 10 cm depth estimated as the average of the thermal conductivities measured at site at 9 cm and 13 cm using the KD2 thermal analyzer as explained before.

3.2.3.4. Soil Hydraulic Parameters

In this study van Genuchten-Mualem single porosity model was used to define soil hydraulic parameters *θ(h)* and *K(h)* (Van Genuchten, 1980). This model assumes that the 15 cm soil layer has single porosity charechteristics. Van Genuchten-Mualem model

is defined with water content and soil hydraulic conductivity models as

$$\theta(h) = \theta_r + \frac{\theta_s + \theta_r}{\left[1 + |\alpha h|^n\right]^m} \tag{16}$$

$$K(h) = K_S S_e^l \left[1 - \left(1 - S_e^{1/m}\right)^m\right]^2 \tag{17}$$

where θ_s (m^3/m^3) is saturated water content, θ_r (m^3/m^3) is residual water content; α, n, and m (m = 1/n+1), are empirical parameters; S_e is effective saturation; and K_s (m/s) is saturated hydraulic conductivity. The saturated water content and residual water content were determine from 5-minute measurements of water content at 5 cm as the maximum and minimum water contents as 0.3 m^3/m^3 and 0.13 m^3/m^3, respectively. HYDRUS-1D was used to optimize the parameters α, n, and K_s using the Levenberg-Marquardt function, which expresses the difference between the observed parameter and the predicted system response (Marquardt, 1963). The initial values for these parameters were selected according to the specifications for loam soil given in the model catalog as n = 3.6, α = 1.56 1/m and K_s = 2.89*10^{-6} m/s. However, these parameters do not necessarily represent the actual parameters of the soil in the study area. Because the range of thermal properties of the siliceous sinter is unknown, the maximum and minimum ranges for α, n, and K_s were set to cover the maximum values of sand soils and minimum values of silty clay soils. For sand soils, the values α, n, and K_s are given in Simunek et al. (2005b) as 14.5, 2.68, and 8.3*10-5 m/s, respectively, and for silty clay soil, these values are given as 0.5, 1.09, and 5.6*10-8 m/s, respectively.

3.2.3.5. Heat Transport Parameters

On 30 October 2014, we measured thermal conductivity (λ_0) on site at 9 cm and 13 cm depths using KD2 thermal analyzer probe. Soil samples were collected at the same depths to measure water content using the gravimetric method. The measured thermal conductivities and water contents were used in the thermal conductivity equation defined by Chung and Horton (1987) to estimate the parameters b_1, b_2, and b_3, as

$$\lambda_0(\theta) = b_1 + b_2\theta + b_3\theta^{0.5} \tag{18}$$

where b_1, b_2, and b_3 (W/m/K) are empirical parameters. Fig. (3.2) shows the fitting of the two measurement points relative to sand, clay, and peat soils, developed in Chung and Horton (1987).

3.3. Results and Discussion

3.3.1. Soil Hydraulic and Thermal Characteristics

The inverse solution in Hydrus-1D was performed by optimizing the hydraulic parameters n, α, and K_s. The model converged after 10 iterations with minimum objective function as 0.353 and n, α, and K_s optimized values as 6.44, 1.41, and $4.21*10^{-7}$ m/s, respectively. The standard error and lower and upper 95% confidence levels are presented in Table (3.3). The correlation coefficients between the estimated parameters shows strong linear correlation ($R^2 > 0.9$) (Table 3.3). Simunek et al. (2005a) explained that the correlation matrix shows the nonorthogonality between the estimated parameters and that the correlation matrix can be used to select the parameters to be kept constant in the model based on the high correlation. The soil water retention and unsaturated

hydraulic conductivity function for the siliceous sinter soil were developed from the optimized parameters as in Fig. (3.3).

The confidence limit on parameters estimates using HYDRUS 1-D were not well defined mainly because the theory used by the model to calculate the parameters are linear models. The results concluded that the parameters were accurately estimated given the narrow confidence level (Table 3.2) and high coefficient of correlation (Table 3.3). However, HYDRUS-1D estimates these as a combination of unknown parameters rather than an independent parameter. Statistically, many combinations of these parameters can result in the same objective function making estimates of an individual value of the parameter challenging given the data obtained for the study in this chapter.

3.3.2. Model Calibration

Model calibration is generally done by adjusting the input parameters and/or the initial or boundary conditions to closely match the simulated results and measured variables. The calibration was done for ten consecutive days in 2009 from September 23rd to October 2nd, to optimize the hydraulic parameters n, α, and K_s as explained in the method section. The model was then validated using two data sets from 2010 and 2011. The days from 23 to 29 September 2009 were mostly sunny with clear skies (Fig. 3.4). A total of 3.81 mm of rain was recorded on September 30th, 2009, resulted in increase in water content to about 0.3 m^3/m^3. Air and surface temperatures were notably lower during that day compared to the former dry days. The data used for the validation from 2010 was chosen from a period with notably high soil and ground surface temperatures, possibly related to increase in subsurface thermal heat flow. Surface

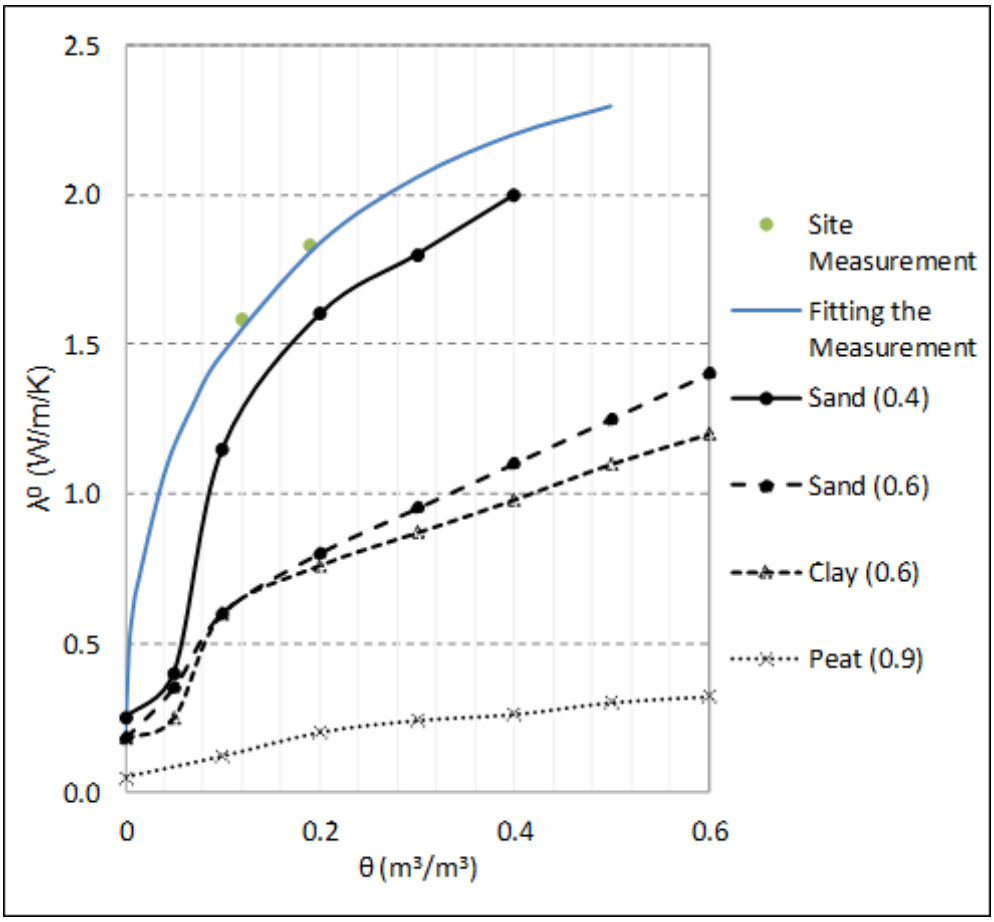

Fig. 3.2. Plot of thermal conductivity for different porous media (porosities shown in parenthesis) as a function of volumetric water content presented in Chug and Horton (1987). Measurements of thermal conductivity made at the research site from depths of 9 cm and 13 cm were used to fit the thermal conductivity model presented in Eq. (18) to the data points.

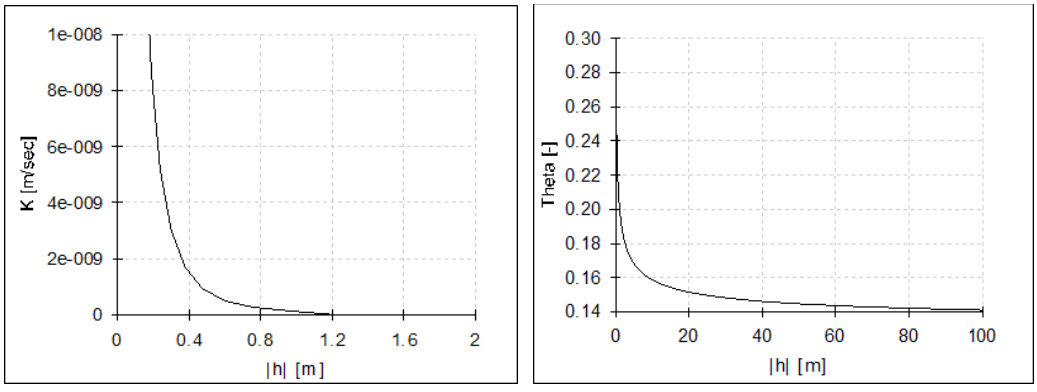

Fig. 3.3. Plot of soil retention curve and unsaturated hydraulic conductivity function.

Table 3.2.

The standard error and lower and upper 95% confidence level of the optimized hydraulic parameters α, n, and K_s

Variable	Value	Standard Error	Lower 95% Confidence Limit	Upper 95% Confidence Limit
α	6.44	0.32	5.82	7.06
n	1.41	0.01	1.39	1.44
K_s (m/s)	$4.21*10^{-7}$	$0.27*10^{-7}$	$3.67*10^{-7}$	$4.74*10^{-7}$

Table 3.3.

The correlation coefficient (R^2) between each two estimated parameters

Variables	α and n	α and K_s	n and K_s
R^2	-0.9947	0.9854	-0.9841

temperature during that period was about 10 °C higher than the calibration days of 2009. Soil and surface temperatures during the validation days from 13-22 September 2011 were generally similar to 2009. About 0.5 mm of rain was recorder during September 14th, 2011, and another 2.85 mm was recorded during September 16th, 2011. Maximum water content measured at 5 cm on September 16th, 2011 was approximately 0.28 m^3/m^3.

The results of model calibration show the 5-minute measurements of soil temperature and water content at 5 cm and the simulated soil temperatures and water contents at 0 cm, 5 cm, and 10 cm (Fig. 3.5). In the dry and mostly sunny days from 23 to 29 September 2009, the estimated soil temperature was about 5 °C warmer than measurement at 5 cm in the maximum and minimum ends. That difference increased to about 7 °C from September 30th to October 2nd. The simulated water content was generally consistent during the dry days when average measured water content at 5 cm

was about 0.21 ± 0.04 m^3/m^3. As water content increased during September 30th, the simulated water content was lower than the measurement with a time lag between the two of about 3 hours.

The validation results for modeled and measured soil temperate at 5 cm was mostly consistent with about 5° C bias. The consistent temperature bias suggested that either the model simulation is biased or the temperature probe may have been dislocated to a shallower depth, most likely due to natural processes in the soil. Temperature probes are prone to dislocation during installation and/or soil shrink/swell after rain. The regression analysis had high R^2 values for modeled and measured soil temperature at 5 cm in the calibration and validation days (Fig. 3.8.a to Fig. 3.8.c). Modeled and measured water content was less accurate compared to soil temperature with lower R^2 values; however, was consistent (Fig. 3.8.d to Fig. 3.8.f).

3.3.3. Comparison of Two Conductive Heat Flux Simulations

Estimation of the conductive heat flux at the surface was one of the objectives of this study to evaluate the calorimetric heat storage method used in Chapter 2 to estimate the ground heat flux at the surface. In that study, the conductive heat flux at the surface was estimated, using the same data used in this study, by adding the soil heat flux measurement at 10 cm to the estimated soil heat storage above the heat flux plate. Some assumptions were made to apply that method including that the temperature measured at the mid-depth between the heat flux plate and the ground surface (5 cm) was representative of the average temperature of the 10-cm soil layer. This assumption was denied by several studies including Massman (1993) who expected that the error in

estimating the heat storage due to using one-depth temperature measurement is about 3-10% .

HYDRUS-1D estimates the temperature and water content profiles by numerically solving the modified Richards equation for water flow and the heat transport equation. In this study, to estimate the conductive heat flux at the surface, the temperature gradient between the surface and 0.1 cm depth (top node in the soil profile) was multiplied by the average thermal conductivity of that node using Fourier law (eq. 15). Fig. (3.9) shows the 6-hours conductive heat flux estimated at the ground surface from HYDRUS-1D temperature simulation from 23 September to 2 October 2009, and the 5-minute conductive heat flux at the surface estimated in Chapter 2. The simulation agreed well with the average conductive heat flux estimated from the heat storage method. The noise of the estimated soil surface heat flux using the calorimetric method was notably high especially at sunrise and sun set when soil temperature changed rapidly.

3.3.4. Liquid Water Flux and Water Vapor Flux

The modeled liquid water flux and water vapor flux were used to estimate the convective heat flux of liquid water and water vapor and latent heat flux of water vapor using the heat transport equation (eq. 2). Fig. (3.10) shows the vertical liquid water flux and water vapor flux estimated at 12 am and 12 pm on 23 September to 2 October, 2009. The sign of the liquid water flux and water vapor flux determines the direction of the flux in the profile (i.e. negative indicates downward flux and positive indicates upward flux). During the dry days between 23 and 29 September, 2009, the liquid water flux through the profile was approaching 0 mm/day at 12 am. On October 1st, the liquid water flux

after the precipitation on September 30th was approximately -4 mm/day at the bottom of the profile and decreased to -2 mm/day at 12 am on October 2nd (Fig. 3.10.a). At noon on September 30th, the liquid water flux was approximately -25 mm/day at 2 cm depth following the rain, and was 0 mm/day at approximately 11 cm depth. At noon on October 1st, the maximum liquid water flux was approximately -6 mm/day at 3 cm depth and was almost constant below 8 cm depth. On October 2nd the liquid water flux was +6

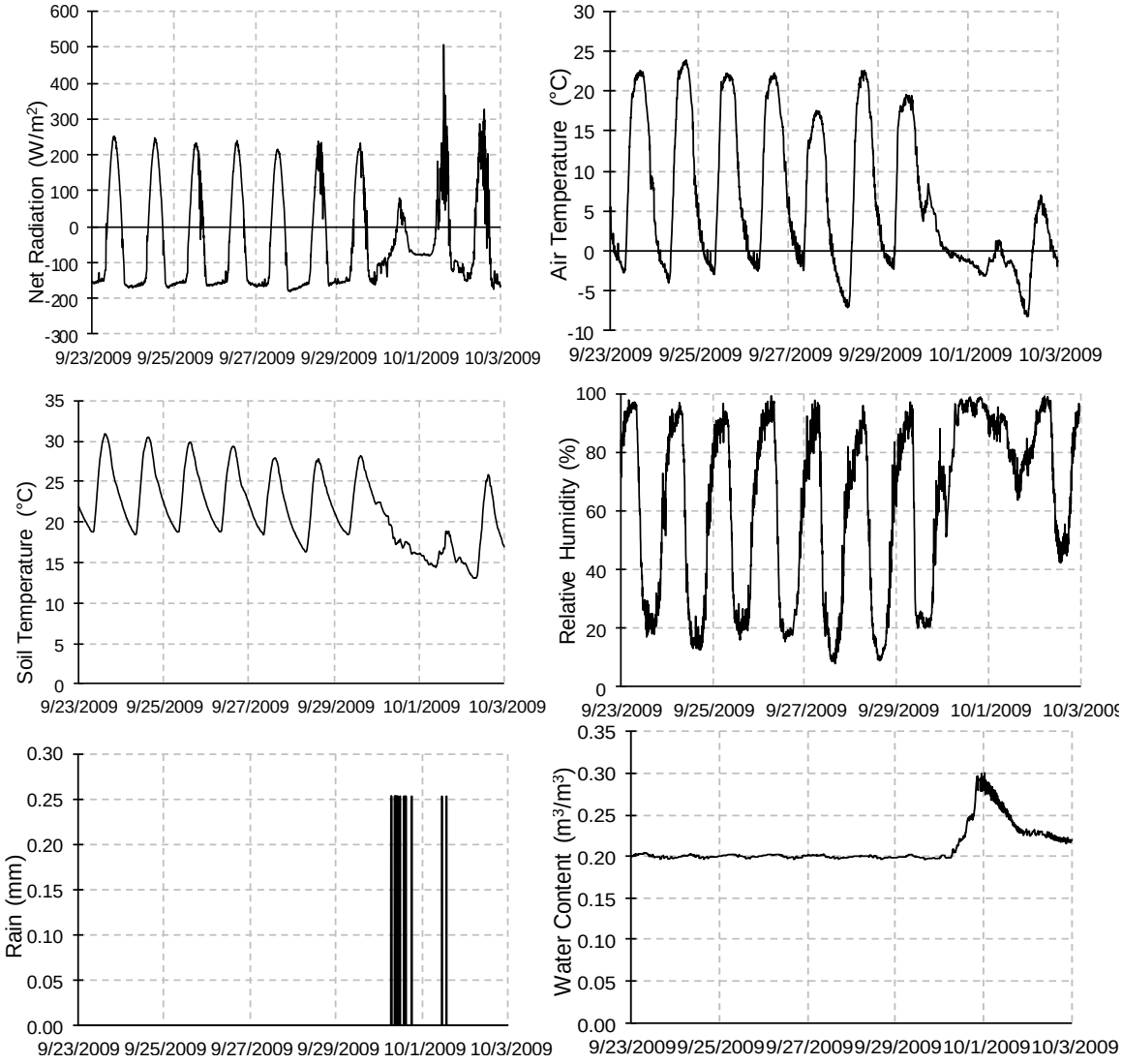

Fig. 3.4. The 5-minute measurement of weather and soil water content data for 23 September to 2 October, 2009.

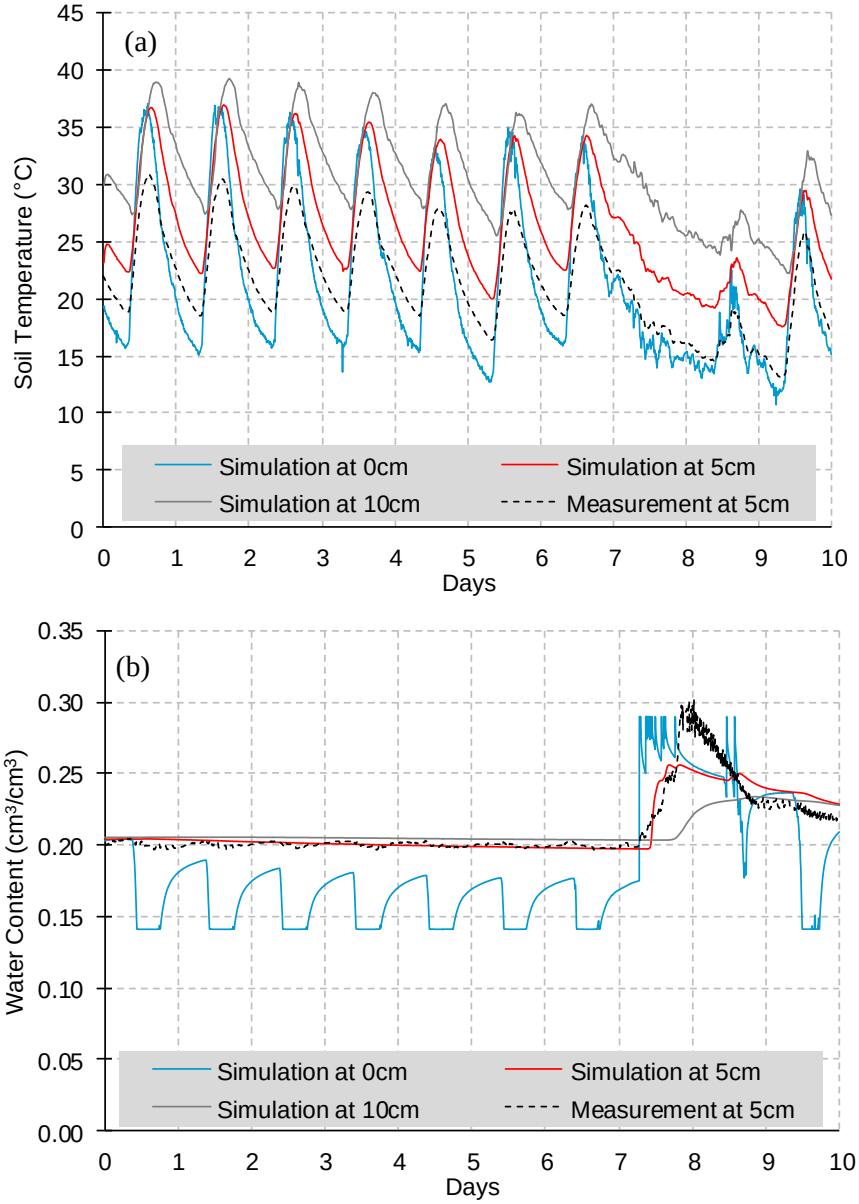

Fig. 3.5. Model calibration results showing (a) soil temperature measured at 5 cm and simulation of soil temperature at 0 cm, 5 cm, and 10 cm, (b) water content measured at 5 cm and simulation of water content at 0 cm, 5 cm, and 10 cm, from 23 September to 2 October, 2009.

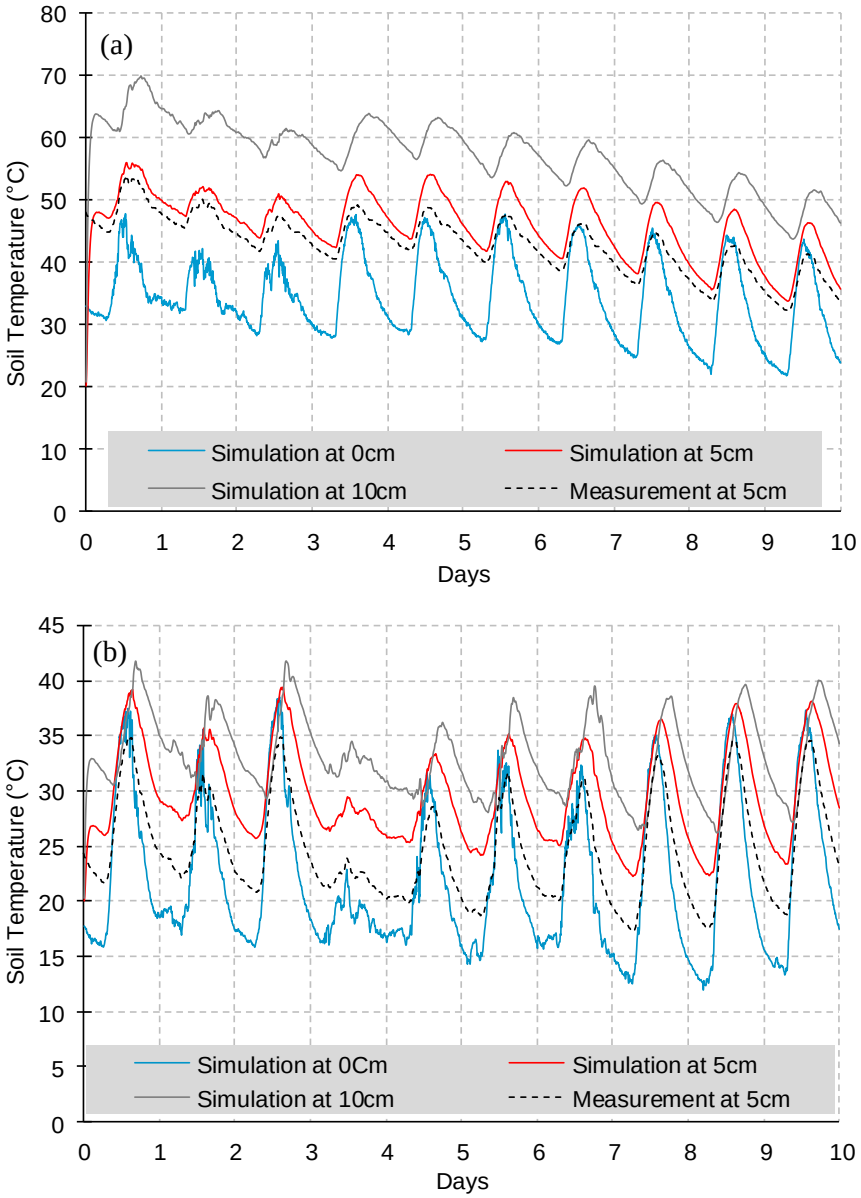

Fig. 3.6. Model validation results showing the measured soil temperature at 5 cm and simulated soil temperatures at 0 cm, 5 cm, and 10 cm, from (a) 22-30 September 2010, and (b) 13-22 September 2011.

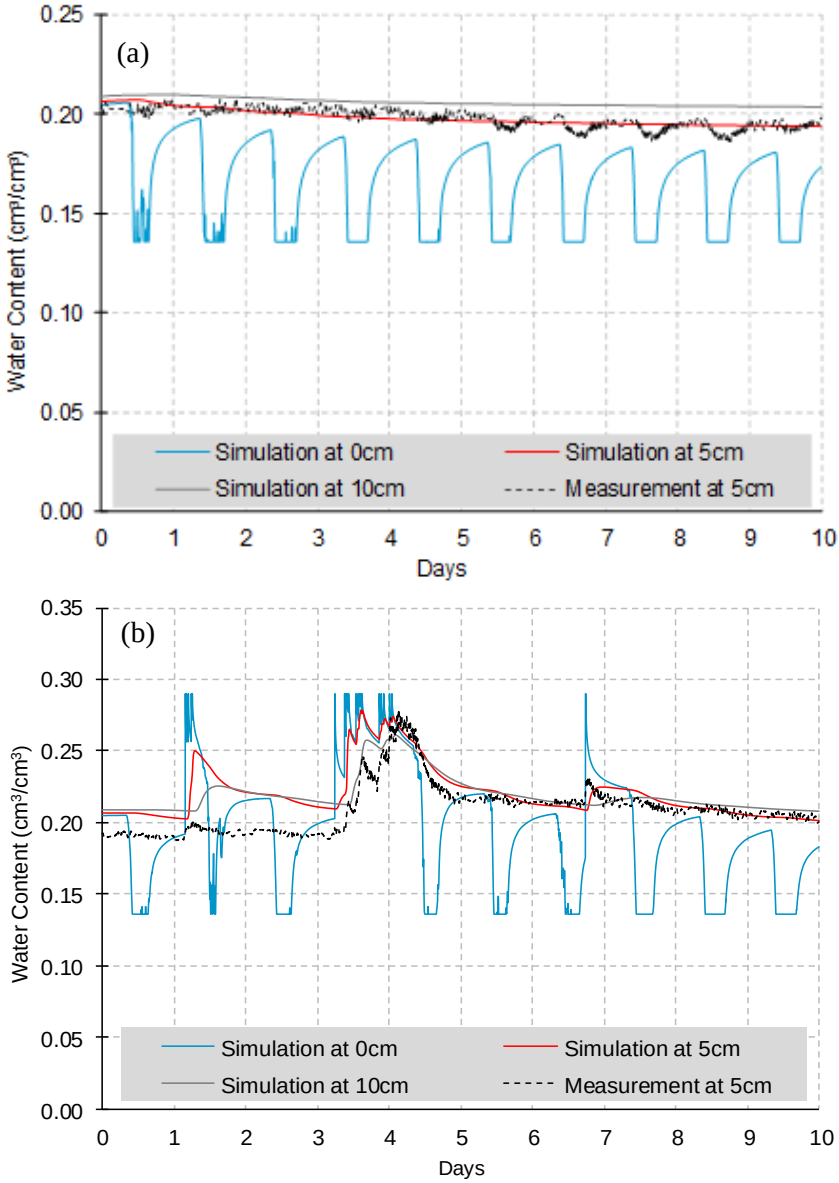

Fig. 3.7. Model validation results show the measured water content at 5 cm and simulated water content at 0 cm, 5 cm, and 10 cm, from (a) 22-30 September 2010, and (b) 13-22 September 2011.

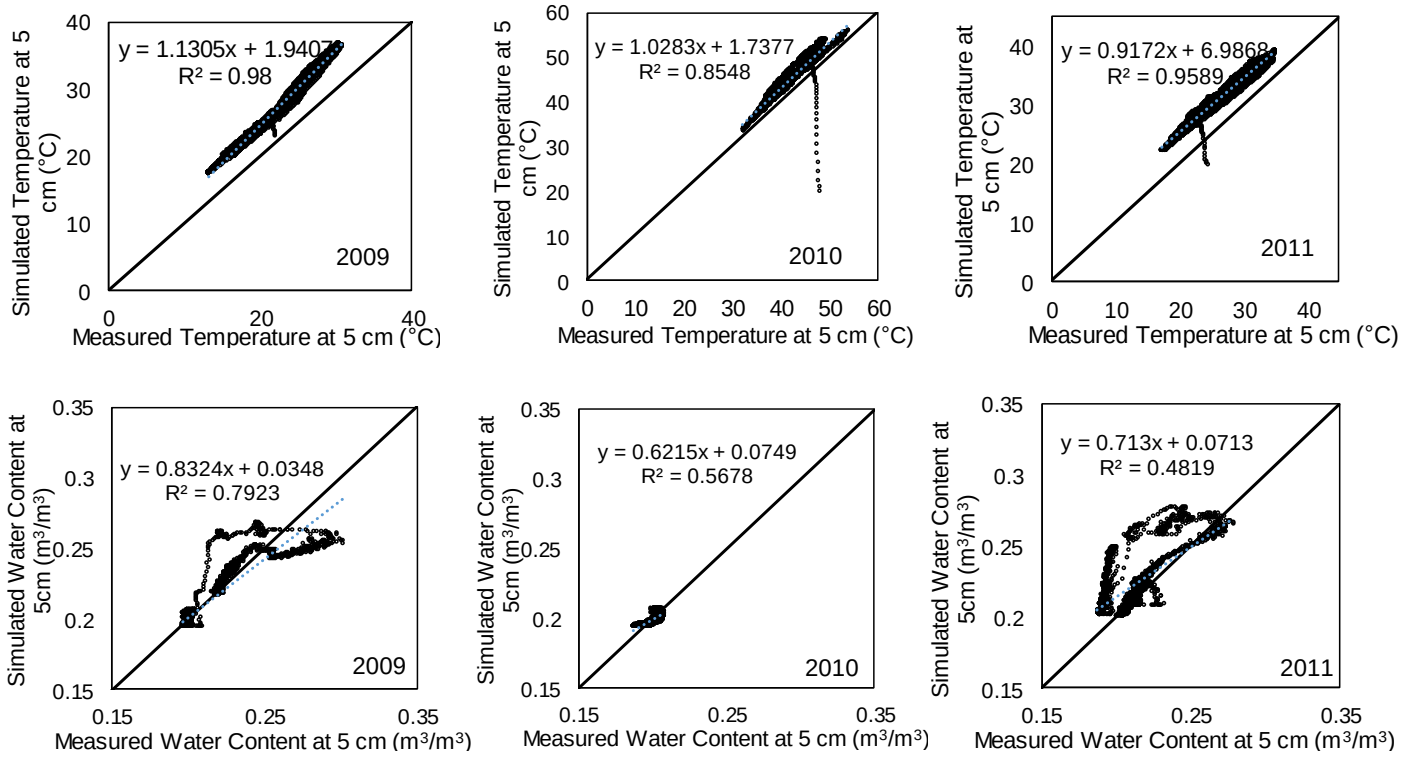

Fig. 3.8. Regression plots for 5-minute measured soil temperature at 5 cm (top) and simulated water content at 0 cm, 5 cm, and 10 cm, from (a) 22-30 September 2010, and (b) 13-22 September 2011.

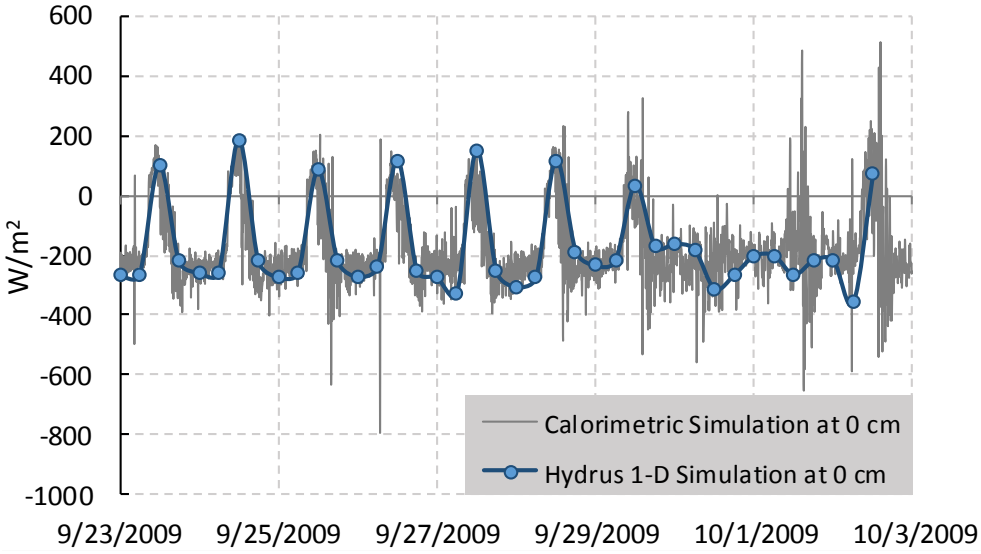

Fig. 3.9. 5-minute conductive heat flux estimated in Chapter 2 and the 6-hours conductive heat flux estimated using HYDRUS-1D simulation.

mm/day at the top of the profile, as water moved upwards due to increase evaporation. At 12 am, water vapor flux was always positive flowing upwards in the soil profile. On 23-29 September 2009, the water vapor flux increased exponentially at approximately 6 cm to reach maximum values just few millimeters below the surface (Fig. 3.10.e). The water vapor flux decreased few millimeters below the surface due to the effect of the diffuse cool air through the surface. At 12 am on October 1st, the water vapor flux was approaching 0 mm/day in the top of the profile as water content increased after the precipitation on September 30th. At 12 pm, the water vapor flux was negative above a certain depth and then became positive towards the bottom of the profile. For example, on September 24th the water flux was positive above approximately 11 cm reaching a maximum value of 0.103 mm/day at the surface. The water vapor flux decreased below 11 cm to a minimum value of 0.013 mm/day at 15 cm. On September 30th and October

1st, the water vapor flux was very close to 0 mm/day above approximately 7 cm and was positive below that depth.

Fig. (3.11) shows the 6-hourly time series of the liquid water flux and water vapor flux at the specified nodes in the soil profile at 0 cm (surface), 5 cm, 10 cm, and 15 cm, estimated at 12 am, 6 am, 12 pm, and 6 pm, on 23 September to 2 October 2009. The liquid water flux at 0 cm was always positive at noon and was close to 0 mm/day at 6 am, 6 pm and 12 am (Fig. 3.11.a). During the dry days of 23-29 September, the liquid water flux at the 5 cm, 10 cm, and 15 cm, was close to 0 mm/day. The effect of rain on the liquid water flux can be seen on September 30th and October 1st. The maximum liquid water flux at 5 cm, at noon, on September 30th, was about -12 mm/day, and decreased to -5 mm/day at the same time on October 1st. The liquid water fluxes at 10 cm and 15 cm were higher during the later days compared to the precedent dry days.

During the dry days, the water vapor flux at 0 cm was negative at noon as the surface was warmed up by the sun, and was positive at 6 pm, 12 am, and 6 am (Fig. 3.11.b). The water vapor flux at 5 cm was notably lower than the surface vapor flux and was flowing downward the soil profile at noon during the dry days. On September 30th and October 1st, the water vapor flux was about 0 mm/day at 0 cm, 5 cm, and 10 cm due to increase soil water content. The water vapor flux at 15 cm was generally greater than that estimated at 5 cm and 10 cm and was mainly flowing upwards the profile.

3.3.5. Convective Heat Flux and Latent Heat Flux

The convective heat flux of the liquid water and the convective heat flux of water vapor through the specified nodes of the soil profile were calculated using the second and

third terms of the heat transport equation as $\left[C_W\, q\, \frac{\partial T}{\partial x}\right]$ and $\left[C_v\, q_v\, \frac{\partial T}{\partial x}\right]$, respectively. Fig. (3.12) shows the time series of these two fluxes estimated at 0 cm (surface), 5 cm, 10 cm, and 15 cm, using the liquid water flux and vapor flux densities in Fig. (3.11). The convective heat flux by liquid water was generally low (close to 0 W/m^2) in the four nodes during the dry days of 23-29 September, 2009. On September 30th and October 1st, the heat flux increased with the maximum value occurred at 5 cm on September 30th at noon and was approximately 0.1 W/m^2. Maximum value at 10 cm on the same day was about 0.05 W/m^2 and occurred at 6 pm.

The convective heat flux by water vapor was more than nine orders of magnitude less that that by liquid water. The maximum value occurred at the surface on September 26th at noon and was about 1.1*10^{-8} W/m^2. At 5 cm and 10 cm, the heat flux increased during the evening and night and was minimum at 12 pm approaching 0 W/m^2.

The latent heat of water vapor was calculated using the third term of the heat transport equation as $\left[L_0\, \frac{\partial q_v}{\partial x}\right]$. At the surface on 23- 29 September, the latent heat was mostly flowing downward in the profile at noon and upwards to the surface at 6 pm following the direction of the water vapor flux. The range of the latent heat in the surface varied according to the water vapor gradient. The maximum value at noon and 6 pm occurred on September 24th as -0.38 W/m^2 and 0.5 W/m^2. The latent heat flux in the nodes at 5 cm, 10 cm, and 15 cm was notably lower compared to the surface, due to low vapor flux gradient, with a range varied between -0.5 W/m^2 and 0.5 W/m^2. During September 30th and October 1st, the latent heat flux was close to 0 W/m^2 as the water vapor flux approached 0 mm/day during these days.

3.3.6. Comparison of the Different Rates of Heat Transport

The contribution of the heat transport mechanisms in the total heat flux in the surface of bare ground area in NGB are presented in Fig. (3.14). Generally, the convective heat flux and latent heat flux were orders of magnitude lower than the conductive heat flux. The conductive heat flux contributed to more than 99% of the total heat flux in the study area. During the dry days of 23-29 September 2009, the contribution of the conductive heat flux varied diurnally with a percentage close to 100% at 12 am and 6 am and lower percentages at 12 pm and 6 pm. On September 30th and October 1st, the conductive heat flux contributed to about 100% of total heat flux throughout the entire day. The contribution of the latent heat flux contravened the contribution of the conductive heat flux, with values close to 0% at 12 am and 6 am, and maximum values at 12 pm and 6 pm. The contribution of the convective heat flux of liquid water and water vapor was less than 0.05% of the total heat flux.

3.4. Summary and Conclusions

Studies about heat transport mechanisms and rates in the subsurface of geothermally heated grounds in Yellowstone National Park are limited. In Chapter 2, it was assumed that the ground heat flux at and near the surface, in geothermally heated grounds, is mainly a combination of near-surface geothermal heat flux and the heat flux from absorbed solar shortwave radiation and atmospheric longwave radiation, neglecting the effect of latent heat flux and sensible heat flux due to increased ground temperatures.

This study was conducted to test that hypothesis by estimating the rates of heat transport on an near the ground surface through different mechanisms including

conduction of convection of latent heat by water vapor in the top 15 cm of siliceous sinter deposit in Norris Geyser Basin. HYDRUS-1D was used to estimate the rates of heat

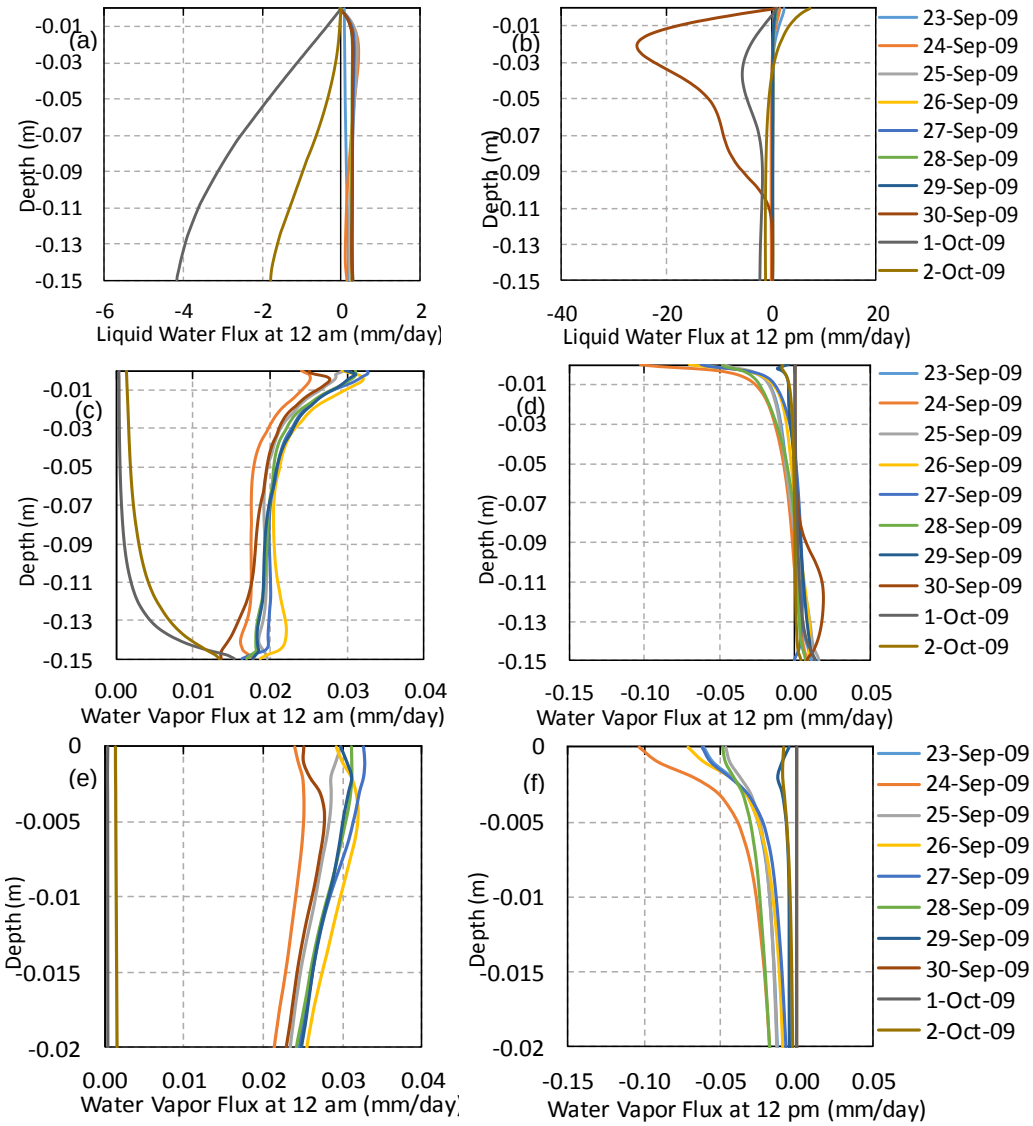

Fig. 3.10. Vertical profiles of (a) liquid water flux (mm/day) at 12 am, (b) liquid water flux (mm/day) at 12 pm, (c) water vapor flux (mm/day) at 12 am, (d) water vapor flux (mm/day) at 12 pm.

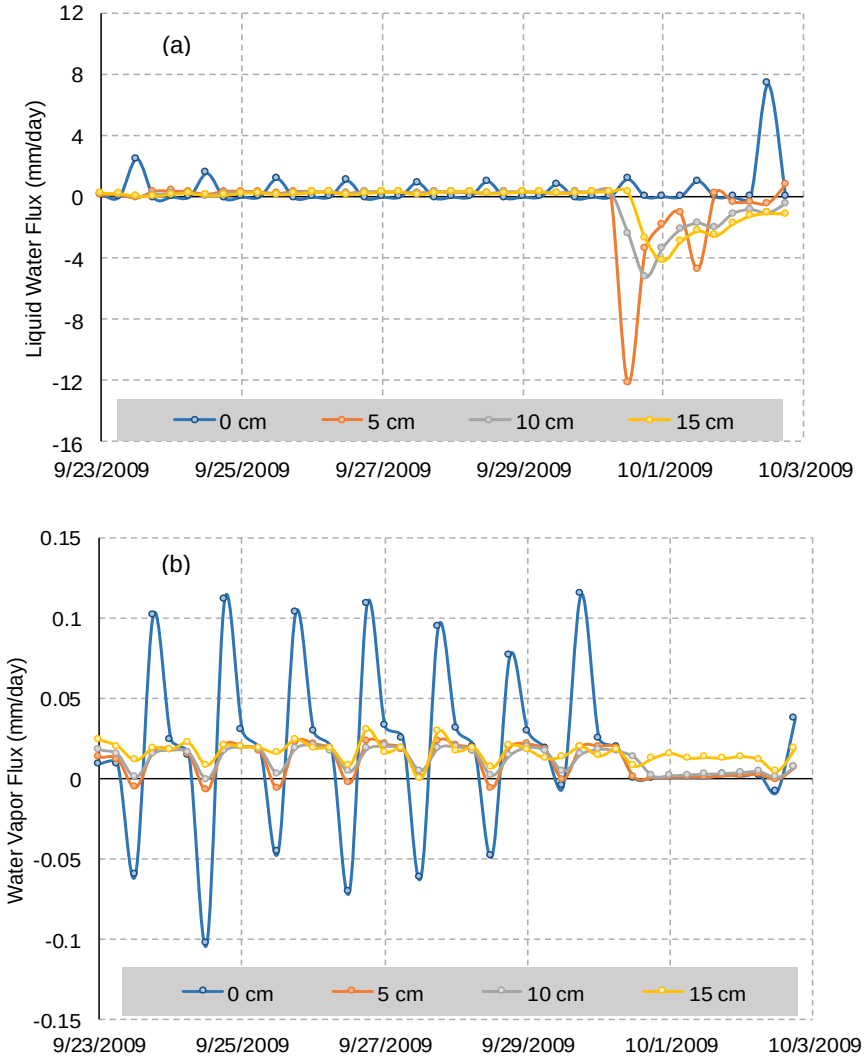

Fig. 3.11. (a) Liquid water flux, and (b) water vapor flux, modeled at the surface (0 cm) at 12 am, 6 am, 12 pm, and 6 pm for days from 23 September 2009 to 2 October 2009.

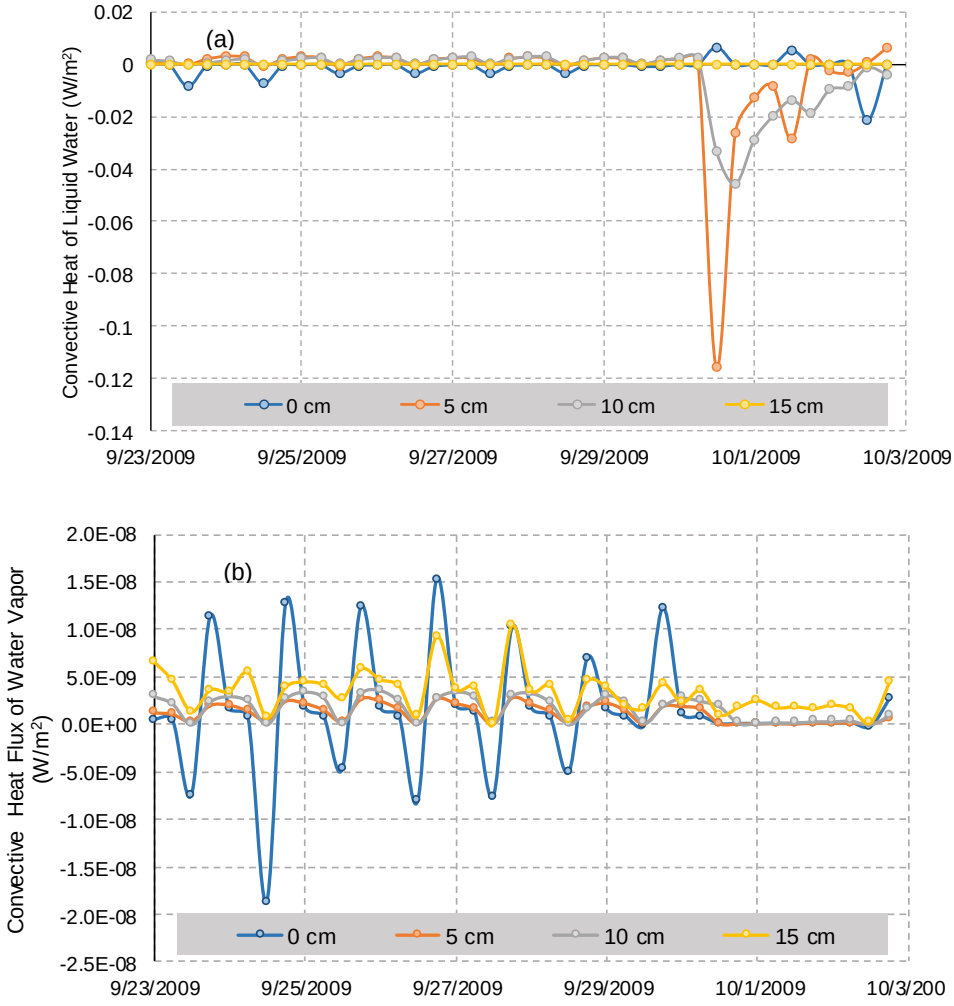

Fig. 3.12. Convection heat flux of (a) liquid water, and (b) water vapor, modeled at the surface (0 cm), 5 cm, 10 cm, and 15 cm, at 12 am, 6 am, 12 pm, and 6 pm for days from 23 September 2009 to 2 October 2009.

transport using estimated values of soil temperature, water content, liquid water flux, and water vapor flux, estimated along the soil profile. Modeling the heat transport rate in the siliceous sinter deposit required optimization solution to estimate the hydraulic and thermal properties for that deposit. The results of parameters optimization suggested acceptable parameterization and high correlation between the estimated parameters. Model calibration was carried out, using data from 10 days in September and October of 2009, to optimize the soil hydraulic parameters α, n, and Ks, for different water content conditions. The model was validated using water content and soil temperature measurements from September 2010 and September 2011. The simulated temperature at 5 cm showed consistent offset error of about 5° C.

The flux of liquid water was generally greater than that of water vapor after precipitation flowing mostly downwards in the soil profile. The flux of water vapor; however, was greater during dry days and either flowed upward or downward in the profile depending on the time of the day. The results of the heat transport rates showed that the conductive heat flux dominated the area with more than 99 % contribution to the total heat flux. The convective heat flux; however, represented only a small percent of the total heat flux. The latent heat of water vapor was about an order of magnitude greater than the convective heat flux of liquid water; however; represented less than 0.5% of the total heat flux. These results support the hypothesis that was suggested in chapter 2 that the latent heat flux and advective heat flux were negligible in the study site in Norris compared to conductive heat flux resulted from the stored solar radiation and atmospheric longwave radiation and the geothermal heat flux.

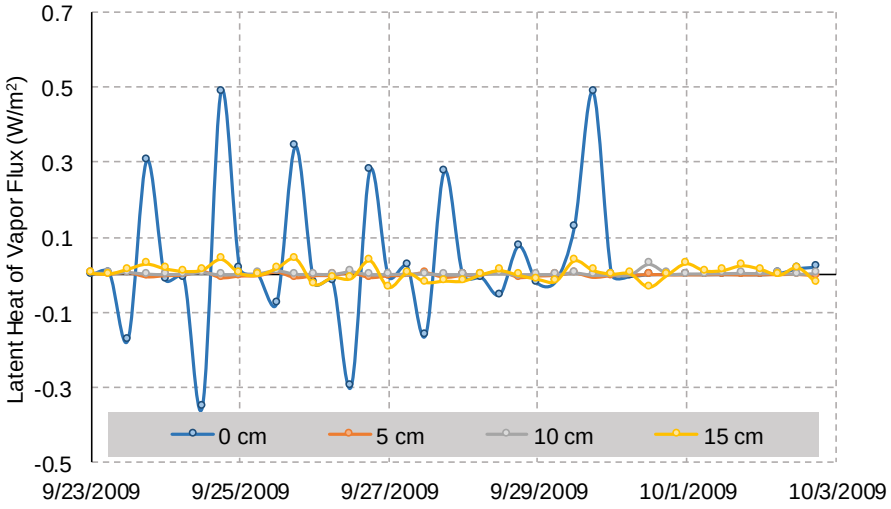

Fig. 3.13. Latent heat of water vapor, modeled at the surface (0 cm) at 12 am, 6 am, 12 pm, and 6 pm for days from 23 September 2009 to 2 October 2009.

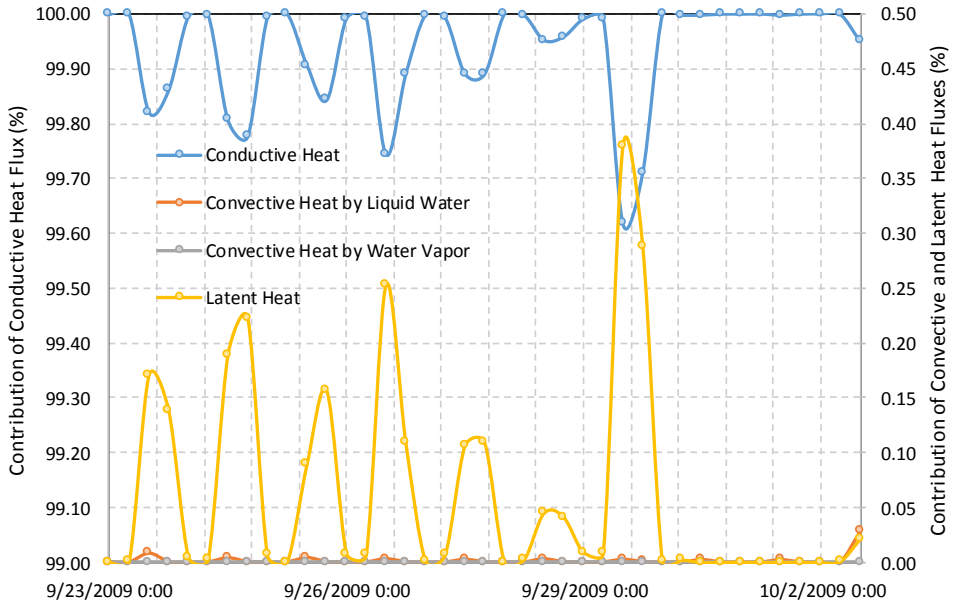

Fig. 3.14. Percent contribution of the conductive heat flux, convective heat flux by liquid water, convective heat flux by water vapor, and latent heat flux, to the total heat flux.

References

Abrams, M., 2000. The Advanced Spaceborne Thermal Emission and Reflection Radiometer (ASTER): data products for the high spatial resolution imager on NASA's Terra platform. International Journal of remote sensing, 21(5), 847-859.

Ball, J. W., McCleskey, R. B., Nordstrom, D. K., Holloway, J. M., Verplanck, P. L., Sturtevant, S. A., 2002. Water-chemistry data for selected springs, geysers, and streams in Yellowstone National Park, Wyoming, 1999-2000.

Cady, S. L., Farmer, J. D., 1996. Fossilizationprocessesin siliceous thermal springs: trends inpreservation along thermal gradients.

Campbell, K. A., Guido, D. M., Gautret, P., Foucher, F., Ramboz, C., Westall, F., 2015. Geyserite in hot-spring siliceous sinter: Window on Earth's hottest terrestrial (paleo) environment and its extreme life. Earth-Science Reviews, 148, 44-64.

Chung, S. O., Horton, R., 1987. Soil heat and water flow with a partial surface mulch. Water Resources Research, 23(12), 2175-2186.

De Vries, D. A., 1958. Simultaneous transfer of heat and moisture in porous media. Eos, Transactions American Geophysical Union, 39(5), 909-916.

DeVries, D. A., 1963. Thermal properties of soils. In 'Physics of plant environment'.(Ed. WR van Wijk) pp. 210–235: John Wiley & Sons: New York, NY.

Fournier, R. O., White, D. E., Truesdell, A. H., 1976. Convective heat flow in Yellowstone National Park.

Friedman, I., Norton, D. R., 2007. Is Yellowstone Losing Its Steam?—Chloride Flux out of Yellowstone National Park.

Haselwimmer, C. E., Prakash, A., Holdmann, G., 2011. Geothermal exploration at Pilgrim Hot Springs, Alaska using airborne thermal infrared remote sensing.

Hopmans, J. W., Šimunek, J., Bristow, K. L., 2002. Indirect estimation of soil thermal properties and water flux using heat pulse probe measurements: Geometry and dispersion effects. Water Resources Research, 38(1).

Hurwitz, S., Harris, R. N., Werner, C. A., Murphy, F., 2012. Heat flow in vapor dominated areas of the Yellowstone Plateau Volcanic Field: Implications for the thermal budget of the Yellowstone Caldera. Journal of Geophysical Research: Solid Earth (1978–2012), 117(B10).

Kool, J. B., Parker, J. C., Van Genuchten, M. T., 1985. Determining soil hydraulic properties from one-step outflow experiments by parameter estimation: I. Theory and numerical studies. Soil Science Society of America Journal, 49(6), 1348-1354.

Livo, K. E., Kruse, F. A., Clark, R. N., Kokaly, R. F., Shanks Iii, W. C., 2007. Hydrothermally altered rock and hot-spring deposits at Yellowstone National Park—characterized using airborne visible-and infrared-spectroscopy data.

Marquardt, D. W., 1963. An algorithm for least-squares estimation of nonlinear parameters. Journal of the society for Industrial and Applied Mathematics, 11(2), 431-441.

Massman, W. J., 1993. Errors associated with the combination method for estimating soil heat flux. Soil Science Society of America Journal, 57(5), 1198-1202.

Neale, C. M., Sivarajan, S., Masih, A., Jaworowski, C., Heasler, H., 2011. Estimating heat flow of thermal features in Yellowstone National Park using airborne thermal infrared remote sensing.

Neuman, S. P., Feddes, R. A., Bresler, E., 1974. Finite element simulation of flow in saturated-unsaturated soils considering water uptake by plants.

Philip, J. R., De Vries, D. A., 1957. Moisture movement in porous materials under temperature gradients. Eos, Transactions American Geophysical Union, 38(2), 222-232.

Saito, H., Šimůnek, J., Mohanty, B. P., 2006. Numerical analysis of coupled water, vapor, and heat transport in the vadose zone. Vadose Zone Journal, 5(2), 784-800.

Schelle, H., Iden, S. C., Fank, J., Durner, W., 2012. Inverse modeling of water flow and root water uptake in lysimeters. Vadose Zone J.

Simunek, J., Van Genuchten, M. T., 1999. Using the HYDRUS-1D and HYDRUS-2D codes for estimating unsaturated soil hydraulic and solute transport parameters. Characterization and measurement of the hydraulic properties of unsaturated porous media, 1523-1536.

Šimůnek, J., van Genuchten, M. T., 2008. Modeling nonequilibrium flow and transport processes using HYDRUS. Vadose Zone Journal, 7(2), 782-797.

Simunek, J., Van Genuchten, M. T., Sejna, M., 2005a. The HYDRUS-1D software package for simulating the movement of water, heat, and multiple solutes in variably saturated media, version 3.0, HYDRUS software series 1. Department of

Environmental Sciences, University of California Riverside, Riverside Edition.

Simunek, J., Van Genuchten, M. T.,Sejna, M., 2005b. The HYDRUS-1D software package for simulating the one-dimensional movement of water, heat, and multiple solutes in variably-saturated media. University of California-Riverside Research Reports, 3, 1-240.

Šimunek, J., van Genuchten, M. T., Senja, M., 1998. The HYDRUS-1D software package, code for simulating the one-dimensional movement of water, heat and multiple solutes in variably saturated porous media, version 2.01: IGWMC-TPS-53, Int. Ground Water Modeling Cent., Golden, Colo. School of Mines, Golden, USA.

Van Genuchten, M. T., 1980. A closed-form equation for predicting the hydraulic conductivity of unsaturated soils. Soil Science Society of America Journal, 44(5), 892-898.

White, D. E., Hutchinson, R. A., Keith, T. E. C., 1988. Geology and remarkable thermal activity of Norris Geyser Basin, Yellowstone National Park, Wyoming. US Geol. Surv., Prof. Pap.;(United States), 75(1456).

Wildenschild, D., Hopmans, J. W., Simunek, J., 2001. Flow rate dependence of soil hydraulic characteristics. Soil Science Society of America Journal, 65(1), 35-48.

CHAPTER 4

MONITORING SPATIAL AND TEMPORAL CHANGES IN HYDROTHERMAL FEATURES AT NORRIS GEYSER BASIN

Abstract

Continuous monitoring of the dynamic thermal activity in Yellowstone National Park is required and funded by the United States Congress. This study is part of the monitoring program initiated in the early 2000s to monitor changes over Yellowstone National Park's thermal activity. In this study, high-spatial-resolution thermal infrared imagery acquired through airborne remote sensing setup, were used to estimate year-to-year changes in radiant temperature, radiant flux, and radiant power over Norris Geyser Basin. A method was developed to remove the residual heat flux resulting from stored solar shortwave radiation in the ground, from the total radiant flux images enabling year-to-year comparison of changes due to mainly the geothermal heat source. The results showed that year-to-year monitoring of Norris Geyser Basin could depict changes in the radiant temperature and radiant flux before they were visually observed by the park service personnel. The repeated high-spatial-resolution monitoring may help resolve the concerns about public and property safety and the safety of the park service personnel and researchers, who come into a close contact with the hydrothermal areas in the park.

4.1. Introduction

4.1.1. History of Norris Geyser Basin and Previous Remote Sensing Studies

Norris Geyser Basin (NGB) of Yellowstone National Park (YNP) is known as the

most unrest thermal area in the park (Fournier et al., 2002; White et al., 1988). The highest temperatures in the park were recorded in the geysers of NGB that are distributed around Back Basin, Porcelain Basin, Ragged Hill, and Hundred Springs Plain (Fig. 4.1). NGB is also known for the frequent hydrothermal disturbances that involve relatively rapid changes in water and surface temperatures, renewed thermal activity of dormant features, and development of new features. Changes in the extent and/or temperatures of the hydrothermal features in the basin may indicate signs of change in the underlying magmatic system (Heasler et al., 2009). Therefore, geospatial data describing the temperature and other thermal characteristics of the hydrothermal features and the surrounding heated ground, is frequently needed to maintain public safety, design and relocate infrastructure facilities and install safety signs. Such data could eventually be integrated into Yellowstone's baseline information system and incorporated in the research program at YNP.

Geothermal heat flux (W/m^2) represents the heat coming from below the surface without accumulated heat from convection of warm air and/or conduction of solar energy in the soil. It can be measured directly from bore holes using thermocouples (Hurwitz et al., 2012b) or indirectly estimated from thermal chloride flux (Fournier et al. (1976); Friedman and Norton (2007)). Most of the active thermal areas in YNP are inaccessible either due to the extremely high kinetic temperatures or acidic nature or both. Remote sensing of hydrothermal features is being used to monitor spatial and temporal changes of radiant flux within and between geyser basins (Haselwimmer et al., 2011; Neale et al., 2011; Neale et al., 2016; Savage et al., 2010; Vaughan et al., 2012; Watson et al., 2008).

In the early 2000's, YNP implemented a scientific geothermal monitoring program that involved using remote sensing imagery to monitor geothermal features in the park following a noticeable deployment within NGB. The deployment included formation of new mud pots, changes in geyser eruptions, and significant increase in ground temperatures (Heasler et al., 2009). The remote sensing portion of the monitoring program included acquisition of repeated airborne thermal infrared (TIR) imagery of dynamic hydrothermal areas in the park, including NGB. The hottest hydrothermal features in NGB are typically a few square meters large which encouraged the use of high-resolution airborne remote sensing imagery.

The first airborne remote sensing study in NGB was initiated by the University of Montana-Missoula in 2002 (Hardy, 2005; Seielstad and Queen, 2009). Hardy (2005) acquired two sets of airborne remote sensing imagery in NGB using a single channel thermal sensor. His work represents the initiation of airborne remote sensing monitoring in YNP and provide a baseline for additional research using multi-sensor platform. His method demonstrated that a geothermal anomaly could be classified and mapped using high-spatial-resolution TIR imagery. Seielstad and Queen (2009) adopted Hardy's method and experimented the use of multi-channel imaging system. In our study we utilized the best of Hardy and Seielstad and Queen's technical advances and addressed some of the technical gaps. For example Hardy (2005) ignored the correction of the TIR images for atmospheric attenuation (the reduction in the intensity of the electromagnetic radiation in the earth's atmosphere) which may have significantly overestimated the final radiant temperature values. Given that the study area has a massive heat output at the

surface, the atmosphere between the ground surface and sensor elevation at ~ 1200 m AGL, is highly stratified. Hardy also neglected to adjust the radiant flux estimations from effects of background heat flux stored in the ground due to incoming solar radiation, which was found to be a large fraction of the total radiant flux (approximately 88% of the total radiant flux in the area) (Seielstad and Queen, 2009). Seielstad and Queen (2009) improved Hardy's method by developing an approach to estimate the radiant flux due to solar radiation (background heat flux). They assumed that the heat flux of areas adjacent to, but outside of a previously defined geothermal areas, is representative of background flux in the basin. They classified the basin to five land-cover types (forest, water, sinter soil, and road) and sampled them for background flux outside the geothermal areas. Then they estimated weighted mean flux within each land-cover class to produce total flux by a class. Our observation of the radiant temperature outside the previously defined geothermal polygon indicated presence of areas with high temperatures that matches the temperature of some of the areas within the geothermal polygon. Using the weighted mean flux to estimate the heat flux out of the background areas raised a question about the bias associated with the presence of hot areas within the defined background areas. In our study we followed an recommendation by Vaughan et al. (2012) to define the background areas in NGB. They used ASTER and MODIS thermal satellite infrared imagery to quantify the radiant flux in YNP. They defined a background area with similar topographic and land surface cover characteristics, similar elevation and topographic characteristics as the thermal area (to minimize the effects of differential elevation, slope and aspect), and similar surface cover types as the thermal area (to minimize the effects

of variable surface emissivity and transpiration in vegetation). The authors then estimated the radiant geothermal heat flux by subtracting the radiant flux of the background areas from the total radiant flux.

4.1.2. The CESU Agreement between the National Park Service Ecological Unit and Utah State University

After Hardy and Seielstad and Queens's studies, a long-term study of the hydrothermal features in NGB was needed to continue the monitoring program and to monitor any changes in the radiant temperature and heat flux of the hydrothermal features. Accordingly, the CESU Task Agreement between Utah State University (USU) and the National Park Service was initiated in 2005. The goal from the agreement was to continue exploring the use of high-resolution airborne remote sensing imagery to develop a consistent and repeatable method for image acquisition and processing to enable year-to-year comparison among the remote sensing images, and to gather accurate and continuous information about the thermal activity in NGB (Neale et al., 2011). The agreement included acquisition of annual, and in some years, biannual TIR and multispectral images of the hydrothermal areas in YNP between 2005 and 2013. The first three years of the monitoring program have resulted in improvement in image processing and calibration techniques that have led to high quality systematically reproducible images (Neale et al., 2016).

4.1.3. Objectives of Study

This study represents the second phase of the airborne remote sensing campaign study in NGB. The first phase focused in building the digital system by selecting the imaging sensors and filters, correcting the images for lens vignetting effects and radial

distortion, setting the specifications for flight lines and data acquisition protocols, testing different software for image strip formation and georeferencing, correcting the thermal infrared images for atmospheric effects and surface emissivity, and general modification of the remote sensing system along the course of the project. Description of this phase of the project was given in Neale et al. (2016).

In this context, the objectives of the present study includes 1) using the previously created, georeferenced and corrected TIR and emissivity images to calculate the pixel radiant flux for NGB, 2) determine and compare year-to-year radiant flux values, 3) compare the relevance of the results to previous studies that used similar methods, 4) define background areas suitable for estimating the radiant flux due to solar radiation, 5) estimate the radiant flux corrected for solar effect and determine and compare the radiant flux of high-priority thermal areas in NGB, 6) draw a conclusion about the effectiveness of the method and set recommendation for future application of airborne remote sensing technology in thermally active areas.

4.2. Methods

The methods section of this study is divided into two parts, 1) image acquisition and processing, and 2) image analysis. Image acquisition and processing is described briefly to generally explain the method used to acquire the images including description of the spectral range, spatial resolution, correction of TIR images for atmospheric radiation and surface emissivity, and the accuracy and precision of the method. More details about these processes are discussed in Neale et al. (2016). In the methods section,

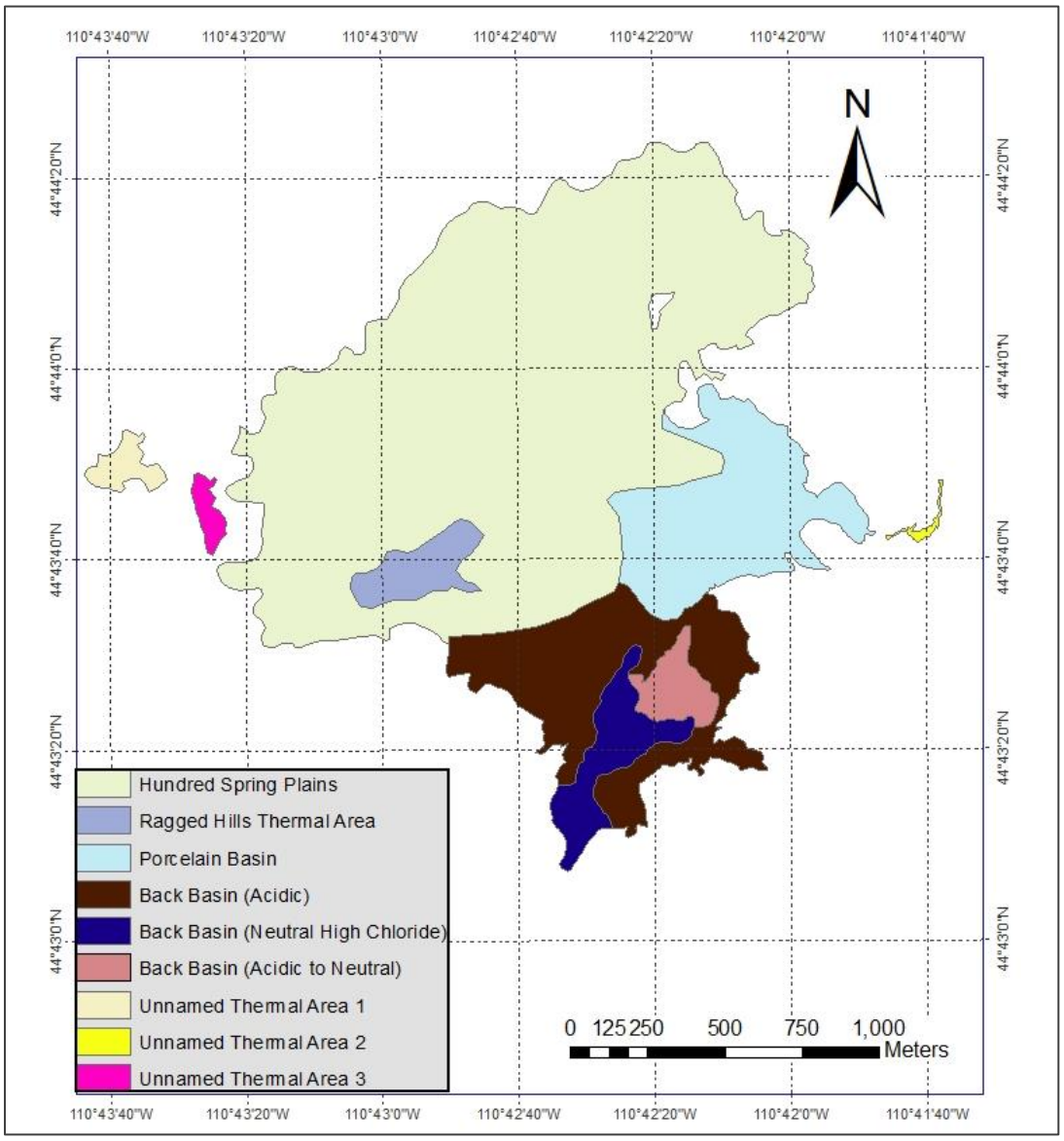

Fig. 4.1. The sub basins comprising Norris Geyser Basin (created by Hutchinson (1997) (unpublished data available from the Yellowstone Center for Resources GIS geodatabase)).

more focus is given to the image analysis part of the method, including surface classification, estimation of the heat flux due to solar radiation effect, identification of geothermal regions within NGB, and estimation of the radiant flux and heat power from the selected geothermal region.

4.2.1. Image Acquisition and Processing

The two types of airborne remote sensing images used for the analysis in this study were the thermal infrared images (TIR) and multispectral images (MS). The TIR images cover the thermal range between 8-12 μm of the electromagnetic spectrum and provide information about the surface radiometric temperature. The MS images include the spectral bands green (0.545-0.56 μm), red (0.665-0.68 μm), and near infrared (0.795-0.806 μm) and are typically used as a base map for map-to-map rectification of the TIR images, and to correct the TIR images for surface emissivity as explained below. At least one TIR image was acquired annually between 2008 and 2013 in NGB using USU airborne remote sensing digital system (Fig. 4.2). TIR images were typically acquired during nighttime hours, under clear skies to maximize radiative heat loss and minimize warming effect from clouds. The images were acquired from an average elevation of 1800 m AGL to maintain an approximate spatial resolution of 1 m. One image comprised of approximately 640 x 480 pixels covering an approximate area of 0.64 x 0.48 km^2. Single TIR tiff images were georeferenced using the MS orthorectified image base map by identifying common control points within the images. The root-mean-square error (RMSE) for image rectification was kept to less than 1 m to maintain high positional accuracy. The georeferenced single TIR tiffs were assembled into image strips along the flight lines and then the strips were stitched into uncalibrated TIR mosaics, covering the NGB area.

The georeferenced uncalibrated TIR mosaics were then corrected for atmospheric effects. The radiation energy received at the sensor, located in the airplane, generally

includes the terrestrial emission transmitted through the atmosphere, the upwelling atmospheric emission transmitted through the atmosphere, and the downwelling atmospheric emission reflected by the surface and transmitted through the atmosphere. The correction of the images for these atmospheric effects was done to isolate the latter two components and yield an estimate of the terrestrial emission. To calculate the transmissivity and atmospheric emission terms, Moderate Spectral Atmospheric Transmittance Algorithm Model (Modtran 4) was used in conjunction with a local radiosonde profile data obtained from the University of Wyoming station in Riverton, WY (Berk et al., 1999). The Modtran 4 is iterated over the range of scan angles (θ) observed over the scene. Following surface emission, the atmospheric effects (transmission and emission) are determined by the path length through the atmosphere, which can be approximated as a function of the scan angle of the sensor. The upwelled atmospheric emission is calculated as the sum over the thermal band after taking the sensor response into account. A modified form of the Planck equation is used to estimate the actual surface emission (Brunsell and Gillies, 2002).

Besides the correction for atmospheric disturbances, the TIR images were corrected for surface emissivity (the ratio of the energy radiated from the surface to that radiated from a blackbody at the same temperature and wavelength, under the same viewing conditions). When the images were acquired, a value of 1 was assigned for emissivity of the surface. This assumption considers the surface as a perfect emitter or a black body. Typical surface emissivity values vary with surface cover (i.e. soil, water, or vegetation). Ignoring the correction for surface emissivity can result in overestimation of

the radiometric surface temperature by a number of degrees Celsius. The pixel emissivity was determined based on the relationship with the amount of vegetation present within a pixel following Brunsell and Gillies (2002). The vegetation cover represented by the normalized difference vegetation index (NDVI) is the function of the surface derived reflectance in the red and near infrared bands. The fraction of vegetation (Fr) within a pixel is a function of the NDVI of the minimum emissivity (0.9) estimated for bare soil and NDVI of the maximum emissivity (0.98) for a dense vegetation canopy. The emissivity of the different classes is determined by linearly relating the fraction of vegetation to a bare sinter soil emissivity and a full vegetation emissivity. The effective emissivity of the pixel can be written as a function of the fractional vegetation cover.

The final mosaic of surface emissivity was created using the model builder in ERDAS Imagine software (Guide, 2008). The model maker in ERDAS Imagine uses the emissivity layer, the MS image, and the at-aircraft temperature image corrected using Modtran 4 to obtain the corrected surface temperature image. In general, the corrections for atmospheric disturbances and emissivity decreased the values of the at-aircraft temperatures by several degrees.

4.2.2. Potential Bias in the TIR Images

The accuracy and precision of the method to create the final atmospherically adjusted and emissivity corrected TIR images can be discussed from three different perspectives i.e. relevance of the estimated radiometric temperatures to the measured kinetic temperatures, spatial accuracy of the features, temporal consistency of the TIR images.

4.2.2.1. Accuracy of Radiant Temperatures

The radiometric temperature measured at the sensor level in the airplane should ideally match of the surface kinetic temperature. However, atmospheric effects may result in erroneous radiometric temperatures estimates. The atmospheric correction explained in an earlier section can improve the accuracy of the radiometric temperature; however, it might not completely overcome the bias. Bias in the radiometric temperature can also occur if the initial assumptions of surface emissivity that were input into Modtran of sinter soil and vegetation were inaccurate. Typical range of emissivity of the whitish-colored siliceous sinter soils in the thermal wavelength range between (8-12 μm) is 0.86-0.92 (Vaughan et al., 2005). A sensitivity analysis for the typical range of sinter soil emissivity revealed maximum difference in temperature is 7.13 °C for $\varepsilon = 0.86$ and $\varepsilon = 0.94$.

Neale et al. (2016) compared the radiometric temperature from 2008-2012 acquisitions and the relevant kinetic temperature measured with thermistors of six ground control points within NGB including Cinder Pool, explosion crater pool, an unnamed pool, Nuphar Lake, the reservoir, and two bare ground locations, after accounting for positional inaccuracy (5-6 m). Their result showed an agreement between the radiometric temperature and relevant kinetic temperature for temperature values less than 35 °C with RMSD value of 3.3 °C and mean bias error of -1.8 °C. However, the RMSD for kinetic temperatures greater than 35 °C was 19.1 °C with a mean bias error of -16.8 °C. Neale et al. (2016) explained the possible reason from the mismatch at higher temperatures was due to the cloud of water vapor developed above hydrothermal pools with high

temperatures. Water vapor, generally, absorbs the thermal energy at 8-12 µm wave length resulting in lower radiant temperature estimates (Haselwimmer and Prakash, 2013; Seielstad and Queen, 2009).

4.2.2.2. Accuracy of Spatial Referencing

Qualification of the spatial accuracy of the method is generally a challenging process that is done through assessment of the location of easily identified control points within the TIR image compared to their location in the MS base map. Difference between the two locations defines the spatial bias within the TIR image. Neale et al. (2016) reported an offset of approximately 1-7 m between the visually rectified TIR night mosaics acquired in 2008-2012 and the same control point on the orthorectified visible mosaic. We measured the distance between Norris Museum building that appeared in April 2013 and October 2013 TIR images and the MS base image from 2010 and found the offset was about 5-3 m in the X-direction and 3-1 m in the Y-direction, respectively.

4.2.2.3. Accuracy of Temporal Representation

Maintaining an acceptable temporal accuracy is significant for year-to-year comparison of the hydrothermal features in NGB. The method used to acquire, process, georeferenced, and correct the radiometric TIR images was consistent throughout the project as explained in the method section. Neale et al. (2016) used the maximum temperature values in the images as an indicator of the temporal accuracy of the method. The maximum temperature in the image is relevant to hydrothermal feature with high kinetic temperature approaching the boiling temperature at Norris elevation (~ 90 °C). The temperature of these features is unlikely to be affected by weather and

meteorological conditions. The average of maximum temperature in all TIR images, acquired between 2008 and 2013, was 70.82 °C with 3.95 °C standard deviation. The small standard deviation gives an insight of the temporal accuracy of the method.

4.2.3. Image Analysis

The purpose of this study was to continue exploring the technical effectiveness of using airborne remote sensing to monitor the hydrothermal features in NGB and to observe possible temporal and/or spatial changes that may indicate signs of increased subsurface activity. In the first part of the analysis, the radiant flux (W/m^2) and radiant power (Watts) were estimated for all seven surface classes in NGB including bare soil, bare soil with siliceous sinter deposits, lakes and pools, river, grass, forest (bine trees), and mud pools, without removing the heat flux due to solar radiation. The pixel radiant flux (q) was calculated using Stefan-Boltzmann equation as

$$q = \varepsilon \sigma T_S^4 \quad (1)$$

where ε is pixel emissivity, σ is Stefan-Boltzmann constant (5.67E-8 $W/m^2/K^4$), and T_s is pixel radiant temperature from the TIR image.

To test for the technical effectiveness of the method, the results of radiant flux and radiant power were compared to the results from Hardy (2005) and Seielstad and Queen (2009), which were strongly consistent. Weather conditions during the images acquisitions were also investigated to determine possible discrepancy in the results due to differences in weather conditions.

The second part of the analysis evaluated year-to year changes in the geothermal heat flux and heat power in NGB. To estimate year-to-year changes in the geothermal

heat, the heat flux due to solar radiation was estimated and removed from the total radiant flux images. Removing the heat flux naturally stored in the soil from solar radiation is essential to enable the year-to-year comparison of the heat flux from subsurface changes related to tectonic, hydrothermal or impending volcanic processes. Therefore, the background heat flux was estimated for the seven surface classes following the recommendation by Vaughan et al. (2012). That heat flux was subtracted from the total radiant flux to enable further year-to-year comparison of the heat power from mainly the geothermal source.

4.2.3.1. Classification of Surface Cover

Prior to estimation of background heat flux, classification of land cover was conducted using the multispectral imagery. The surface classes were obtained using the unsupervised classification method within the ERDAS Imagine software (Guide, 2008). This method classifies the pixels of the multispectral image into a finite number of individual classes which were grouped to seven different classes including bare soil, bare soil with chemical deposits (sinter), forest (pine trees), grass, river, lakes and pools, and an un classified class. The unclassified class includes all pixels that were no classified as one of the six first classes (i.e. asphalt roads, paved roads, etc.). The unsupervised classification approach uses the ISODATA (Iterative Self Organizing Data Analysis Technique) algorithm available in ERDAS Imagine as one of the options. The classification was initially based on 100 classes with 12 maximum number of iterations and convergence threshold of 0.97. These classes were then grouped into the seven major surface classes mentioned above (Fig. 4.4).

Fig. 4.2. The USU LASSI LiDAR and airborne multispectral remote sensing system including FLIR SC640 thermal IR camera installed in the Cessna TP206 remote sensing aircraft.

4.2.3.2. Estimation of Background Heat Flux

Different methods were used to estimate the effect of the absorbed solar radiation on each of the seven surface classes during summer and winter acquisitions.

4.2.3.2.1. Bare Soil and Sinter Soil Classes

The effect of solar heat in bare ground is a function of many factors including elevation, slope, and aspect (Vaughan et al., 2012). To account for these factors on the estimate of the background heat flux, areas with bare soil and sinter deposits were classified into nine aspects (i.e. north, northeast, southeast, east, south, northwest, southwest, west, and flat) and six ranges of slope with 10 degrees increments from 0° to 60°. Two flat areas were selected for each of the two classes out of the hydrothermal polygon, defined by Hutchinson (1997), at the northwest side of NGB. The skin temperature of that area was within the lowest seventh percentile of the radiant temperature of NGB. The coordinates of the center of the background areas are centered at -110° 43' 23.174" W and 44° 43' 30.756" N for sinter soil and at -110° 43' 22.819" W

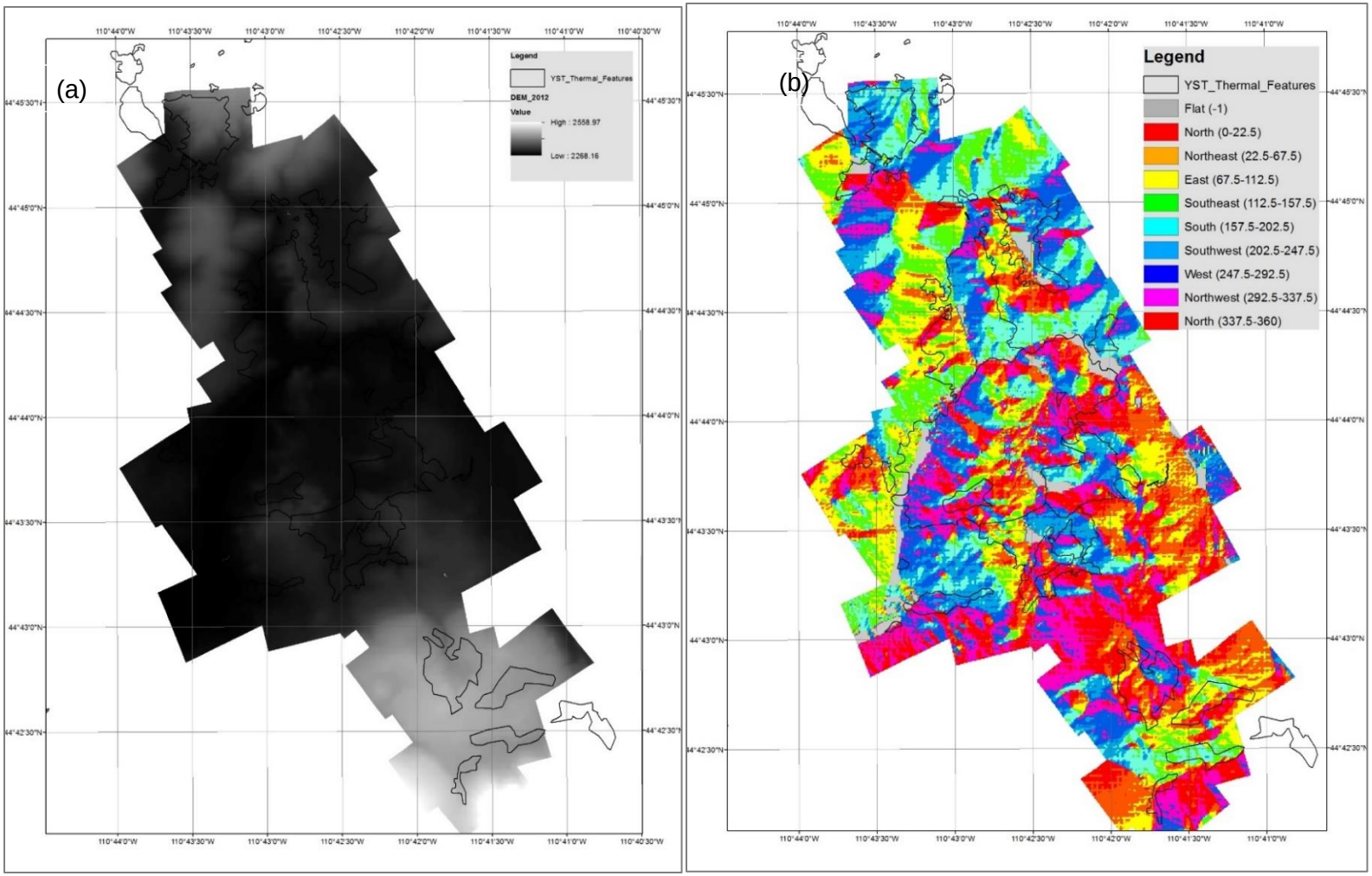

Fig. 4.3. USU LiDAR image showing the elevation of NGB (a), and the aspects layer calculated for NGB from 2012 Acquisition.

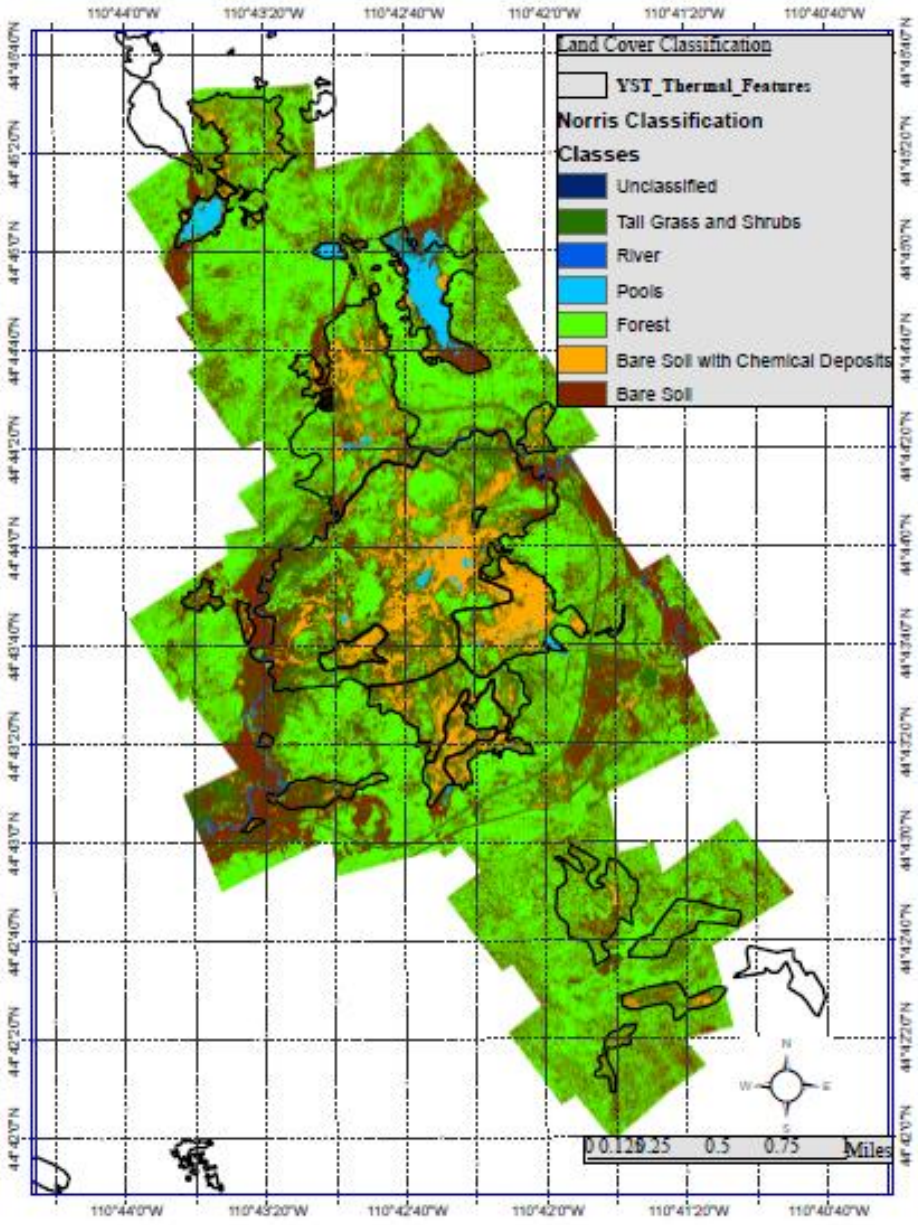

Fig. 4.4. Land cover classification image for the 2012 multispectral acquisition, defines seven different surface cover classes.

and 44° 43' 35.416" N for bare soil. The aspect and slope raster maps for every TIR image were calculated using the LiDAR image created by Utah State University with the LASSI LiDAR system (Fig. 4.3.a). A raster map was created for solar beam irradiance ($Wh/m^2/day$) for the different months of image acquisition (September, October, March,

and April) using the Solar Irradiance and Irradiation Model available in Grass GIS 7.2 software (Team, 2016). Grass GIS model requires information about elevation, slope, and aspect of the area, surface albedo, atmospheric turgidity coefficient, and clouds and haze coefficients. The Linke atmospheric turbidity coefficient for a mild climate in the northern hemisphere was estimated for the month of September as 2.1 for mountain areas and 2.9 for rural areas (Kasten, 1996). A sensitivity analysis showed that the difference in solar beam irradiance using these two values was about 50 Wh/m^2/day compared to the total solar beam irradiance of 7816.28 Wh/m^2/day. Clouds and haze coefficients were assumed zero since the TIR images were usually acquired during clear days.

The beam solar irradiance was estimated for each aspect in different ranges of slopes which resulted in total number of 54 raster maps for each of the four months. The average of the beam irradiance for each raster was calculated and the ratio between the averages and the average beam irradiance of the flat aspect was calculated (Fig. 4.5). To estimate the heat flux due to solar radiation for each raster map, it was assumed that the ratio between the beam irradiance of that raster map and the beam irradiance of the flat background area equals the ratio between the temperature of that raster map and the temperature of the flat background area as

$$\frac{Beam\ Irradiance\ of\ a\ raster\ map}{Beam\ Irradiance\ of\ flat\ background\ area} = \frac{Temperature\ of\ a\ raster\ map}{Temperature\ of\ flat\ background\ area} \quad (2)$$

The background temperature for each pixel was then estimated given the temperature of the background flat area which was determined from the TIR images (Table 4.1).

This method was applied only for September and October imagery. During March and April flights, the average temperature of the background areas was far below zero

degrees Celsius (Table 4.1). The data of the SNOTEL station in west Yellowstone indicated considerable amount of snow accumulation at the time of the latter two acquisitions. To avoid the error from snow accumulation in estimating the background heat flux, the ratio between the radiant flux raster map during September acquisition and the solar raster map was factored using the ratios in Fig. (4.5) for each aspect and slope range, to estimate the ratio during March and April. The estimated ratio was used to back calculate the solar rater map for March and April images

The effect of elevation on solar effect was neglected in this study. It was extremely difficult to find background areas for the sinter class outside the geothermal polygon that had low radiant temperature values. Incorporating additional factor such as elevation to select the background areas would make it rather impossible to define a background area for sinter class. However, the elevation range in NGB ranges between 2258.97 m and 2268.16 m. So, variability in solar effect due to difference in elevation is expected to be non-significant.

4.2.3.2.2. Lakes and Pools Class

Norris Geyser Basin carries a number of thermal and non-thermal lakes and water pools including the reservoir, Explosion Crater Pool, Hebgen Lake, Sieve Lake, Congress Pool, Lava Pool, Gray Lakes, Cinder Pool, and Nuphar Lake besides a number of unnamed pools. Nuphar Lake is considered the cooled lake in NGB with measured kinetic temperature of 9.4 °C. White et al. (1988) described the lake as a cool lake that is fed with rain water and small thermal springs and has no outlet. The Nuphar Lake was considered as a background lake to estimate the background heat flux. This assumption

does not take into consideration the differences in elevation, lake's surface area, or depth.

4.2.3.2.3. River Class

Two major rivers flow in the NGB, the Tantalus Creek and the Gibbon River. The Tantalus creek, the tributary of the Gibbon River, drains the entire basin to the influence with the Gibbon River at the north side of the basin. The Gibbon River rises in the center of the park at Grebe Lake. It flows west through mostly Lodgepole Pine forest and open meadows and cross Norris Canyon Road and Grand Loop Road to enter NGB through the east border. The Gibbon River collects thermal water from the Tantalus Creek at the confluence north Hundred Spring Plains. The temperature of the river at the east entrance of NGB was assumed to represent the background solar temperature. The radiant flux estimated using that background temperature was subtracted from the radiant flux from the river to remove the solar heat effect.

4.2.3.2.4. Forest and Grass Classes

Different types of trees including Douglas-fir and pine trees and of small trees and grass comprise more than 50% of the area of the basin. To remove the background heat flux from these two classes from September and October images, one area for each class was chosen outside the geothermal polygon, in the northwest side of NGB, close to the background areas of sinter and bare soil. The center of these background areas is at -110° 43' 29.731" W and 44° 43' 38.267" N for forest class and -110° 43' 25.323" W and 44° 43' 34.893" N for grass class.

4.2.3.2.5. Unclassified Class

The unclassified class includes pixels that were not identified as one of the latter six main classes. The unclassified class represent a less than 0.2% of the total area of NGB. Therefore the background heat flux was ignored as the total radiant flux.

4.3. Results and Discussion

4.3.1. Thermal Infrared Radiometric Images

The deployment of the airborne remote sensing project in NGB started in September of 2008. The TIR images acquired from 2008 to 2013 are shown in Fig. (4.6) with the black polygon overlaying the images defining the boundary of the hydrothermal areas in the basin created by Hutchinson (1997) (unpublished data available from the Yellowstone Center for Resources GIS geodatabase). The date, start time and end time of image acquisition and the area covered by each image are summarizes in Table (4.2). The TIR images covered most of NGB, and some parts of the Norris-Mammoth corridor, Gibbon Hill thermal area, Frying Ban Springs, Elk Park, and Roadside Springs. The TIR images from 2008 to 2011 acquisitions were acquired in late summer during September, on days and nights with clear skies, to minimize the interference from clouds. Air temperature during the nighttime acquisitions was close to freezing and therefore the surface cooled down rapidly after sunset due to radiative cooling. Images acquired in early fall (October 2013) and spring (March 2012 and April 2014) were used to compare the potential changes in radiant flux due to seasonal conditions and air temperature. The temperature range in the TIR image suggests large distinction among the thermal areas

that may include difference in locations of fractures/faults and/or permeability of the underline bedrock in the area. The differences are mostly noticeable in 2012 and 2013 winter images where the minimum temperatures are likely related to areas covered by snow. Some of the hot thermal features in NGB have kinetic temperatures approaching the boiling temperature at Norris elevation (~90 °C). The maximum radiant temperature for these features on the calibrated images were about 40 °C less than the kinetic temperatures. For example, in TIR image from 2008 acquisition, the maximum radiant

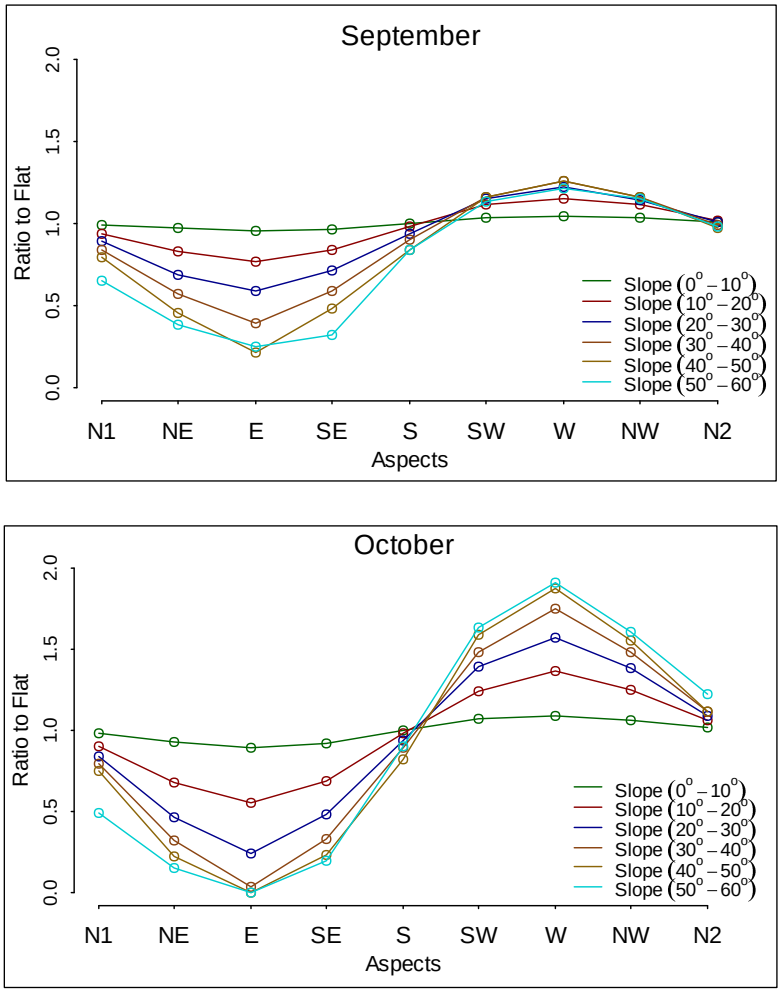

Fig. 4.5. Ratio of solar beam irradiance between different aspects and ranges of slopes and flat aspect during September, October, March, and April acquisitions.

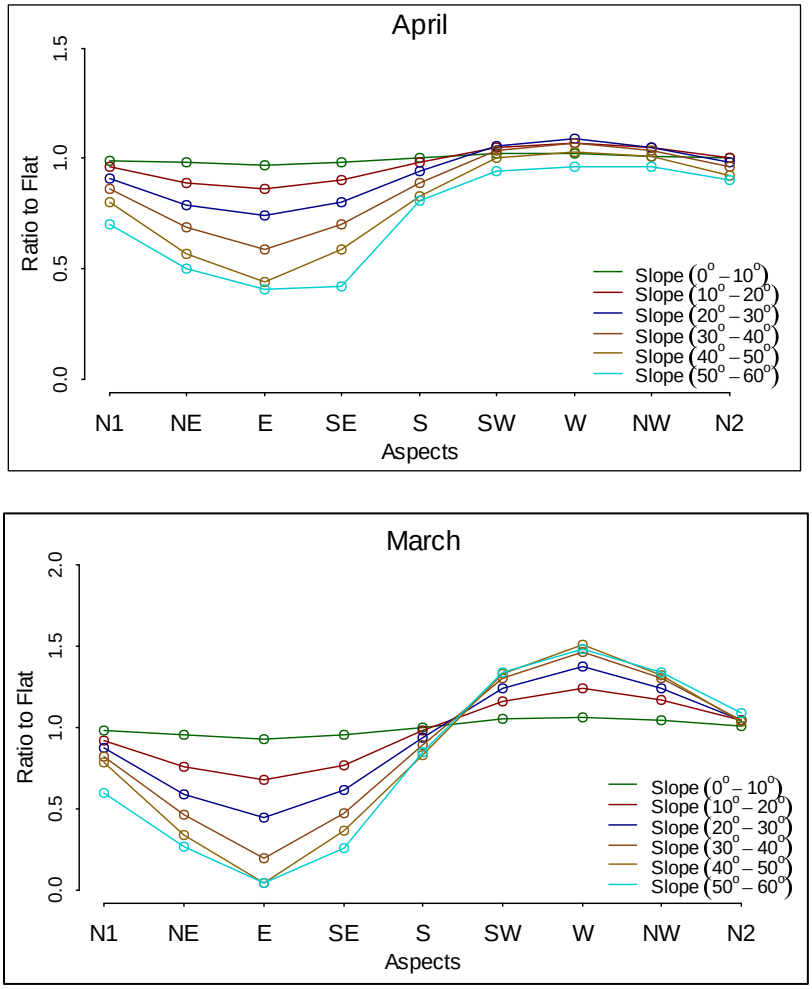

Fig. 4.5. (continued).

temperature at and around Steamboat Geyser was about 57.5 °C compared to the recorded kinetic temperature of about 93.0 °C (Ball et al., 2002b). Seielstad and Queen (2009) observed reduction in radiant temperature of hot features at night such as Gray Lakes, Frying Pan Spring, and Cistern Geyser, while the temperature of cold pools, such as Nuphar Lake, remained fairly similar. They attributed this phenomena to presence of steam cloud above the hot features. Neale et al. (2016) and Haselwimmer et al. (2013) also discussed the cooling effect of water vapor cloud above hot pools due to absorption

Table 4.1.

Temperature of the background area for all surface classes

Date of Flight	Time of Flight	Sinter Soil (°C)	Bare Soil (°C)	Forest (°C)	Grass (°C)	Lakes and Pools (°C)	River (°C)
12 Sept 2008	1:31 – 1:56	-3.6	-1.4	-1.1	-2.5	9.0	7.8
10 Sept 2009	3:36 – 3:53	-2.5	-1.2	-1.3	-0.9	10.0	7.2
25 Sept 2010	00:33 – 00:49	-4.5	-3.0	-2.4	-4.3	7.3	7.0
09 Sept 2011	00:08 – 00:31	0.3	1.4	0.8	0.6	11.8	9.9
09 Mar 2012	21:23 – 21:44	-8.8	-8.5	-5.3	-8.8	-4.8	6.3
25 Apr 2013	23:08 – 23:33	-9.9	-8.3	-6.0	-9.7	-2.6	5.9
25 Oct 2013	20:40 – 21:02	-2.4	-4.4	-4.0	-8.4	4.1	6.4

Table 4.2.

Dates and area covered by the TIR images and the radiant temperature range.

Image Date	Area Covered by Image ($*10^6$ m^2)	Radiant Temperature (°C)
12 Sept 2008	9.38	Min Temp: -3.2 Max Temp: 69.5
10 Sept 2009	9.09	Min Temp: -5.5 Max Temp: 73.8
25 Sept 2010	14.42	Min Temp: -5.6 Max Temp: 75.1
09 Sept 2011	12.57	Min Temp: -1.6 Max Temp: 71.3
09 Mar 2012	14.05	Min Temp: -12.6 Max Temp: 64.1
25 Apr 2013	16.64	Min Temp: -15.5 Max Temp: 74.1
25 Oct 2013	16.89	Min Temp: -11.3 Max Temp: 68.0

of the TIR thermal energy by water vapor in high temperatures. This observation suggests that the radiant temperature of the hot pools, fumaroles, and thermal springs was greatly underestimated.

4.3.2. Weather Conditions

Differences in weather conditions may explain some of the inconsistency among the TIR images due to differences in air temperature, wind speed, and changes in heat flow from precipitation or snow melt. The TIR images from 2008-2011 acquisitions were acquired during the month of September under mostly clear skies to maintain similar weather conditions. However, some differences in weather conditions prior to image acquisition were observed. A cool front passed through Yellowstone prior to the date of image acquisition on 12 September 2008. Average air temperature during the acquisition

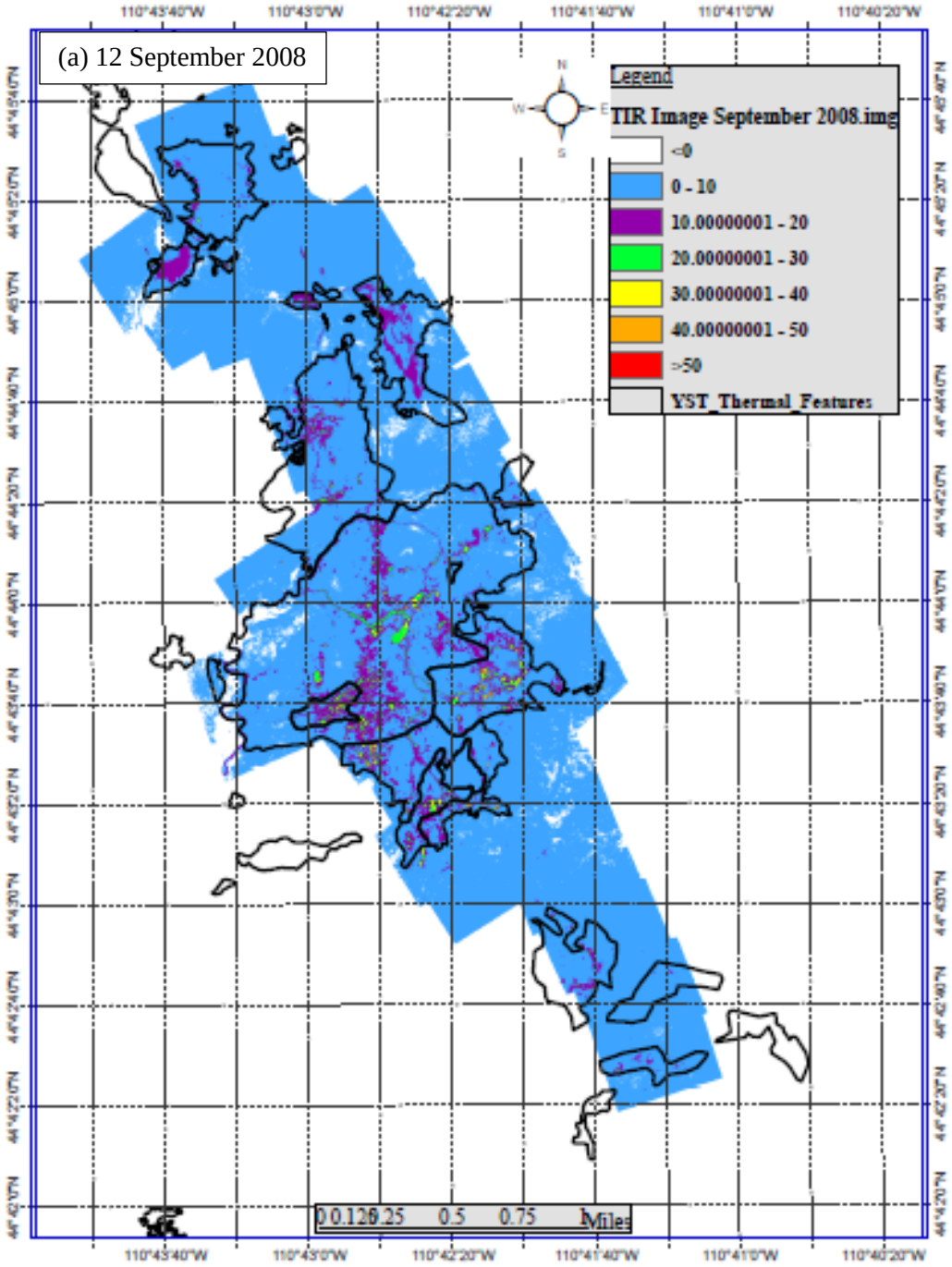

Fig. 4.6. The TIR images from the acquisition on 12 September 2008 (a), 10 September 2009 (b), 25 September 2010 (c), 09 September 2011 (d), 09 March 2012 (e), 25 April 2013 (f), and 25 October 2013 (g).

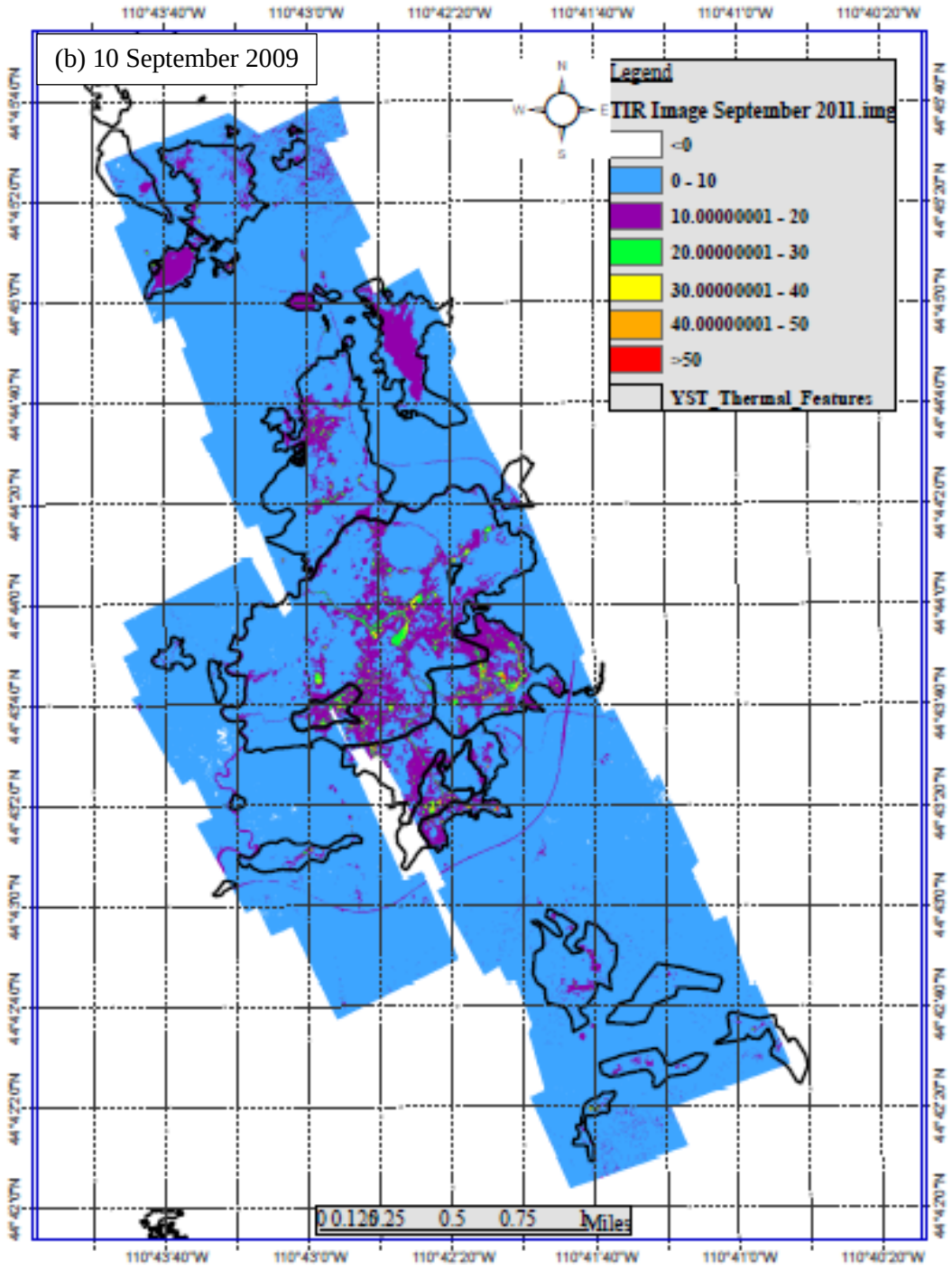

Fig. 4.6. (continued).

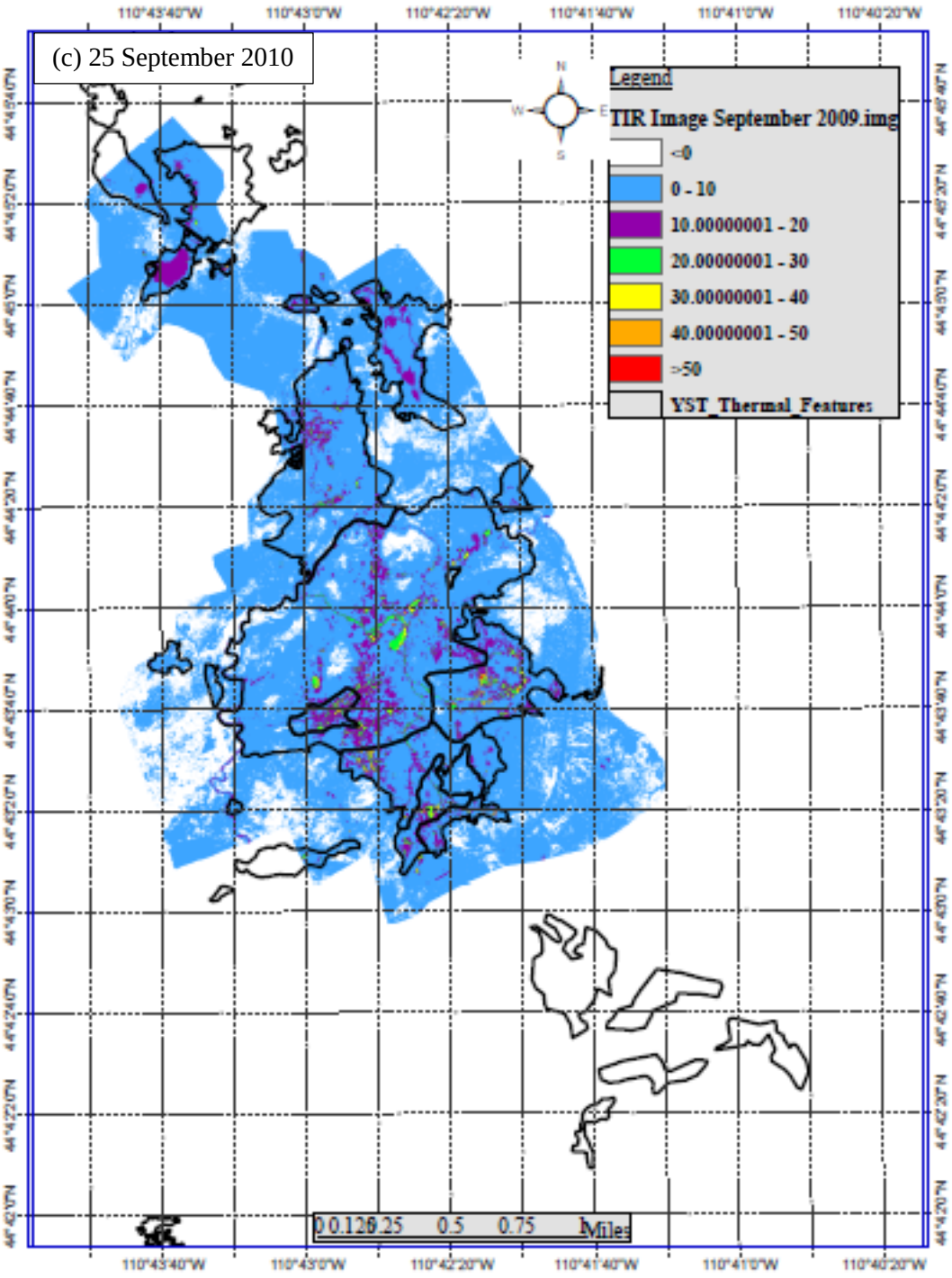

Fig. 4.6. (continued).

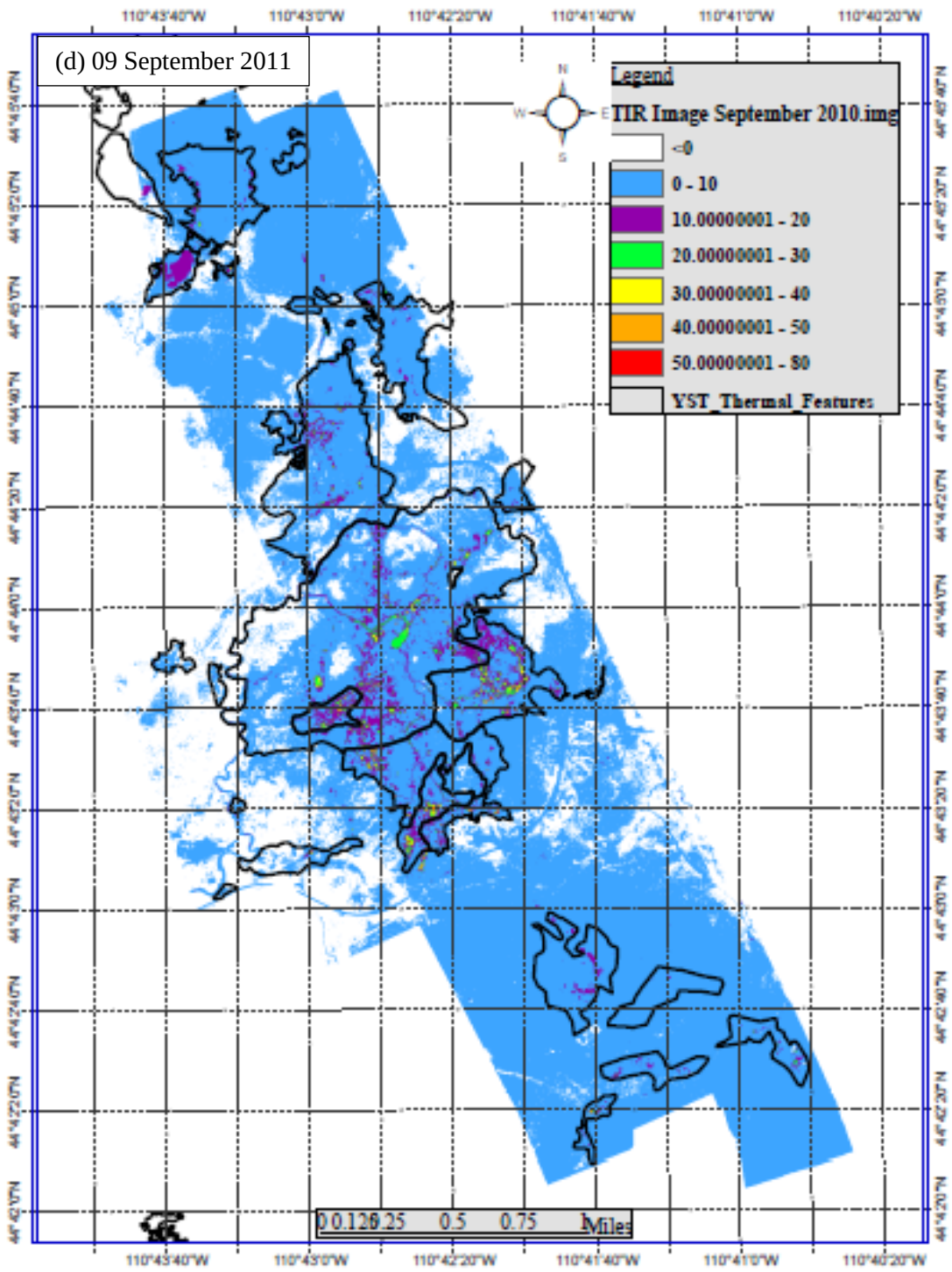

Fig. 4.6. (continued).

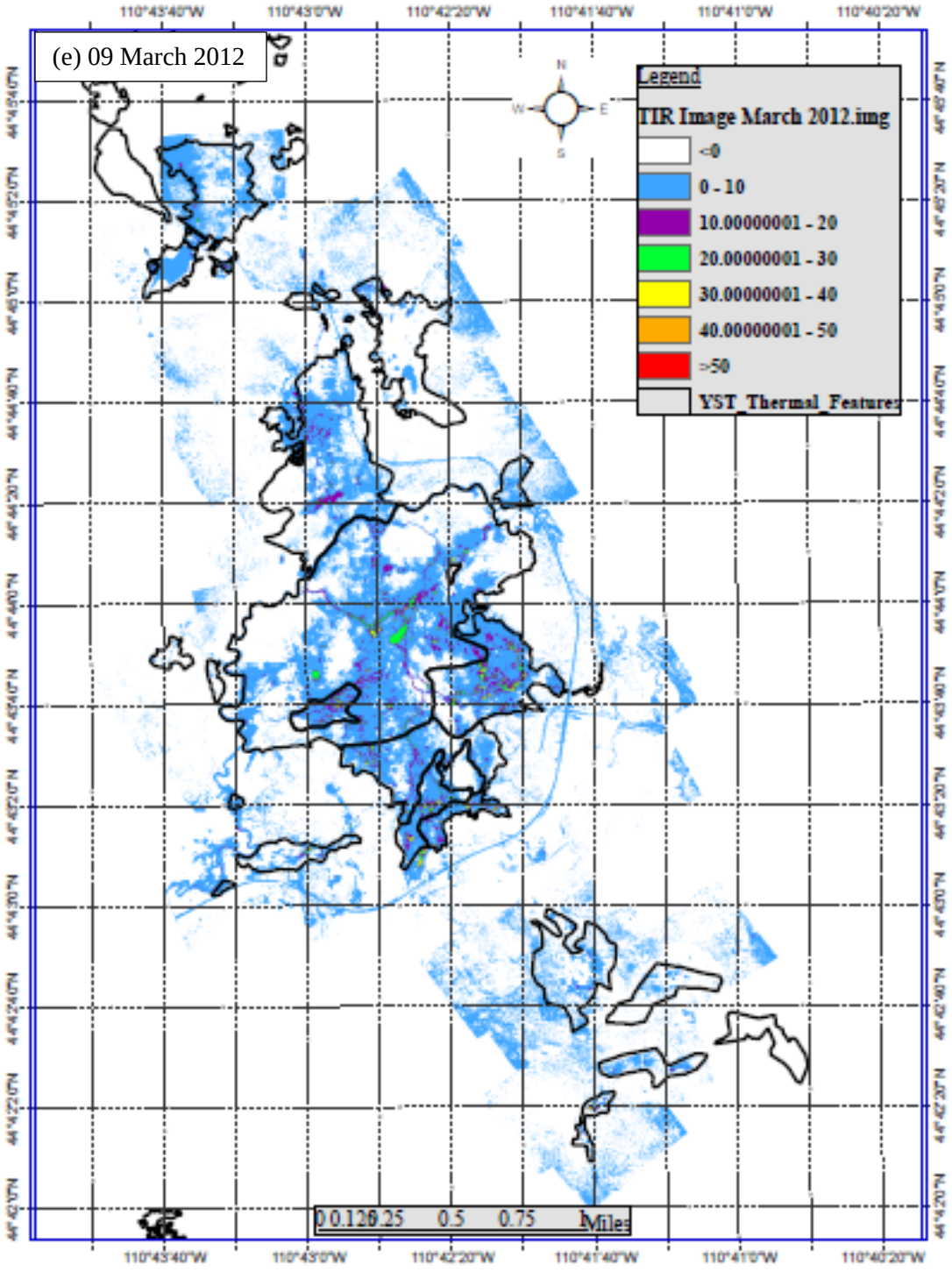

Fig. 4.6. (continued).

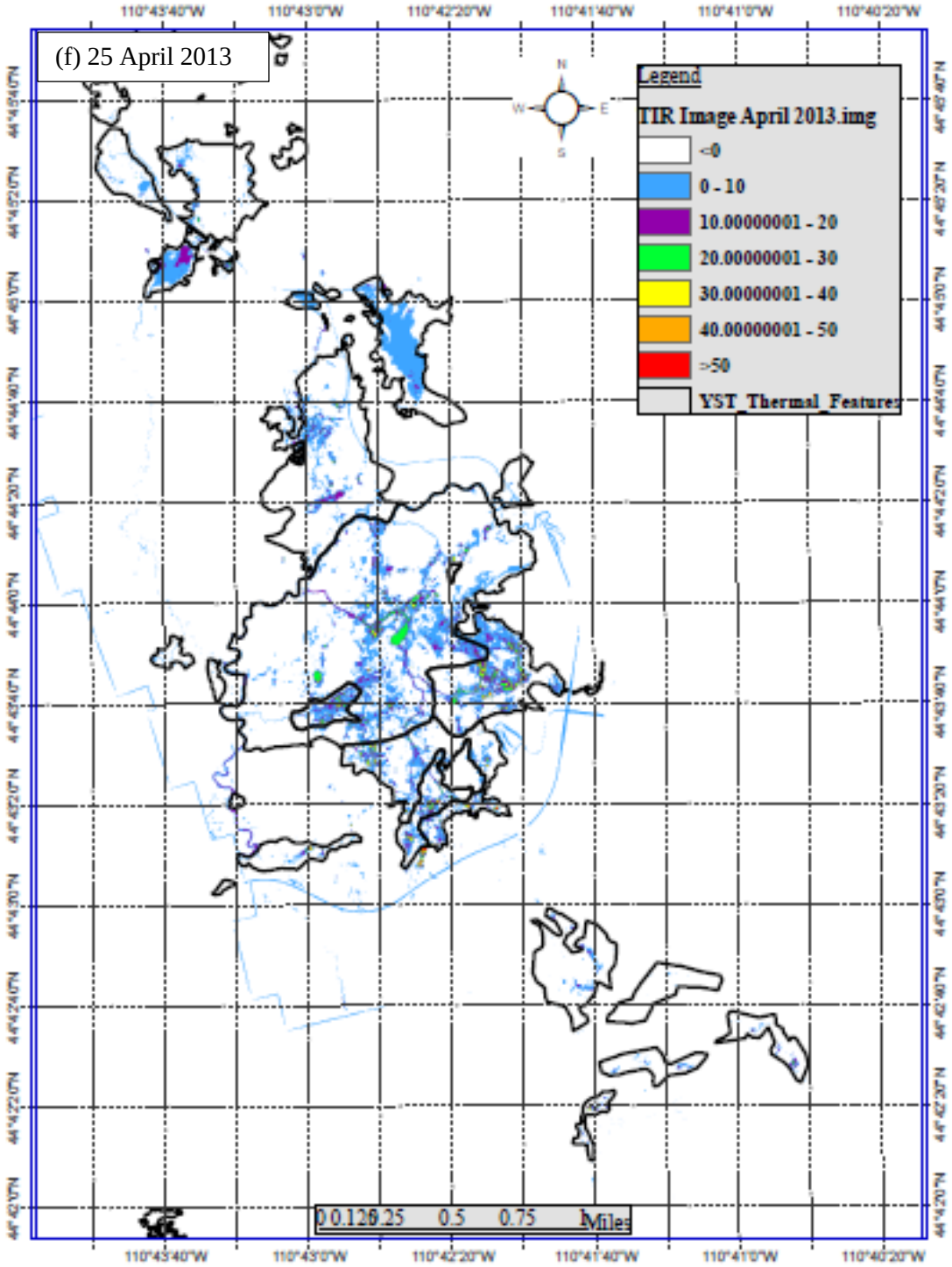

Fig. 4.6. (continued).

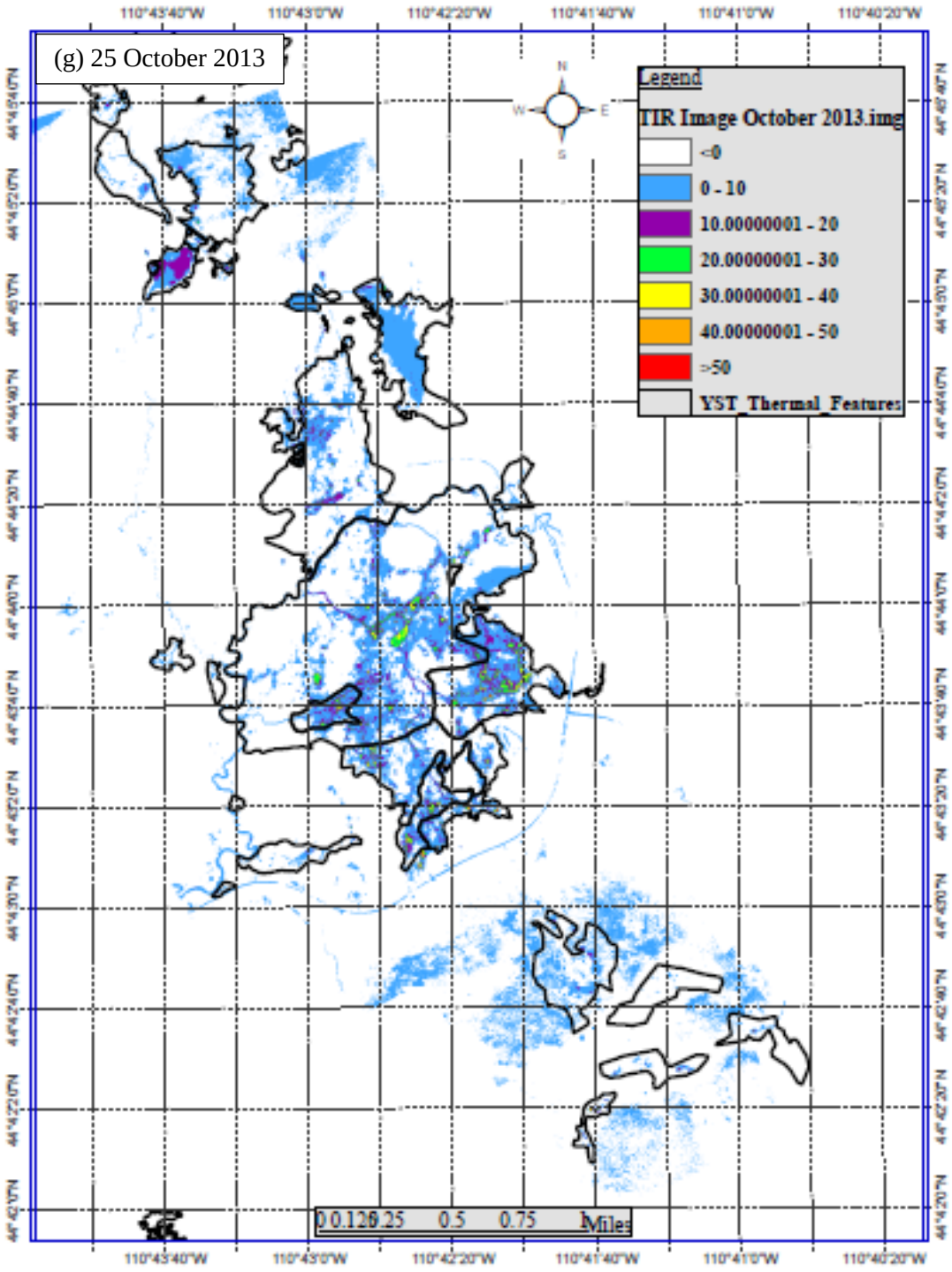

Fig. 4.6. (continued).

as measured by the Geology Program Onset temperature logger at the Norris Museum, was – 0.2 °C. Reduced maximum solar radiation (564 W/m^2) was recorded on 10 September 2008 at the YNP Lake meteorological station (Approximately 20 miles away from Norris) (Jaworowski et al., 2013). The maximum solar radiation recorded on 11 September 2008 was approximately 800 W/m^2 near noon with no precipitation recorded on either date.

The day prior to the time of image acquisition on 10 September 2009 had mostly clear skies with maximum solar radiation of approximately 807 W/m^2. Three days before the image acquisition, on 7 September 2009, the USU weather station in the explosion crater in Norris recorded about 0.5 mm of rain, cooling air temperatures by about 7 °C during the days of 7 and 8 September compared to the following two days. At the time of the image acquisition, wind speed was less than 1 m/s, average air temperature was 2.5 °C, and average relative humidity was about 90.1%.

A cool front passed through the area during the two days before 25 September 2010. Image acquisition took place on September 25 between 00:33 am and 00:49 am. The day before image acquisition was mostly cloudy and had maximum air temperature of 17.1 °C. During acquisition, air temperature was about 4.2 °C, average wind speed was less than 1 m/s, and relative humidity was about 86%.

The days preceding the acquisition in 09 September 2011 were mostly sunny with no recorded precipitation for the week preceding acquisition. Maximum solar radiation on 08 September 2011 was about 796 W/m^2. Average air temperature during the acquisition was about 5.8 °C

In 2012, average air temperature during acquisition was – 3.1 °C, average RH was 65%, and average wind speed was less than 1 m/s. SNOTEL station west Yellowstone reported 2 inches of precipitation on March 5 and March 7. On March 8, air temperature increased above zero degree Celsius during the day indicating snow melt. Maximum air temperature on March 9 was about 8 °C.

SNOTEL at west Yellowstone did not report precipitation on the week before the acquisitions on 25 April 2013 or 25 October 2013. Accumulated snow water equivalent decreased significantly during the week of 25 April indicating snowmelt due to the warm air temperatures during that week. Maximum air temperature on the day of image acquisition on 25 April was 10.3 °C and average air temperature during the hour of image acquisition was -2.5 °C. For the acquisition on 25 October, maximum air temperature on the day before image acquisition was 18.1 °C and average air temperature during the hour of image acquisition was -0.7 °C.

4.3.3. Total Radiant Flux and Heat Power

For this part of the study, radiant flux (W/m^2) and radiant power (watts) for the seven land cover classes in NGB were estimated to compare the results with Hardy (2005) and Seielstad and Queen (2009), who estimated the total radiant power over NGB in previous years. First, the effect from solar heating was not removed from of the total radiant flux image. The results of heat power for the entire basin ranged between 0.73 gigawatt in the 25 April 2013 to 0.85 gigawatt in 09 September 2011, with highest radiant power recorded during 2011, 2010, and 2009 acquisitions, respectively (Table 4.3).

Many factors should be considered when comparing the total heat power estimated from this study with Hardy (2005) and Seielstad and Queen (2009). Hardy (2005) estimated the heat power from NGB from the 09 October 2002 night acquisition as 1.5 gigawatt. This value is about 0.65 gigawatt higher than the highest heat power estimated in this study for 2011. The area covered by Hardy (2005) was 3,502,800 m^2. In this study, two hydrothermal features west of Hundred Springs Plain and a portion of the south east part of NGB were not covered by 2011 acquisition. Since all TIR images were cropped to a unified area suitable for the spatial and temporal comparison of heat power, excluding some area during 2011 acquisition has resulted in a smaller subset area (i.e., 2,486,823 m^2). Another important factor to consider is that Hardy (2005) ignored the atmospheric effect on the radiant flux values assuming that such corrections were not needed because the data were collected with a low-elevation airborne flight (~1200 m AGL). Average airborne flight elevation in our study was about 1800 m AGL. However, atmospheric disturbance was incorporated in the correction of the TIR images. Our comparison between corrected TIR images and uncorrected raw images reveled a maximum apparent temperature difference of about 8 °C. This observation suggests the importance of the atmospheric correction of imagery even at lower flight elevation given that the atmosphere is highly stratified between the ground surface and the remote sensing sensors at the airplane elevation. For Hardy (2005), ignoring the atmospheric correction could have resulted in an over estimation of the final radiant flux by approximately 37 W/m^2 which is equivalent to 0.13 gigawatt of heat power. Lastly, Hardy (2005) acquired their TIR images on a cooler day with maximum/minimum air

temperatures of 6.7/-2.8 °C. However, cooler air temperatures were expected to cool the ground surface resulting in a lower radiant flux output. This suggests that weather condition might not have been a significant factor for the discrepancy between heat power in Hardy (2005) and our study. A simple linear interpolation using the area and heat power from Hardy (2005) and the area covered by this study showed that the heat power equivalent to 2,486,823 m^2 is 1.06 gigawatt, which is 0.21 gigawatt higher than the highest heat power estimated in this study.

Seielstad and Queen (2009) estimated the total heat power from NGB using their nighttime TIR acquisitions on 11 and 12 October 2006, as 0.988 gigawatt and 0.919 gigawatt, respectively. The area covered by their study was similar to that covered by Hardy (2005). Weather conditions during and before the acquisition days were similar to the acquisition day in 2008, generally dry with clear skies and no precipitation records at least two days before the acquisition. Seielstad and Queen (2009) considered correcting the TIR images for atmospheric disturbances, which may contribute to the lower heat power values compared to Hardy (2005). A simple linear interpolation showed the heat output from 2,486,823 m^2 was 0.701 gigawatt for 11 October 2006 and 0.652 gigawatt for 12 October 2006, which was relatively lower than the lowest heat power estimated in our study on April 2013. Given the uncertainties in background heat flux and the noise from calibration and emissivity estimation, we conclude that the differences in heat power, from our study and Hardy (2005) and Seielstad and Queen (2009) studies, might not be significant.

Thermal chloride flux has also been used as a surrogate for convective heat flux in

YNP since 1976 (Fournier et al. 1976). The method is based on calculating the instantaneous chloride fluxes by multiplying the chloride concentrations by the river discharges recorded at the time of sample collection and calculating the equivalent heat power. The Tantalus creek is the primary drainage of NGB and carries a very high proportion of the thermal water derived directly from the hot springs in the basin. The creek was continuously monitored for water temperature and stream flow by USGS since summer 2010. Generally, the discharge and chloride flux from Norris Geyser Basin, as measured in Tantalus Creek, varies greatly with time. The average chloride load measured by USGS between 3 and 5 September 2010 was about 1,032,887 tons/year (Clor et al., 2012). This load is equivalent to 3.1 gigawatt convective heat power drained from the entire area of NGB. Comparing the 0.79 gigawatt radiant flux on 25 September 2010 to the 3.1 gigawatt convective heat flux suggests considerable amount of heat loss through sensible and latent heat fluxes. Future studies might consider estimating these two components of heat transfer to estimate an overall heat budget for NGB.

Fig. (4.7) shows the radiant flux images estimated from 2008-2013 acquisitions. The distribution of heat flux was generally consistent during 2008 and 2009 acquisitions. The cold area (<300 W/m^2) during 2010 acquisition was more than the double of 2008 and 2009. Weather conditions before the day of image acquisition (mostly cloudy with lower air temperatures) may explain this discrepancy. However, the hot area (>500 W/m^2) was greater than those of 2008 and 2009 acquisitions. This observation indicated that the increase in heat flux associated with hot thermal features was not greatly affected by the increase in soil moisture during 2009 acquisition nor by the cooler weather prior to

2010 acquisition. Effect of weather can be clearly seen in the pixels with low or no thermal heat source. The cool area (<300 W/m^2) during 2011 acquisition was less than 4% of the number during 2008 acquisition. Notice the increase in heat power over the entire basin in 2011 represented by fewer cool pixels (dark grey) in the northeast and northwest sides of NGB (Fig. 4.7. d). The National Park Service did not report any significant increase in thermal activity over NGB during that time. However, in summer 2011, the National Park geologists reported increased hydrothermal activity around Back Basin in NGB (Neale at al. 2016). The increase in heat flux over the entire basin in 2011 raises a question about possible basin-wide increase in thermal activity, especially that air temperature during image acquisition was similar to that of 2010.

Notable increase in the cooler area was observed in the radiant flux images of 25 April 2013 and 25 October 2013 (Fig. 4.7.f and Fig. 4.7.g and Table 4.4). However, the area of the hot pixels remained similar to that of 2008 despite the colder weather conditions. For example the heat flux of the reservoir and the explosion crater in NGB remained fairly similar during all acquisitions. Heat flux from hot hydrothermal features such as Whirligig Geyser and Valentine Geyser in Porcelain Basin, Steamboat Geyser, Echinus Geyser, and Veteran Geyser in Back Basin, and Cinder Pool in Hundred Springs Plain, remained above 600 W/m^2 during 2008 to 2013 acquisitions.

4.3.4. Radiant Flux Corrected for Effect of Solar Radiation (Geothermal Radiant Flux)

The heat flux from the background areas, outside of the thermal polygon, was subtracted from the total heat flux to compare year-to-year changes in the distribution of radiant flux due to the geothermal heat flux. Selection of the background areas was

challenging due to the large spatial heterogeneity of the ground skin temperature and the presence of hot pixels adjacent to cold pixels in the TIR images. Vaughan et al. (2012) explained the challenge to select background areas in geothermal grounds. Practically, it is not possible to select a background area that is perfectly suitable to remove the residual solar heat effect as such areas are characterized by unique mineral deposits and vegetation cover. Therefore the selected background areas may possibly still have unpredictable heat output from a geothermal source.

The output heat power values from each class after removing the solar effect are displayed in Table (4.5). These values ranged between 0.086 watts and 0.113 watts. Compared to previous study, Seielstad and Queen (2009) estimated the geothermal heat power from their October 11th 2006 night imagery as 0.081 gigawatt and from the following night image as 0.043 gigawatt. Our study provides a narrower range of radiant geothermal heat power although the TIR images were acquired in different seasons and weather conditions. Geothermal heat should be fairly be constant if no anomalous change was indicated by one of the six vital signs that include gas emissions from the hydrothermal systems, changes in seismic activity, and/or changes in Earth's magnetic, electrical, and gravity fields.

Fig. (4.8) compares the total uncorrected radiant power and the estimated radiant geothermal heat flux at the time of image acquisition. Sinter class encompassed the least reduction in radiant flux compared to the other classes. The high albedo of the whitish siliceous sinter explains why that class absorbed less solar energy. Forest class had alternatively large background heat flux. The background temperature of that class was

larger than bare soil and sinter deposit likely due to evapotranspiration processes.

4.3.5. Temporal Changes in Major Hydrothermal Features in NGB

After removing the heat flux due to stored solar radiation, the pixel radiant flux values were grouped into four ranges i.e. low (0-100 W/m^2), medium (100-200 W/m^2), medium high (200-300 W/m^2) and high (>300 W/m^2) (Table 4.6). The areas with high radiant flux >300 W/m^2 were mostly distributed around Porcelain Basin, the neutral high chloride area in the Back Basin, the southern part of the acid area in Back Basin, the Gap area, the mid-section of the Hundred Springs Plain, and the east side of Ragged Hill (Fig 4.9 and Fig. 4.10). Inconsistent changes in heat flux were observed in areas around Colloidal pools and Sunday Geysers, Congress pool, Whirligig Geyser, unnamed pool east of Whirligig Geyser, and north Crackling Lake. Changes were also observed in the mid-section of Back Basin, west of Tantalus Creek and around Grey Lakes (Fig 4.10). The number of hot pixels in these two areas was higher in 2010 and April 2013 and was lower in the rest of the years (Fig 4.10.c and Fig 4.10.f). Some smaller inconsistent changes occurred around other areas in the basin including Minute Geyser, Emerald Spring close to the walking trail between Emerald Spring and Cistern Spring, Steamboat Geyser, and Cistern and Echinus Geysers. High heat flux areas were also observed around Collapsed Crater Spring below Tantalus Creek and an unnamed feature west of Echinus Geyser.

The changes around the walking trails in Porcelain Basin and Back Basin, between 2008 and 2013, are shown in Fig (4.11.) and Fig. (4.12). Increase in the number of the hot pixels was observed in the east side of Porcelain Basin near the trail to Norris

Table 4.3.

Total radiant power calculated by multiplying pixel radiant flux by the pixel area

Time of Flight	Sinter Soil (gigawatt)	Bare Soil (gigawatt)	Forest (gigawatt)	Grass (gigawatt)	Lakes and Pools (gigawatt)	River (gigawatt)	Total Heat Power (gigawatt)
12 Sept 2008	0.234	0.188	0.223	0.146	0.012	0.046	0.807
10 Sept 2009	0.232	0.187	0.221	0.146	0.012	0.046	0.802
25 Sept 2010	0.230	0.183	0.219	0.143	0.012	0.046	0.792
09 Sept 2011	0.244	0.197	0.238	0.152	0.013	0.050	0.849
09 Mar 2012	0.222	0.178	0.218	0.137	0.011	0.045	0.771
25 Apr 2013	0.211	0.168	0.201	0.131	0.011	0.045	0.727
25 Oct 2013	0.272	0.173	0.207	0.135	0.012	0.046	0.803

Table 4.4.

The area (m^2) relevant to each range of radiant flux as shown in Fig. (4.7). Total radiant power (gigawatt) calculated by multiplying pixel radiant flux by the pixel area

Heat Flux Range (W/m^2)	12 Sept 2008	10 Sept 2009	25 Sept 2010	09 Sept 2011	09 March 2012	25 Apr 2013	25 Oct 2013
<300	139,977	182,861	421,676	6,948	679,383	1,981,330	1,721,689
300 - 400	2,274,812	2,232,167	2,001,334	2,382,287	1,766,051	463,676	718,564
400 - 500	66,828	68,223	58,288	91,704	40,352	39,659	46,000
500 - 600	4,632	5,867	7,052	7,007	3,679	4,689	3,340
>600	574	842	1,611	1,317	495	610	336

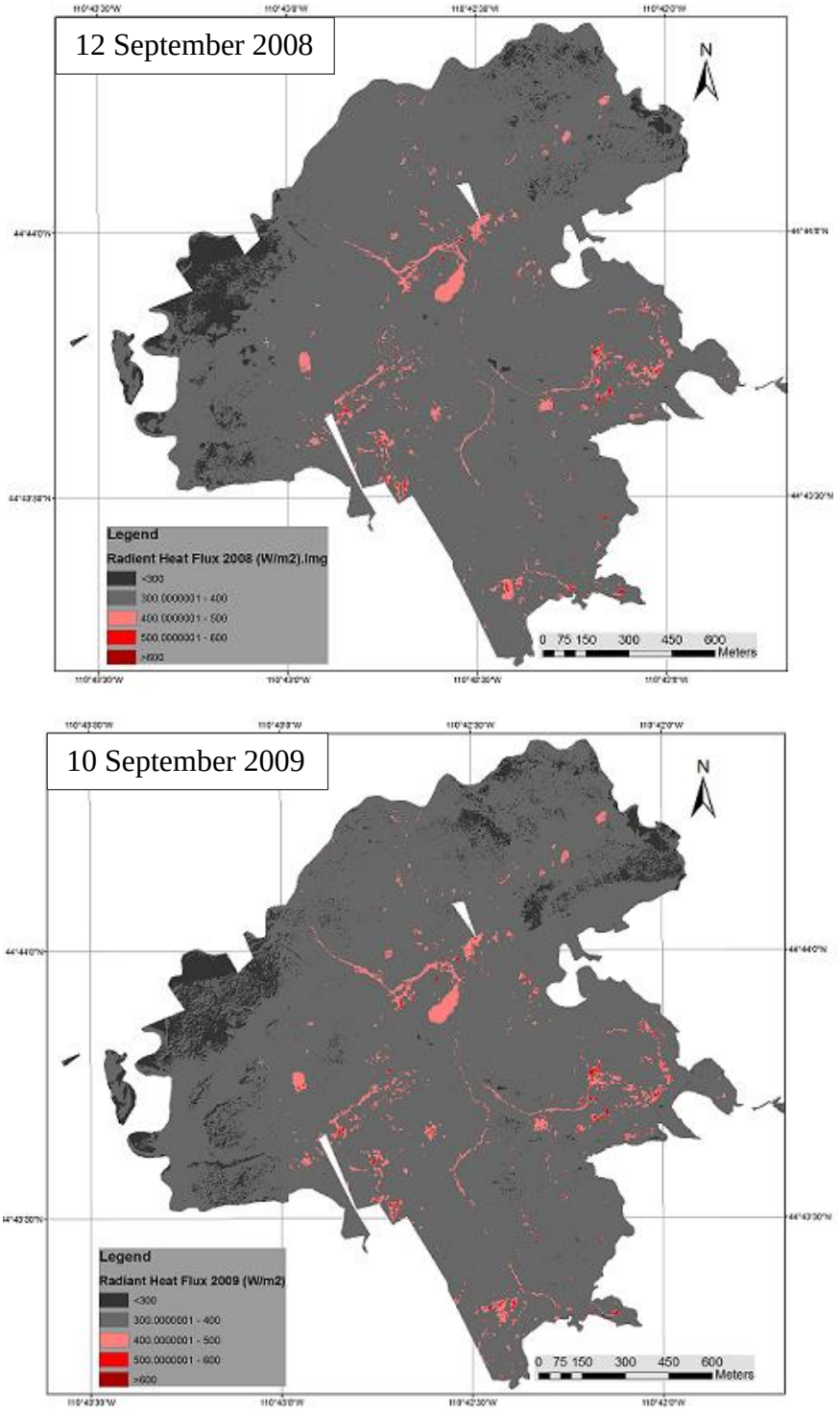

Fig. 4.7. Radiant flux (W/m^2) over NGB on 12 September 2008 (a), 10 September 2009 (b), 25 September 2010 (c), 09 September 2011 (d), 09 March 2012 (e), 25 April 2013 (f), and 25 October 2013 (g), without correction for solar effect.

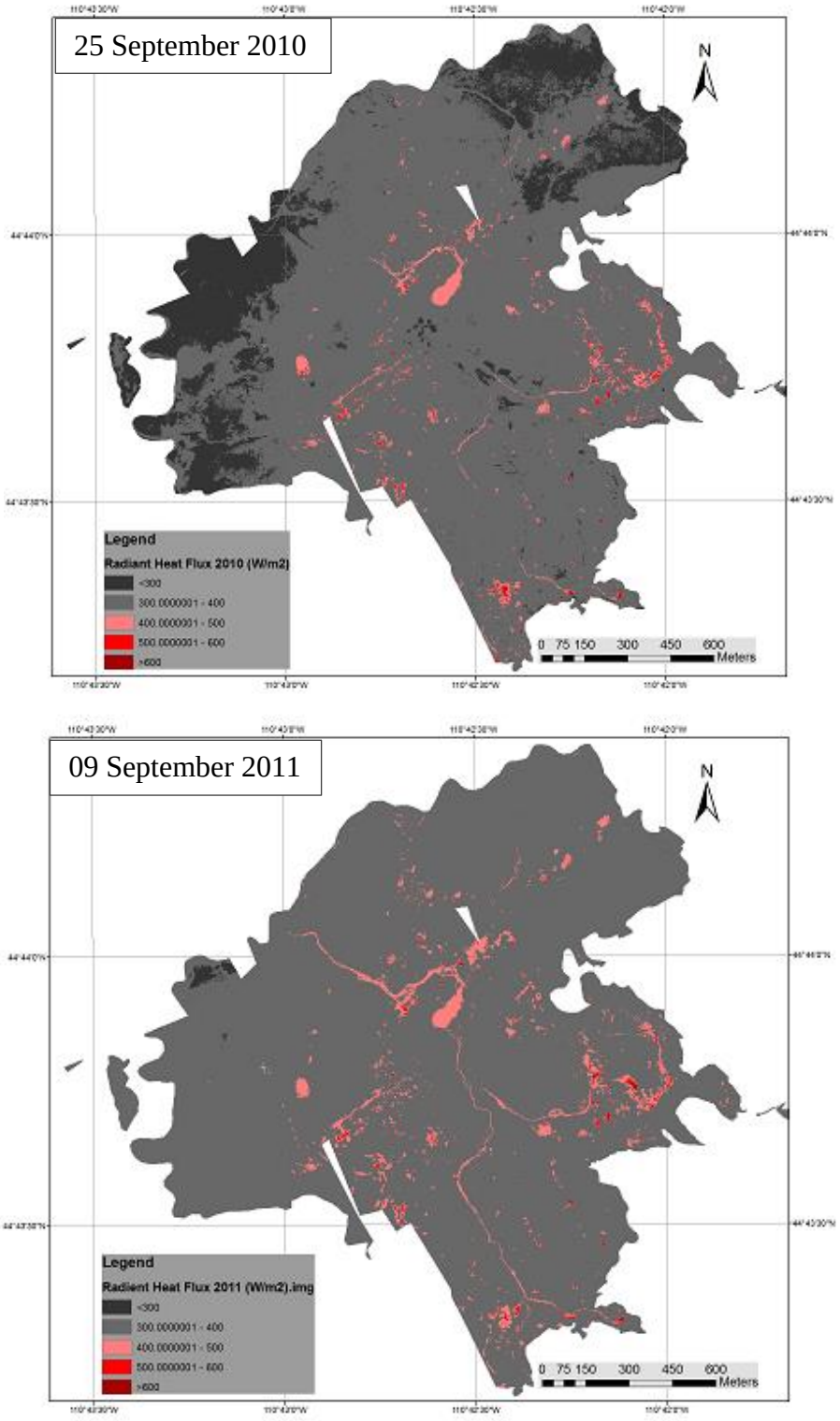

Fig. 4.7. (continued).

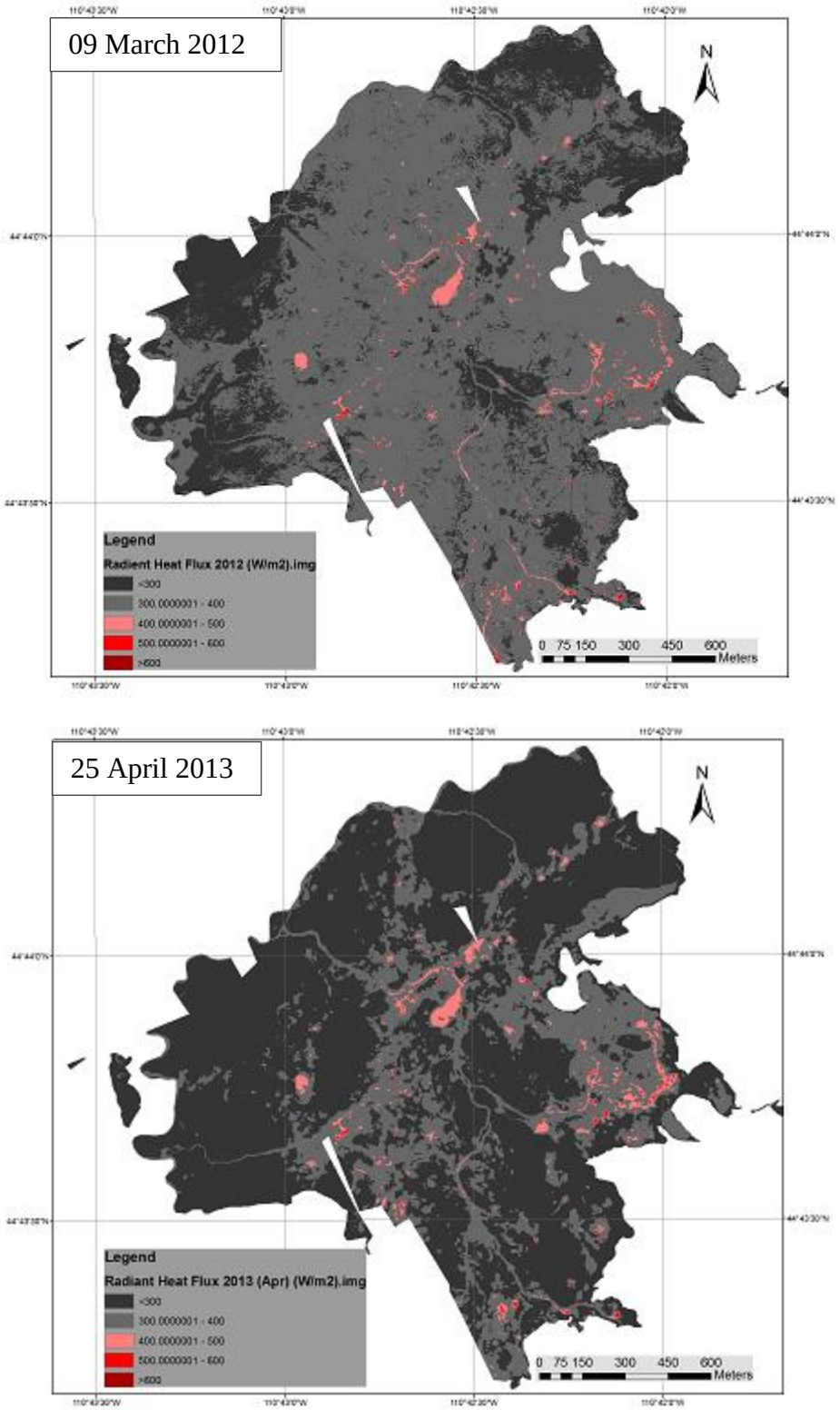

Fig. 4.7. (continued).

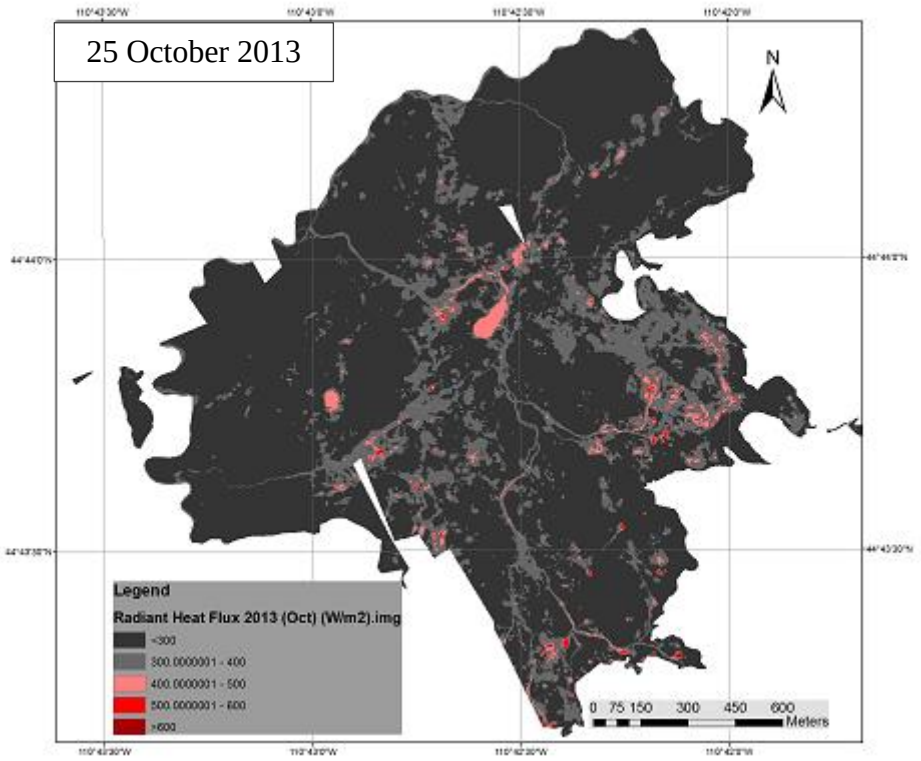

Fig. 4.7. (continued).

campground and museum in 2010 and 2011 images. The area of the hot pixels decreased in 2012 and April 2013 images and increased again in October 2013 image (Fig 4.11). Similarly, hot pixels were observed to be formed in 2009 image in the southern side of the paved trail in Back Basin. The area of the hot pixels was continued to slightly increase until October 2013. Some of the changes observed around the trails in Porcelain Basin and Back Basin have not been aligned with any field observation or official reports from the National Park service about unusual thermal activity around Norris Geyser Basin. However, in mid-June 2011, NGB geologists reported new thermal activity along the Back Basin trail between Yellow Funnel Spring and Porkchop Geyser. They observed burning trees in that area and the change of the color of the ground. The area where the new thermal features were observed in Back Basin is shown in Fig (4.12).

Table 4.5.

Geothermal radiant power estimated for each class after subtracting the radiant power due to stored solar radiation.

Time of Flight	Sinter Soil (gigawatt)	Bare Soil (gigawatt)	Forest (gigawatt)	Grass (gigawatt)	Lakes and Pools (gigawatt)	River (gigawatt)	Total Radiant Heat Power (gigawatt)
12 Sept 2008	0.048	0.019	0.012	0.021	0.002	0.0002	0.1024
10 Sept 2009	0.042	0.017	0.010	0.018	0.002	0.0001	0.0883
25 Sept 2010	0.047	0.019	0.012	0.021	0.002	0.0001	0.1011
09 Sept 2011	0.048	0.021	0.021	0.022	0.002	0.0003	0.1133
09 Mar 2012	0.045	0.018	0.013	0.019	0.003	0.0001	0.0988
25 Apr 2013	0.043	0.017	0.005	0.018	0.003	0.0002	0.0861
25 Oct 2013	0.045	0.017	0.004	0.019	0.002	0.0001	0.0876

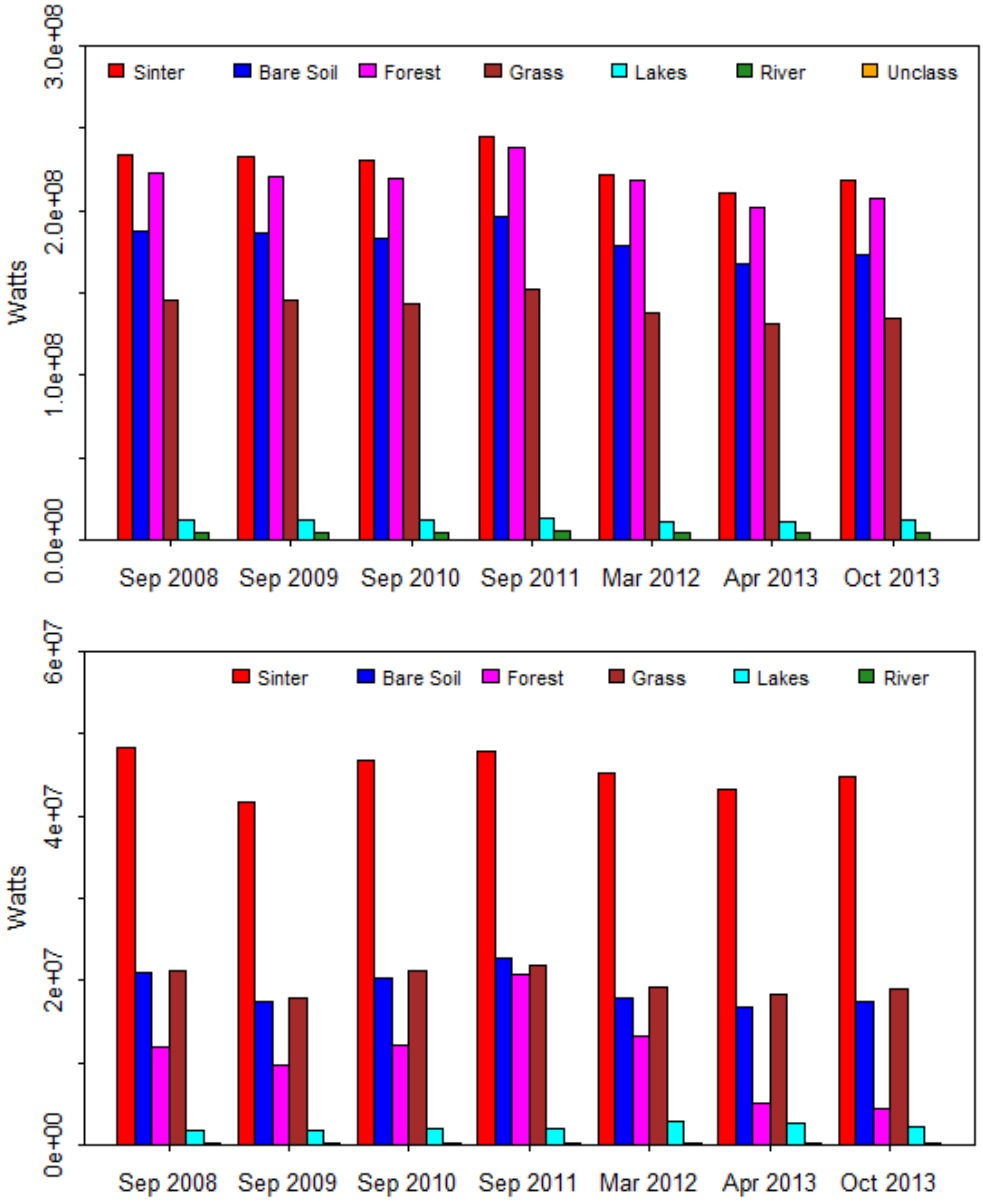

Fig. 4.8. Total radiant power (top) before removing solar effect, and geothermal radiant power (bottom) after removing the radiant power from stored solar radiation.

4.4. Summary and Conclusions

Norris Geyser Basin in Yellowstone National Park is the most dynamic and unrest geyser basin in the Park. The goal of this study was to evaluate and compare the spatial and temporal changes of the geothermal radiant temperature, radiant flux, and radiant

power, at Norris Geyser Basin over several years. The study was supported by high resolution TIR images acquired annually over the basin using consistent processing methods to enable year-to-year comparison of the radiant components. One challenge when temporally comparing the radiant components, was the presence of stored radiant flux from solar shortwave radiation and atmospheric longwave radiation. This flux is variable depending on the season, cloud conditions, and soil moisture. Previous remote sensing studies used the radiant flux from a non-geothermal area as a surrogate for the absorbed radiant flux in the geothermal area. This method required additional remotely sensed images outside the geothermal area, which added to the overall project cost. Selection of a suitable background non-geothermal area is somewhat challenging to select a background area with surface characteristics similar to the geothermal area. Seielstad and Queen (2009) assumed that the heat flux of areas adjacent to, but outside Norris, is representative of background flux in the basin. They estimated weighted mean flux within each land-cover class to produce total flux by a class. However, their method ignored the areas outside Norris with high temperatures that matches or exceeded the temperature of some areas within Norris.

In this chapter, a new method was developed to estimate the stored radiant flux based on solar irradiation estimated for the days of image acquisition. This method assumed clear skies condition given that TIR images were acquired during nights of mostly sunny days. An improvement to the method used by Seielstad and Queen (2009) was suggested by including recommendation by Vaughan et al. (2012) to define the background areas in NGB based on the terrain elevation, aspect, and slope. The radiant

temperature and radiant flux images were consistent and showed that areas covered with siliceous sinter deposit absorbed less heat from the sun due to their high albedo, while areas covered with evergreen Pine and Douglas fir trees had the highest background radiant flux likely due to higher emissivity and storage in these pixels. Results of total radiant power were consistent with previous remote sensing studies before subtracting the solar effect. The study estimated a range of total radiant flux between 0.73 GW estimated from the TIR image acquired on 25 April 2013 and 0.85 GW estimated from the TIR image acquired on 09 September 2011. The radiant geothermal heat flux, after subtracting the radiant effects of solar radiation ranged between 0.086 gigawatts and 0.113 GW. Given the between-acquisition differences in boundary layer moisture, air temperature, and wind speed, on and prior to the acquisitions, the geothermal radiant power values were consistent. This similarity suggests consistency of the methods used for image acquisition and correction and the method suggested in this chapter to estimate the background radiant flux. The observed increase in radiant flux near back Basin trail and close to Porcelain trail during 2009-2011 flights suggested that the methods used for image acquisition and analysis were suitable to study and assess individual hydrothermal features as well as to monitor changes over the entire basin.

Table 4.6.

The area of bare ground and sinter soil (m^2) relevant to different range of radiant flux after removing the stored solar radiant flux.

Radiant Flux (W/m^2)	12 Sept 2008	10 Sept 2009	25 Sept 2010	09 Sept 2011	09 Mar 2012	25 Apr 2013	25 Oct 2013
0-100	1,535,322	1,551,573	1,473,978	1,281,518	1,247,931	1,220,314	1,218,982
100-200	88,428	78,268	87,049	79,013	89,427	86,595	81,990
200-300	5,815	6,451	9,285	6,163	6,506	8,954	6,523
>300	572	881	1,909	1,023	876	1,476	636

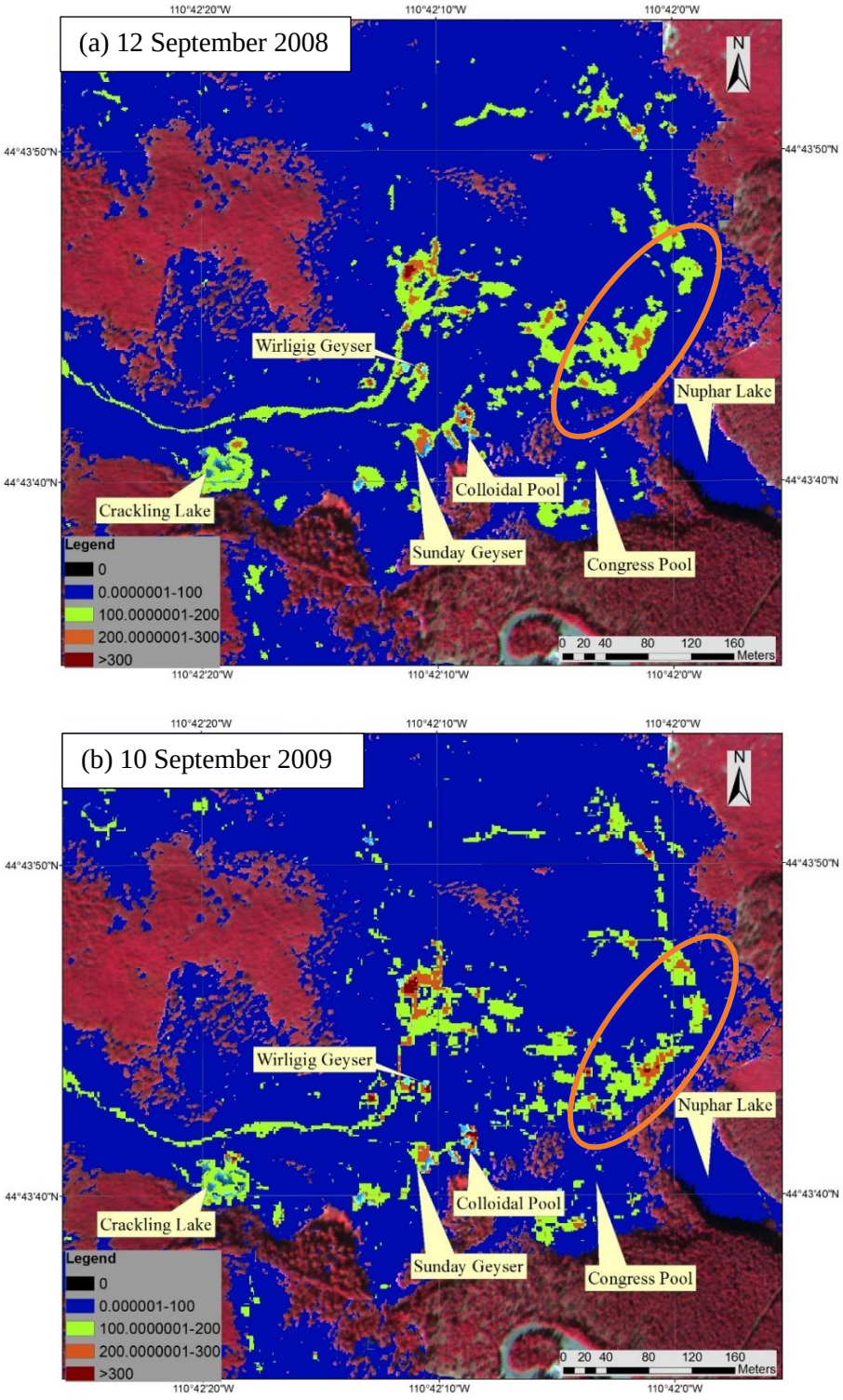

Fig. 4.9. Change in the radiant flux in the east side of Porcelain Basin from 2008 (a), 2009 (b), 2010 (c), 2011 (d), 2012 (e), April 2013 (f), October 2013 (g), Heat flux image overlay an MS image in the red range of spectrum, acquired in 2010.

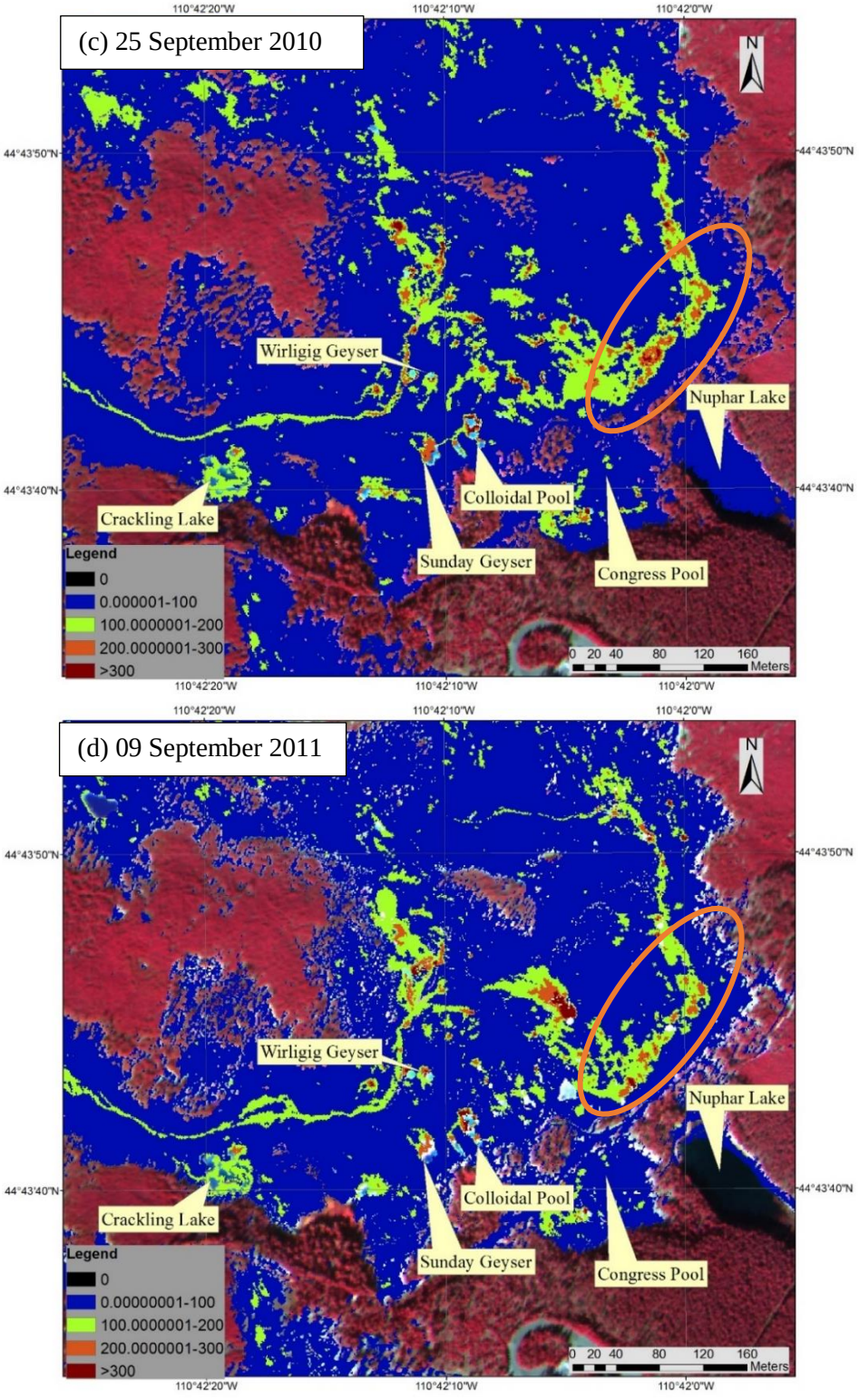

Fig. 4.9. (continued).

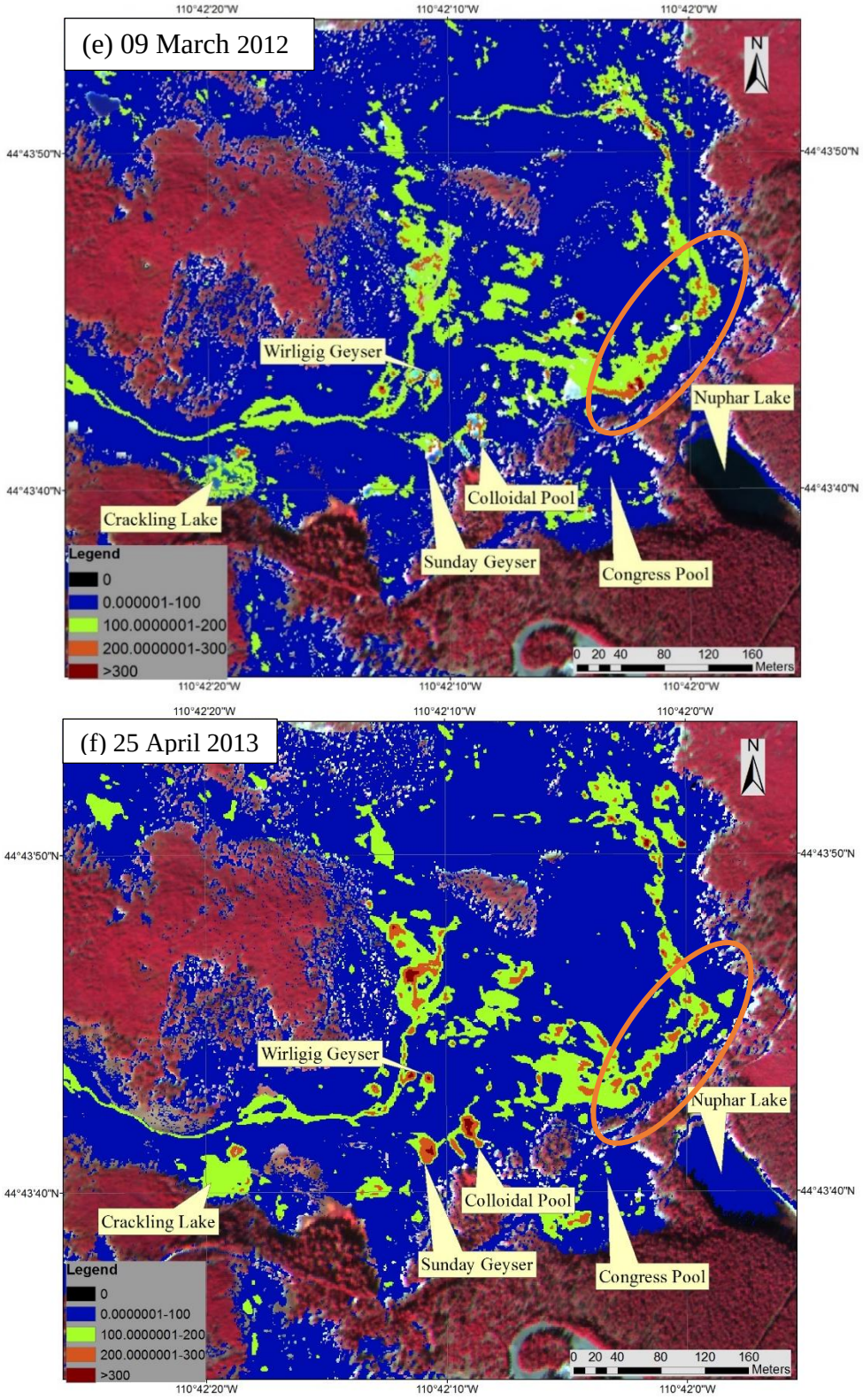

Fig. 4.9. (continued).

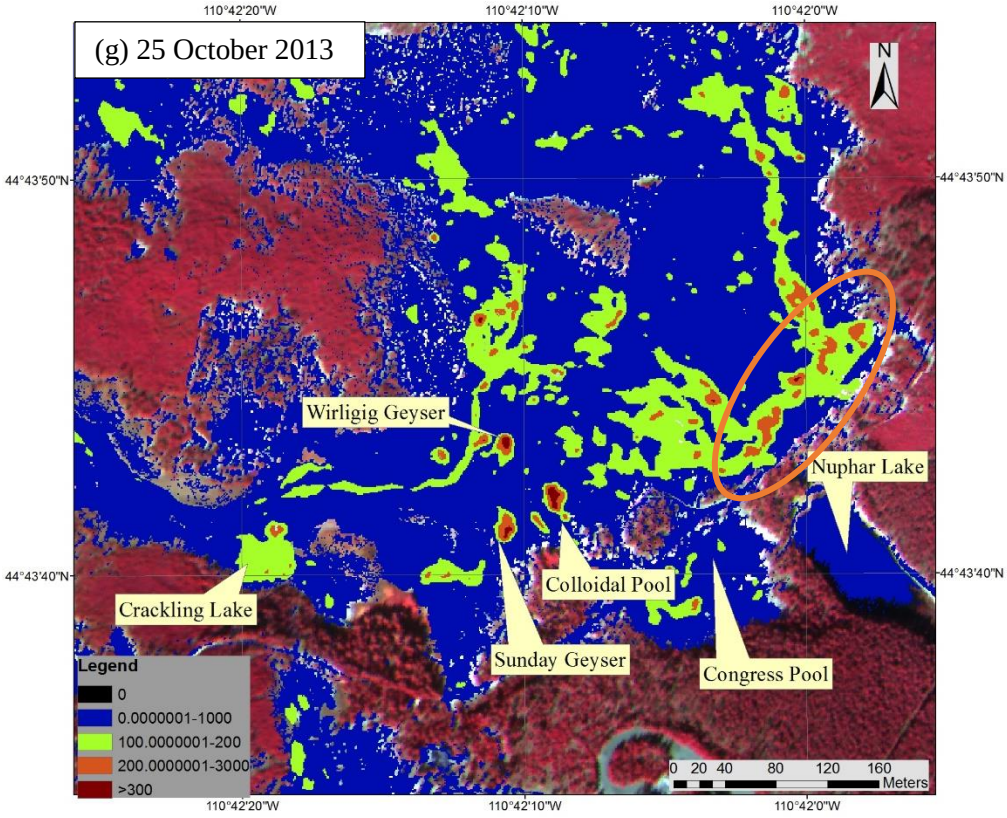

Fig. 4.9. (continued).

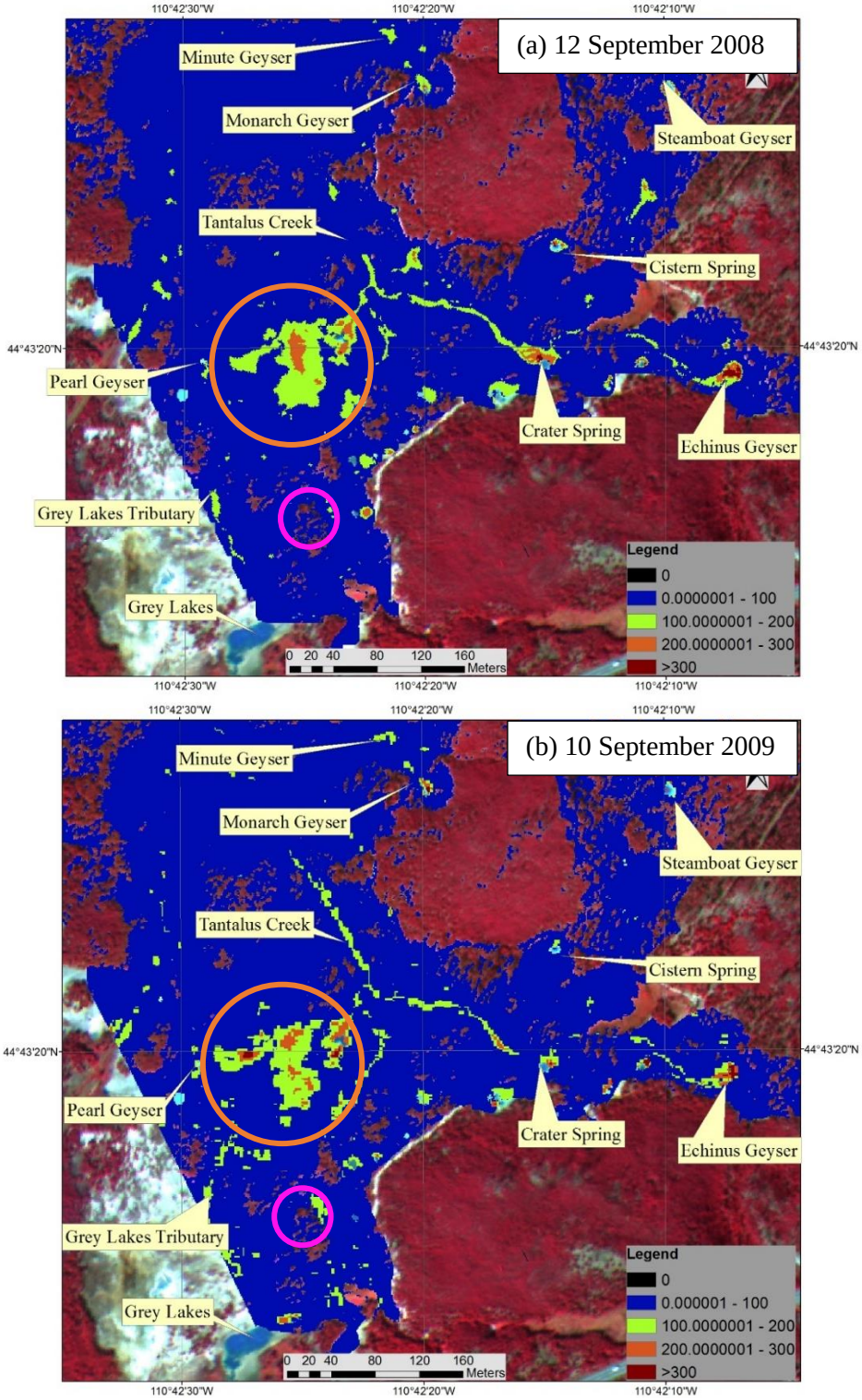

Fig. 4.10. Change in the radiant flux in Back Basin from 2008 (a), 2009 (b), 2010 (c), 2011 (d), 2012 (e), April 2013 (f), October 2013 (g), Heat flux image overlay an MS image in the red range of spectrum, acquired in 2010.

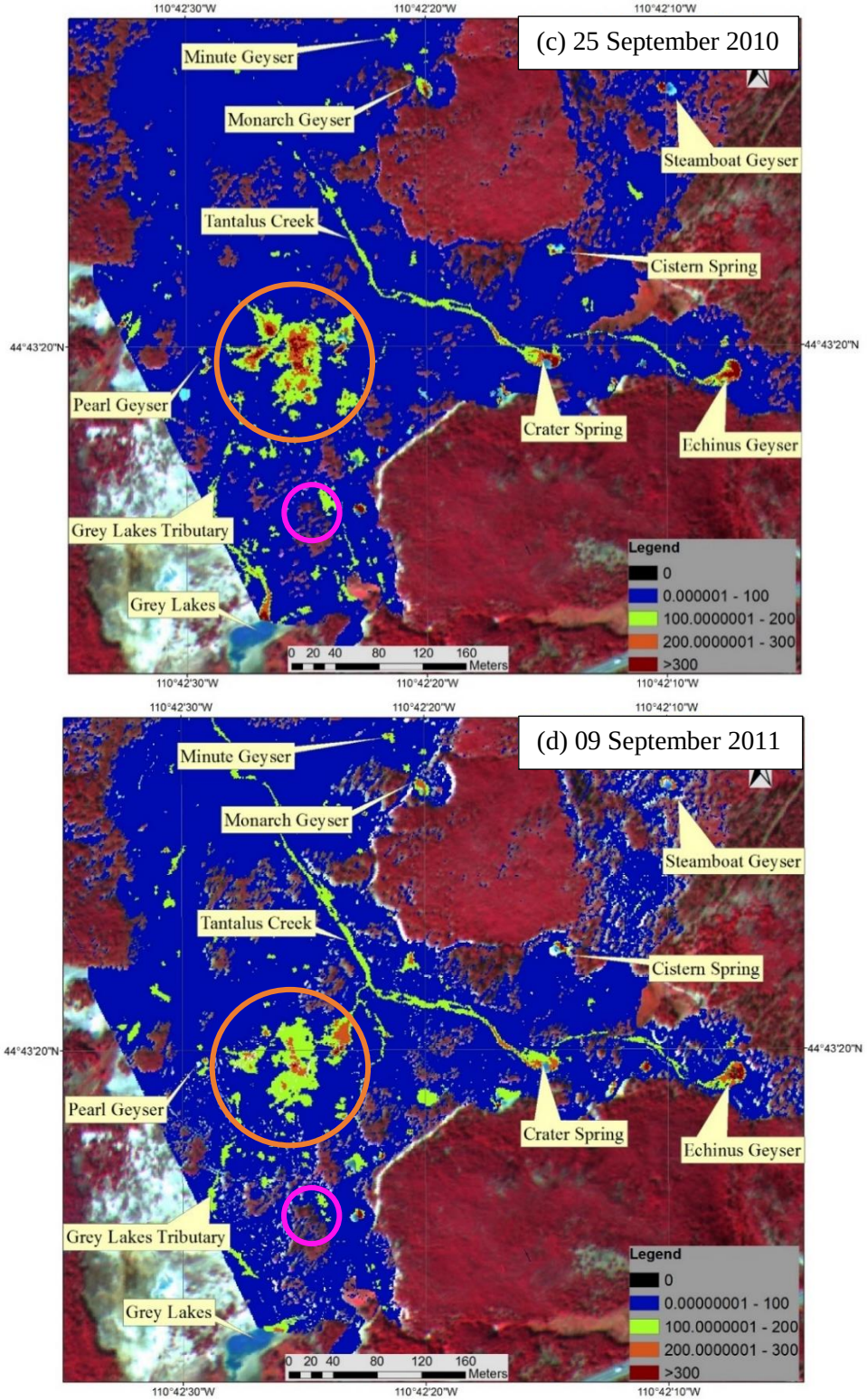

Fig. 4.10. (continued).

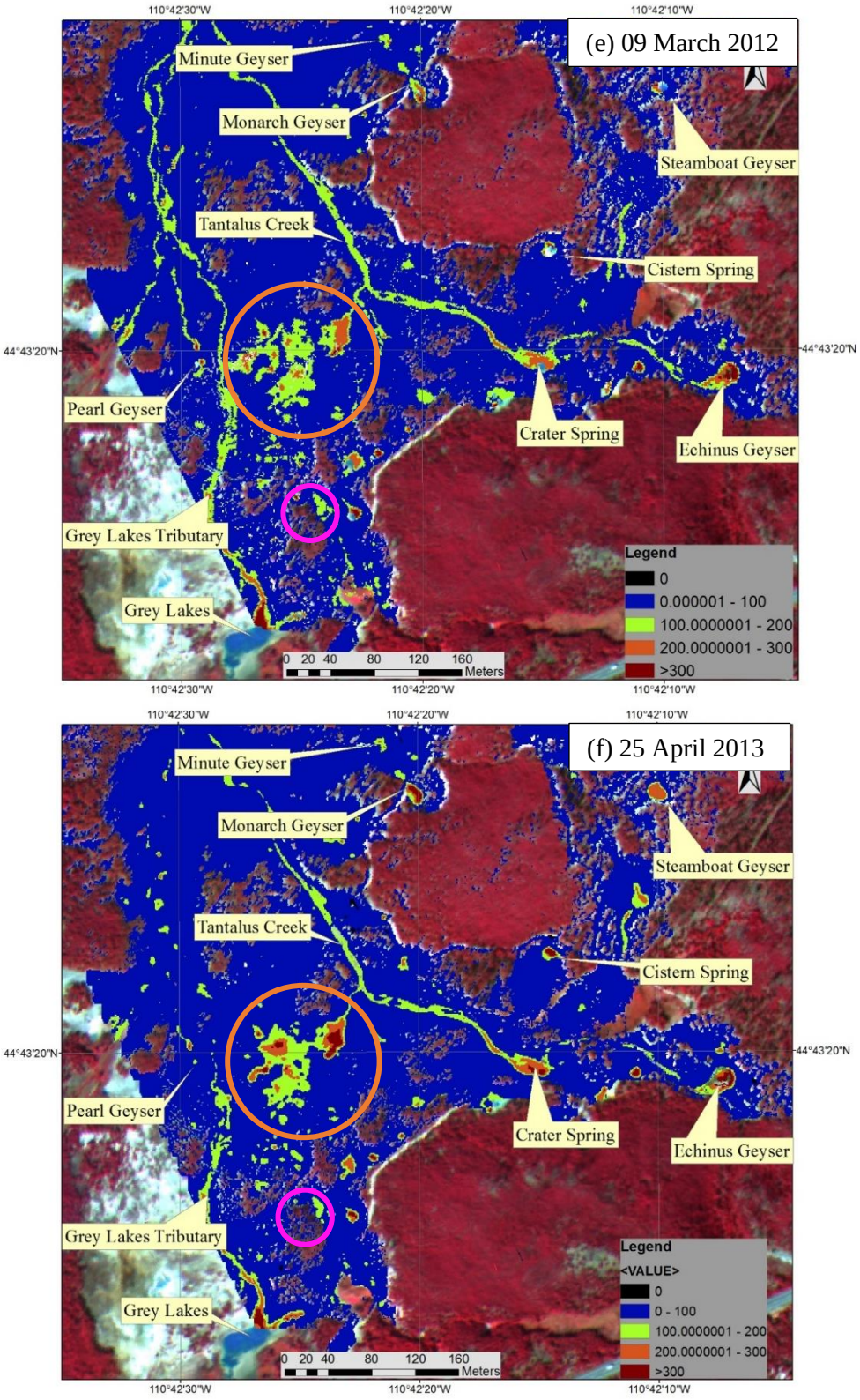

Fig. 4.10. (continued).

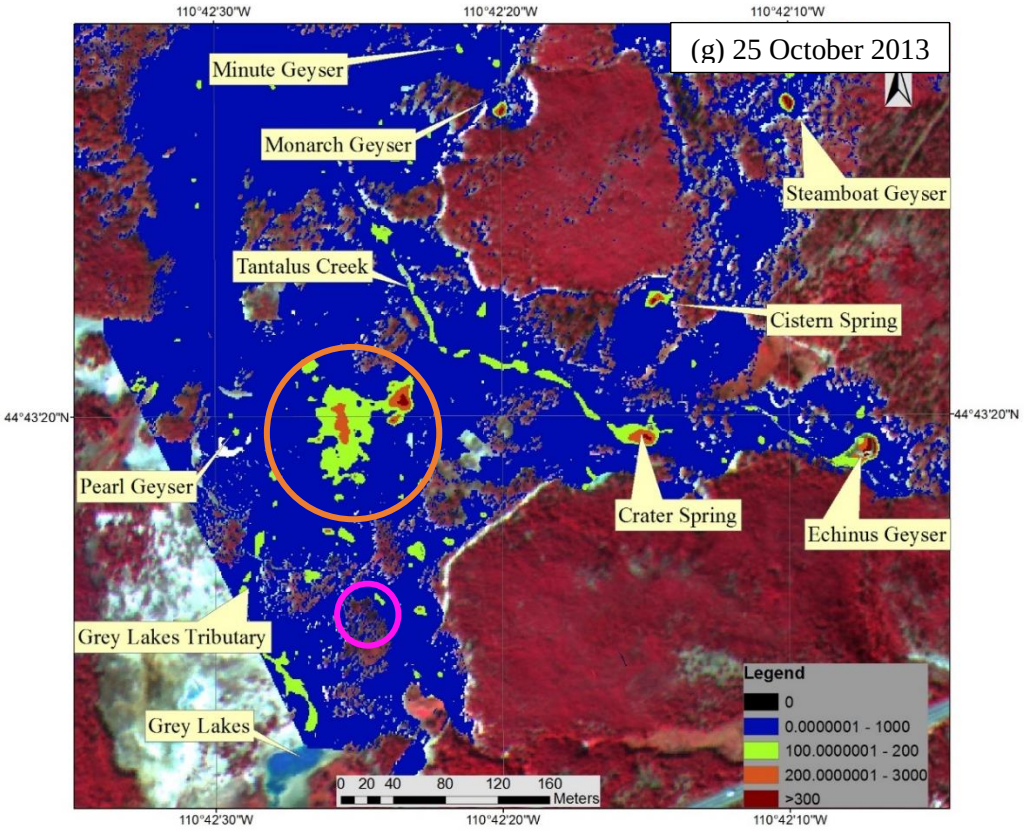

Fig. 4.10. (continued).

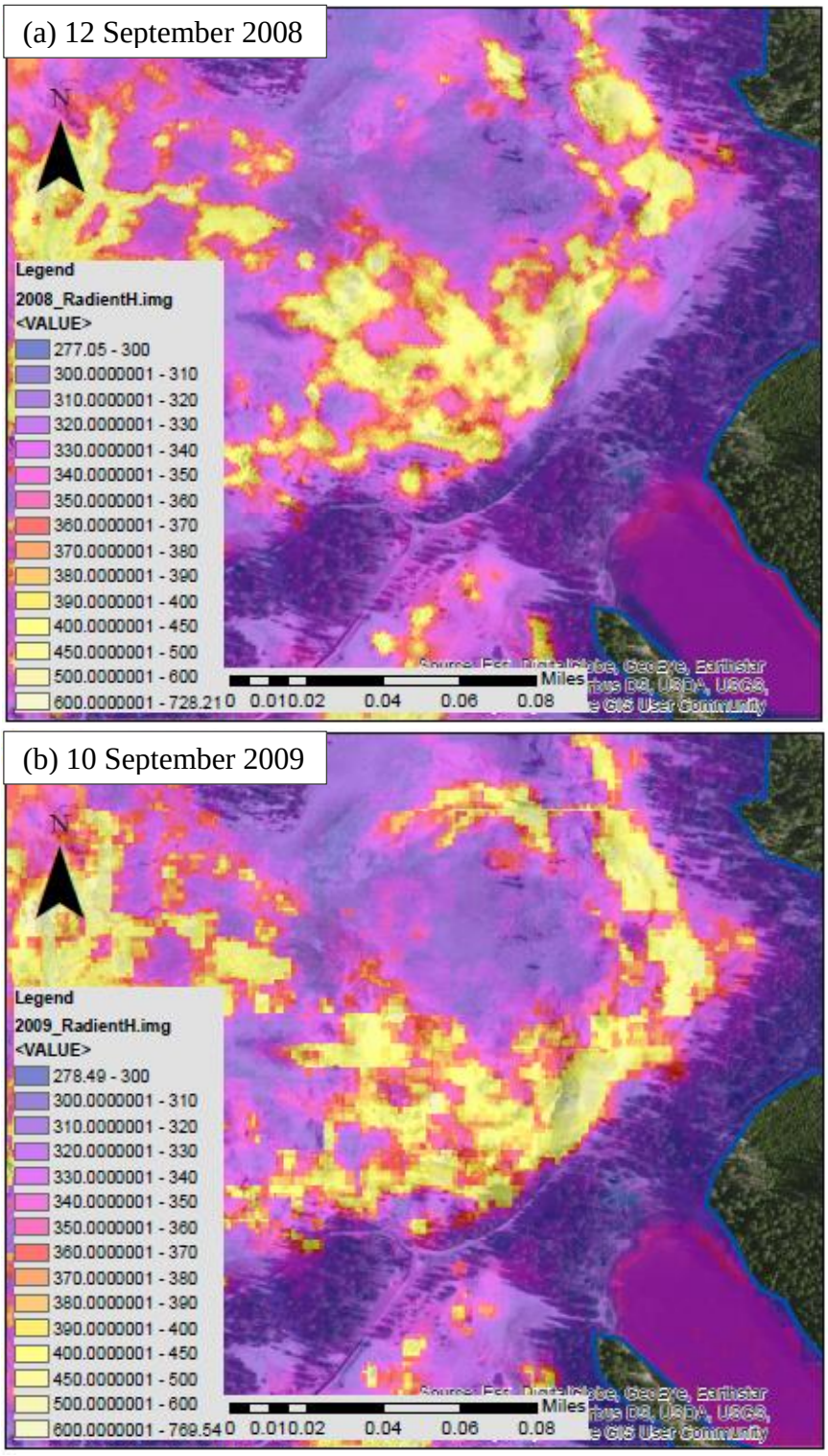

Fig. 4.11. Changes in the radiant flux in the east side of Porcelain Basin on 2008 (a), 2009 (b), 2010 (c), 2011 (d), 2012 (e), April 2013 (f), October 2013 (g), Heat flux image overlay an MS image in the red range of spectrum, acquired in 2010.

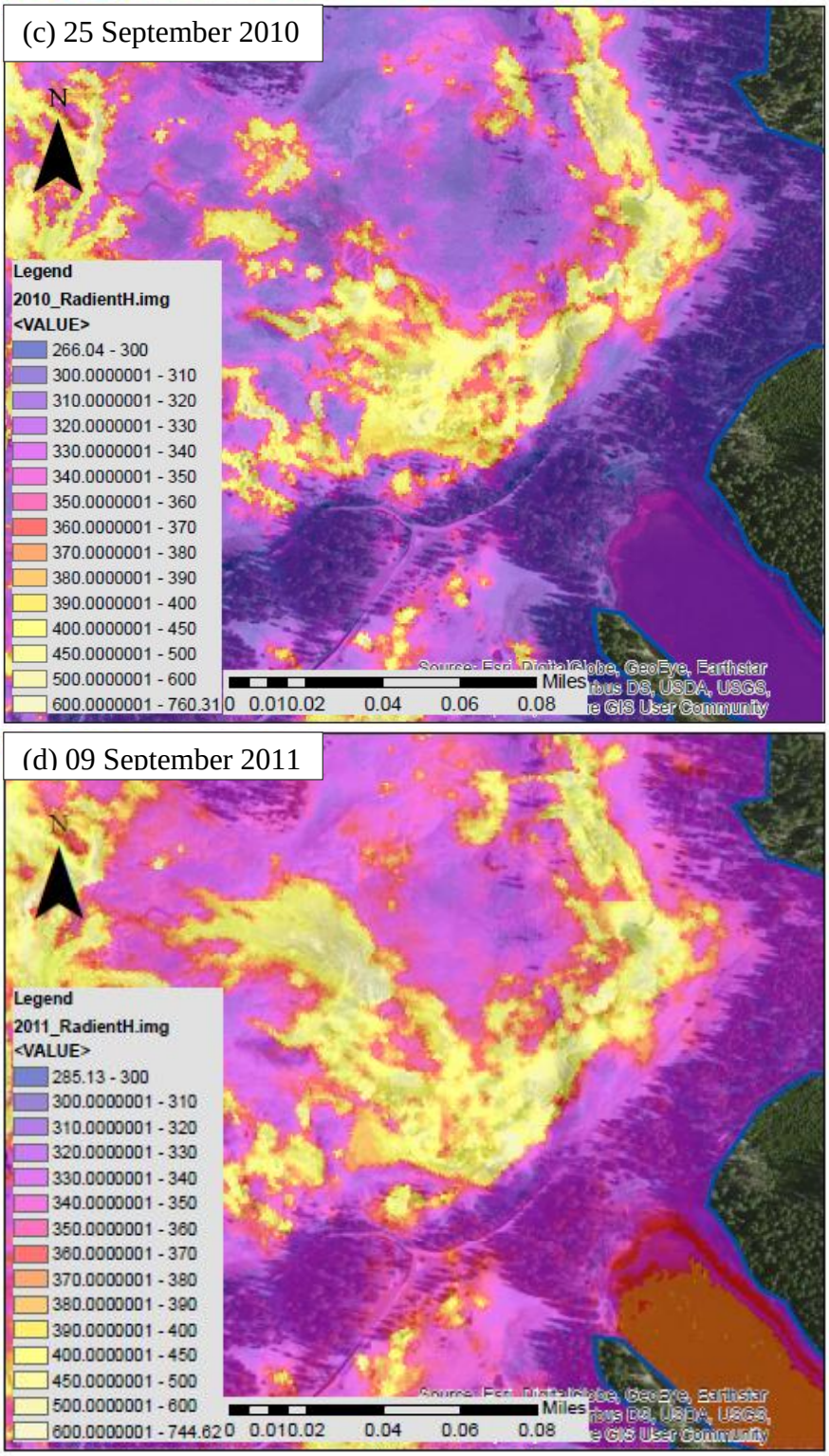

Fig. 4.11. (continued).

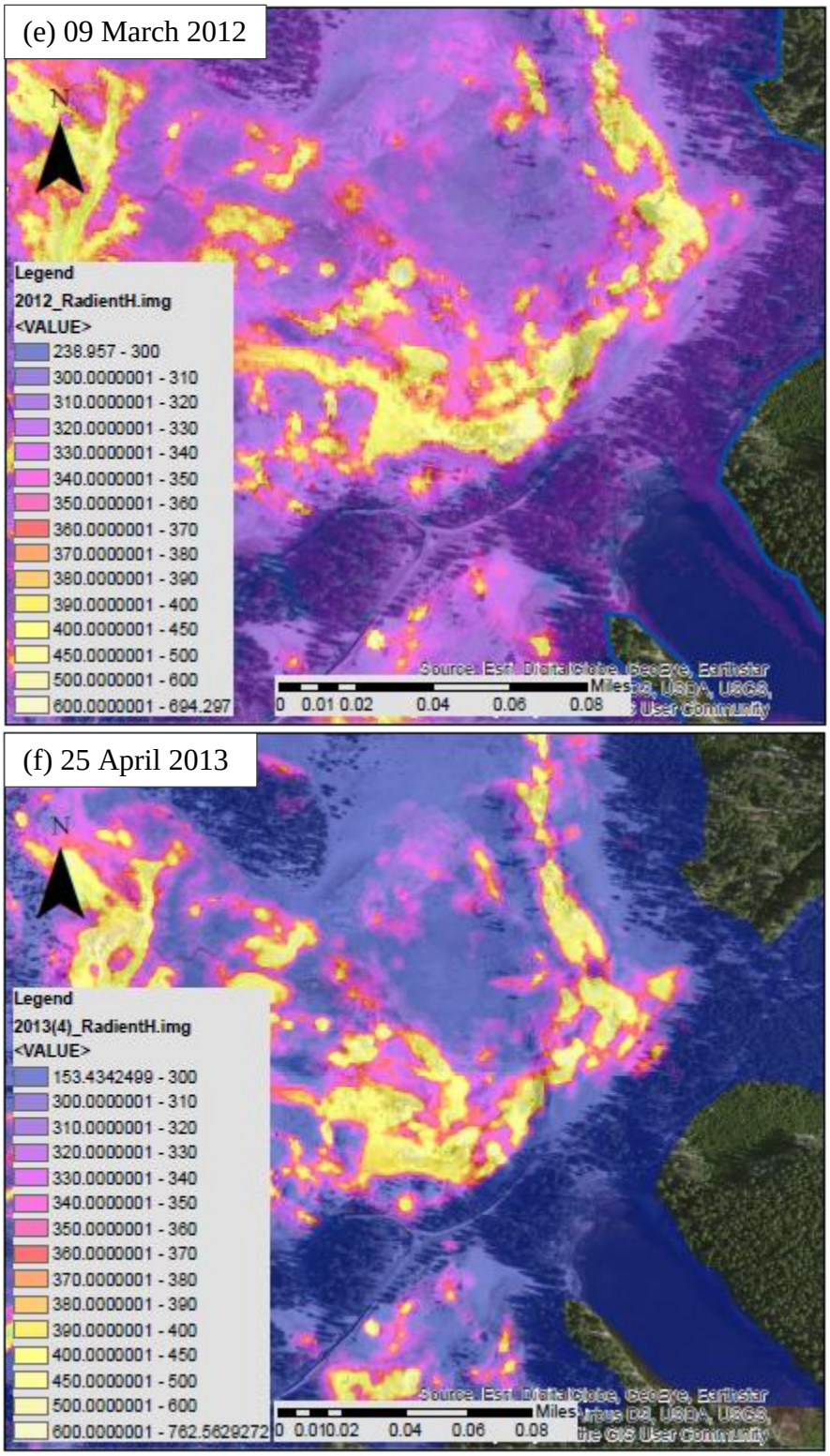

Fig. 4.11. (continued).

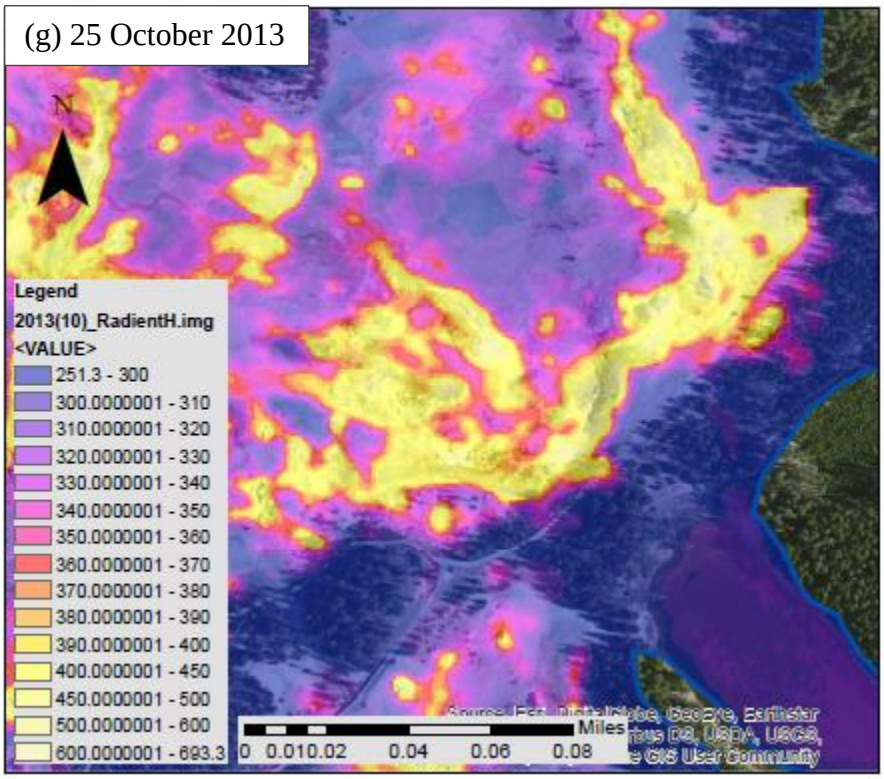

Fig. 4.11. (continued).

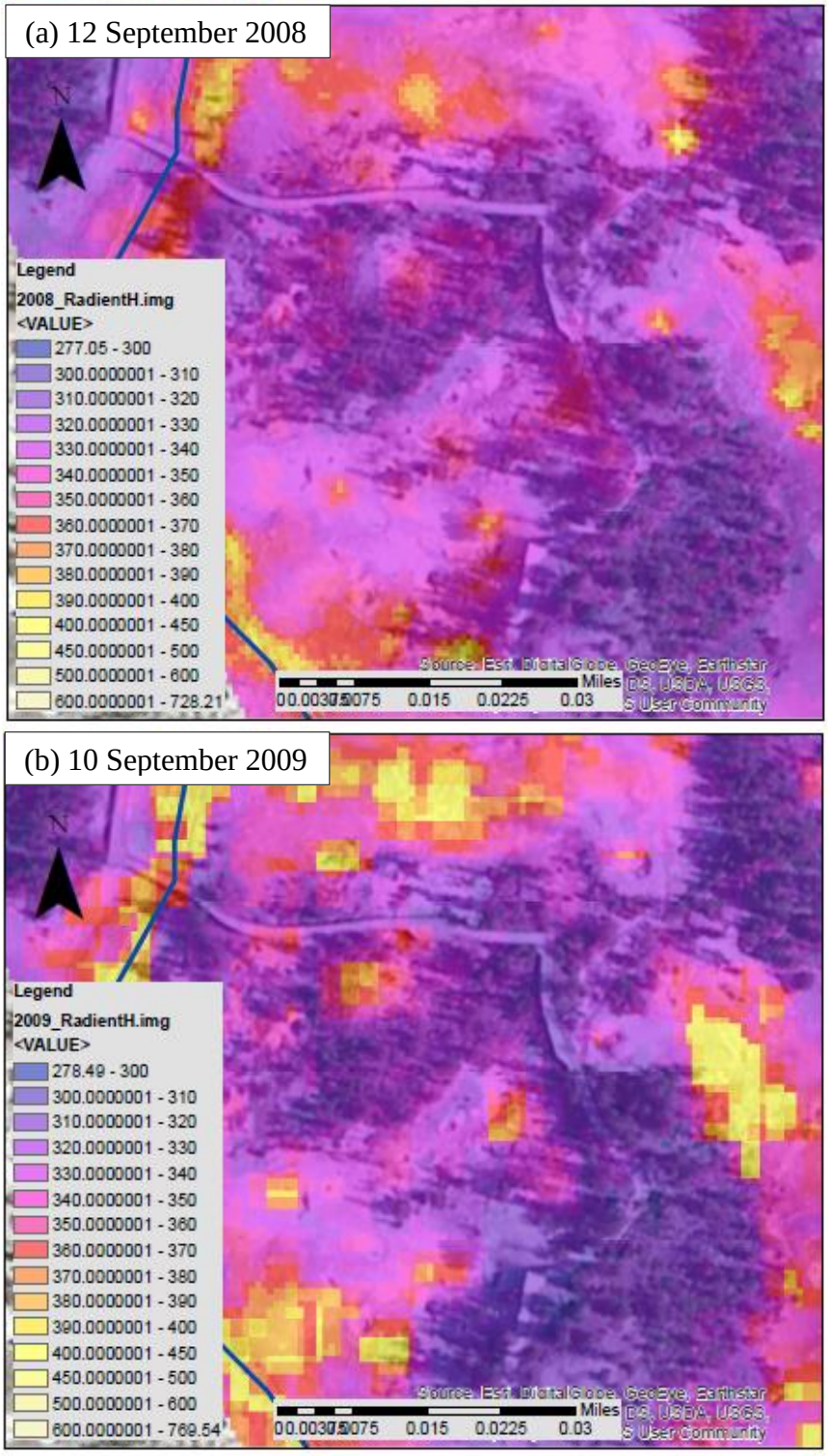

Fig. 4.12. Changes in the radiant flux in Back Basin from 2008 (a), 2009 (b), 2010 (c), 2011 (d), 2012 (e), April 2013 (f), October 2013 (g), Heat flux image overlay an MS image in the red range of spectrum, acquired in 2010.

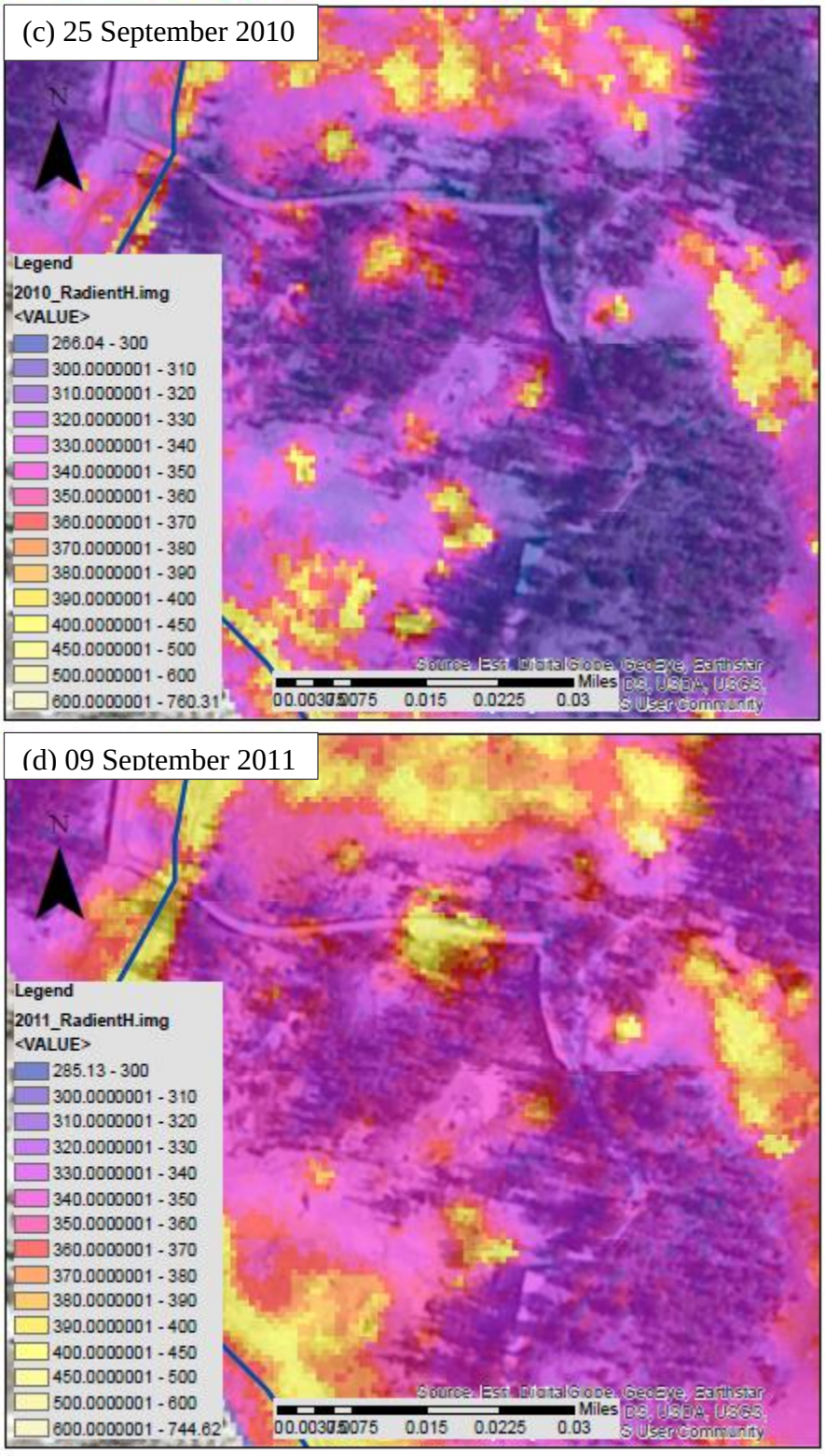

Fig. 4.12. (continued).

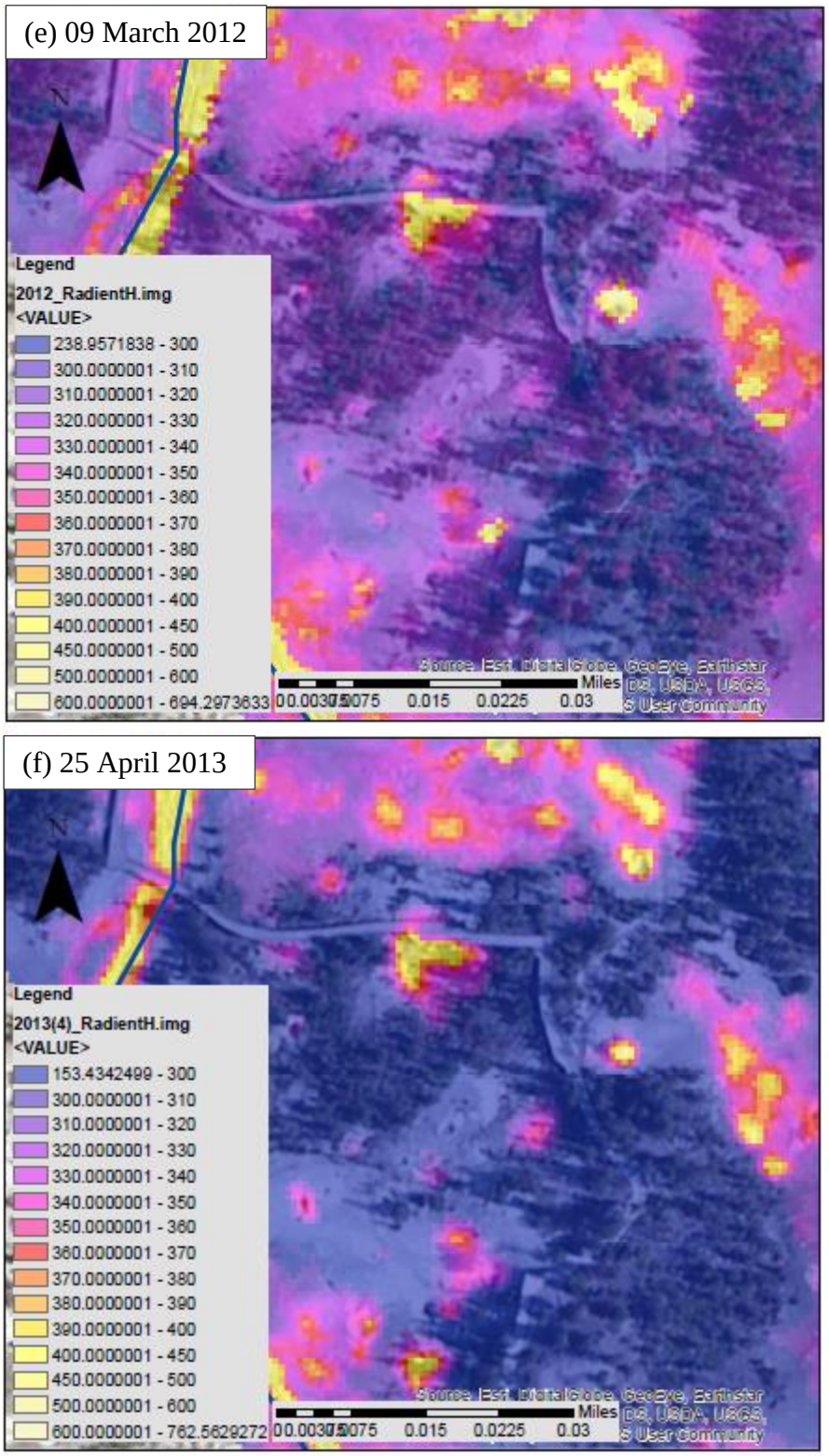

Fig. 4.12. (continued).

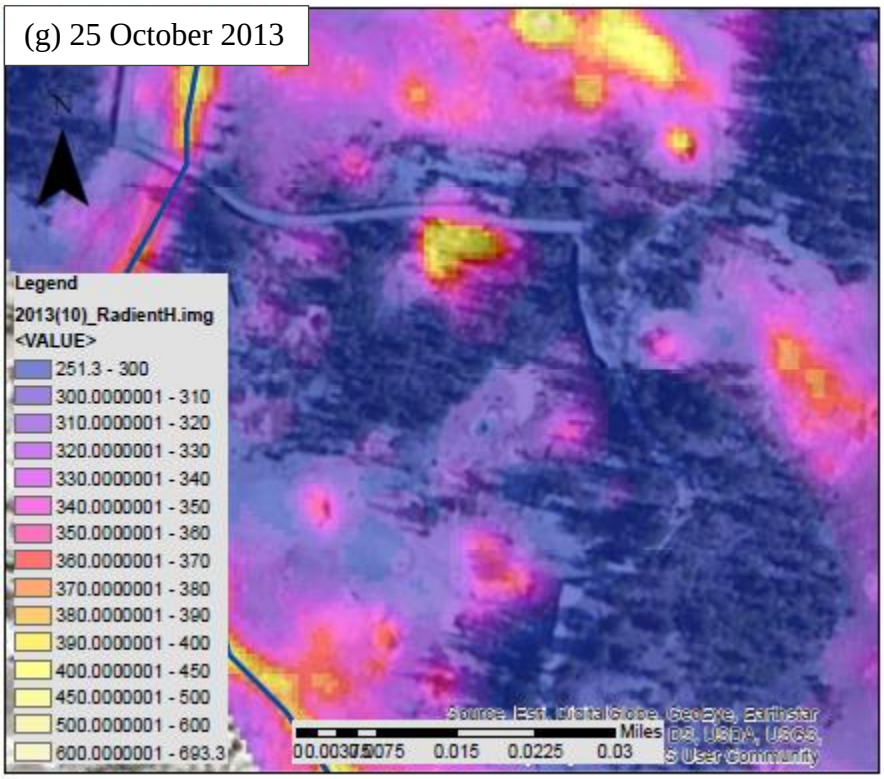

Fig. 4.12. (continued).

References

Ball, J. W., McCleskey, R. B., Nordstrom, D. K., Holloway, J. M., Verplanck, P. L., Sturtevant, S. A., 2002. Water-chemistry data for selected springs, geysers, and streams in Yellowstone National Park, Wyoming, 1999-2000.

Berk, A., Anderson, G. P., Acharya, P. K., Chetwynd, J. H., Bernstein, L. S., Shettle, E. P., Adler-Golden, S. M., 1999. MODTRAN4 user's manual. Air Force Research Laboratory, Space Vehicles Directorate, 1-5.

Brunsell, N. A., Gillies, R. R., 2002. Incorporating surface emissivity into a thermal atmospheric correction. Photogrammetric engineering and remote sensing, 68(12), 1263-1270.

Clor, L. E., McCleskey, R. B., Huebner, M. A., Lowenstern, J. B., Heasler, H. P., Mahony, D. L., Evans, W. C., 2012. Water Chemistry and Electrical Conductivity Database for Rivers in Yellowstone National Park, Wyoming. US Geol. Surv. Data Series, 632, 18.

Fournier, R. O., Weltman, U., Counce, D., White, L. D., Janik, C. J., 2002. Results of weekly chemical and isotopic monitoring of selected springs in Norris Geyser Basin, Yellowstone National Park during June-September, 1995: US Geological Survey.

Fournier, R. O., White, D. E., Truesdell, A. H., 1976. Convective heat flow in Yellowstone National Park.

Friedman, I., Norton, D. R., 2007. Is Yellowstone Losing Its Steam?—Chloride Flux out of Yellowstone National Park.

Guide, E. F., 2008. ERDAS field guide. ERDAS software. ERDAS Inc. Georgia. USA.

Hardy, C. C., 2005. Characterizing thermal features from multi-spectral remote sensing data using dynamic calibration procedures.

Haselwimmer, C., Prakash, A., 2013. Thermal infrared remote sensing of geothermal systems Thermal Infrared Remote Sensing (pp. 453-473): Springer.

Haselwimmer, C. E., Prakash, A., Holdmann, G., 2011. Geothermal exploration at Pilgrim Hot Springs, Alaska using airborne thermal infrared remote sensing.

Heasler, H. P., Jaworowski, C., Foley, D., 2009. Geothermal systems and monitoring hydrothermal features. Geological Monitoring, 105-140.

Hurwitz, S., Harris, R. N., Werner, C. A., Murphy, F., 2012. Heat flow in vapor dominated areas of the Yellowstone Plateau Volcanic Field: Implications for the thermal budget of the Yellowstone Caldera. Journal of Geophysical Research: Solid Earth (1978–2012), 117(B10).

Jaworowski, C., Heasler, H., Neale, C., Saravanan, S., Masih, A., 2013. Temporal and seasonal variations of the Hot Spring Basin hydrothermal system, Yellowstone National Park, USA. Remote Sensing, 5(12), 6587-6610.

Kasten, F., 1996. The Linke turbidity factor based on improved values of the integral Rayleigh optical thickness. Solar energy, 56(3), 239-244.

Neale, C. M. U., Sivarajan, S., Masih, A., Jaworowski, C., Heasler, H., 2011. Estimating heat flow of thermal features in Yellowstone National Park using airborne thermal infrared remote sensing.

Neale, C. M. U., Jaworowski, C., Heasler, H., Sivarajan, S., Masih, A., 2016. Hydrothermal monitoring in Yellowstone National Park using airborne thermal infrared remote sensing. Remote Sensing of Environment, 184, 628-644.

Savage, S. L., Lawrence, R. L., Custer, S. G., Jewett, J. T., Powell, S. L., Shaw, J. A., 2010. Review of alternative methods for estimating terrestrial emittance and geothermal heat flux for Yellowstone National Park using landsat imagery. GIScience & Remote Sensing, 47(4), 460-479.

Seielstad, C., Queen, L., 2009. Thermal Remote Monitoring of the Norris Geyser Basin, Yellowstone National Park. Final Report for the National Park Service Cooperative Ecosystem Studies Unit, Agreement(H1200040001), 38.

Team, G. D., 2016. Geographic Resources Analysis Support System (GRASS), GNU General Public License. Retrieved from http://grass.osgeo.org

Vaughan, R. G., Hook, S. J., Calvin, W. M., Taranik, J. V., 2005. Surface mineral mapping at Steamboat Springs, Nevada, USA, with multi-wavelength thermal infrared images. Remote Sensing of Environment, 99(1), 140-158.

Vaughan, R. G., Keszthelyi, L. P., Lowenstern, J. B., Jaworowski, C., Heasler, H., 2012. Use of ASTER and MODIS thermal infrared data to quantify heat flow and hydrothermal change at Yellowstone National Park. Journal of Volcanology and Geothermal Research, 233, 72-89.

Vaughan, R. G., Lowenstern, J. B., Keszthelyi, L. P., Jaworowski, C., Heasler, H., 2012. Mapping Temperature and Radiant Geothermal Heat Flux Anomalies in the Yellowstone Geothermal System Using ASTER Thermal Infrared Data. Geothermal Resources Council Transactions, 36, 1403-1409.

Watson, F. G. R., Lockwood, R. E., Newman, W. B., Anderson, T. N., Garrott, R. A., 2008. Development and comparison of Landsat radiometric and snowpack model inversion techniques for estimating geothermal heat flux. Remote Sensing of Environment, 112(2), 471-481.

White, D. E., Hutchinson, R. A., Keith, T. E. C., 1988. Geology and remarkable thermal activity of Norris Geyser Basin, Yellowstone National Park, Wyoming. US Geol. Surv., Prof. Pap.;(United States), 75(1456).

CHAPTER 5

SUMMARY, CONCLUSIONS, AND RECOMMENDATIONS

Summary and Conclusions

This dissertation described research conducted towards estimating geothermal heat flux from airborne thermal infrared remote sensing in Norris Geyser Basin, Yellowstone National Park. Similar previous studies including Jaworowski et al. (2013) and Haselwimmer and Prakash (2013), stated the importance of subtracting the residual heat flux stored in the ground from solar shortwave and/or atmospheric longwave radiations from the total radiant flux to estimate the geothermal heat flux. In Chapter 2, a comparison method was suggested to compare ground heat flux measured during selected sunny summer days and overcast winter days with low incoming solar radiation, to estimate the solar radiation absorption effects. This method assumed that the geothermal heat flux was constant during the days used for the comparison. The method also assumed that latent heat and sensible heat were not significant heat sources in the study area and that the main sources of heat in the ground were solar radiation and geothermal heat, neglecting the contribution from atmospheric longwave radiation during sunny and clear conditions. However, the results suggested a minimum value of radiant geothermal heat flux for 09 September 2009 acquisition as 255.03 $W \cdot m^{-2}$ and for 09 March 2011 acquisition as 209.08 $W \cdot m^{-2}$. Given the variability of weather conditions on and prior to image acquisition, these values were considered fairly similar. It was not possible to decide if the difference in these values were due to only differences in weather conditions

or if the underling geothermal heat source contributed to some differences. The variability of the estimated fluxes suggested further measurements of the ground heat flux and/or the temperature profile below the diurnal zone to better quantify changes related to the geothermal source.

A one dimensional numerical model was used in Chapter 3 of this dissertation to estimate the contribution of the four different heat flux mechanisms (i.e. conduction of sensible heat, convection of sensible heat by liquid water and water vapor, and convection of latent heat by water vapor) in the study site in NGB. The study was done to test the null hypothesis assumed in Chapter 2 that latent heat and sensible heat were neglected in the study site due to high ground temperatures compared to air temperatures. The results failed to reject that null hypothesis and concluded that the conductive heat flux contributed to more than 99% of the total heat flux in the ground. The chapter also presented the optimization results of some hydraulic and thermal properties of the siliceous sinter deposit, which were poorly understood. The grain size distribution analysis of a sample of siliceous sinter from the study side classified the deposit as sandy clay loam. The results from the inverse solution conducted through HYDRUS-1D matched the grain size distribution and estimated values of n, α, and Ks that were in between the literature range of sandy clay loam and sandy loam (Simunek et al., 2005). However, the measured thermal conductivity of the deposit was higher than sand with 0.4 porosity as estimated by Chung and Horton (1987) due to the presence of silica in the deposit. The results of the optimization have increased our understanding of the hydraulic

characteristics of the siliceous sinter deposit at different water content and temperature conditions.

In Chapter 4 of the dissertation, the acquired high-resolution TIR images were used to study the spatial and temporal radiant flux in NGB. The accuracy and precision of the TIR images ensured reliable estimates of radiant flux compared to the previous Seielstad and Queen (2009) study. The chapter a method was suggested to estimate the contributions to the radiant flux resulting from absorbed solar radiation based on the surface class and the time of image acquisition (summer versus winter and spring). For areas that were covered by bare soil or siliceous sinter deposit, the method assumed that the solar effect is a function of the aspect and slope of the area. The method suggested using the solar beam irradiance at each aspect and slope to estimate the temperature of that area by comparison with the temperature of a flat background area, with minimum or no geothermal heat contribution. The resulting total radiant power ranged between 0.73 gigawatts and 0.85 gigawatts. The 0.85 gigawatts was consistent with the value estimated by Seielstad and Queen (2009). The range of radiant geothermal heat flux, after subtracting the radiant effects of solar radiation varied between 0.086 gigawatts and 0.113 gigawatts. This range is considered consistent given the differences in weather conditions on and prior to the acquisition date.

The study showed that the methods used for image acquisition and analysis were suitable to study and assess individual hydrothermal features as well as monitor changes

over the entire basin. Most thermal disturbances in volcanic systems inhere signs of change long before the change occur. Example to that is increase in seismic signals preceding an earthquake. Year-to year monitoring of the area may depict some of these signs giving the chance for decision makers to take informative reactions. The repeated high-spatial-resolution monitoring may solve the major concern about public and property safety and the safety of the park service personnel and researchers, who come into a close contact with hydrothermal areas in the park.

Recommendations

In Chapter 2 of the dissertation, the calorimetric heat storage method was used to estimate the ground heat flux at the surface from measurements the soil heat flux at 15 cm and the heat storage in the soil above the measurement point. The error expected from using values of temperature and thermal conductivity only at the middle of the soil layer above the plate can range between 3% and 10%. This error can have implications on the estimated ground heat flux at the surface and in the final estimate of residual heat flux. To improve the results from the calorimetric method, multiple measurements of soil temperature and thermal properties at different depths of the soil profile are suggested.

To better quantify changes related to the geothermal source, and to test the proposed method to estimated the geothermal heat flux at the surface, it is recommended to install the heat flux plate and thermocouples at a depth below the diurnal surface radiant flux zone to measure geothermal heat flux. Given the objectives of the study, it

would also seem desirable to have multiple measurements of heat flux plates to help understand some of the observed anomalies following precipitation events and to avoid loss of data possible due to a single plate dysfunction. Perhaps more data on temperature and water content vertical profile in deeper layers and hydraulic properties above and below the plate in periods after precipitation are important to make further discussion about this issue.

An uncertainty is expected from using ASTER emissivity image with approximately 100-meter spatial resolution, to estimate ground emissivity. The error in ground skin temperature for a range of surface emissivity between 0.86 and 0.89 was about 2.67 °C. This error may have implication on determining the temperature gradient in the soil and therefore *Gs* values during time with $+\Delta T$. Alternatively, measuring ground emissivity is recommended for accurate estimate the ground skin temperature.

The suggested atmospheric correction method explained in Chapter 4 has improved the accuracy of the radiometric temperature of cooler water systems. However, the bias remained still in the radiometric temperature of hot water systems due to the cloud of water vapor above these hot systems. The results from Neale et al. (2016) showed the relevant kinetic temperature of six pools in YNP had agreed well with the radiometric temperature for water pools with temperatures less than 35 °C (mean bias error of -1.8 °C and RMSD value of 3.3 °C); however, the mean bias error for water pools with kinetic temperatures greater than 35 °C was 16.8 °C and RMSD was -19.1 °C.

More research studies on removing the vapor effect from the radiometric thermal infrared imagery is encouraged.

References

Chung, S. O., Horton, R., 1987. Soil heat and water flow with a partial surface mulch. Water Resources Research, 23(12), 2175-2186.

Haselwimmer, C., Prakash, A., 2013. Thermal infrared remote sensing of geothermal systems Thermal Infrared Remote Sensing (pp. 453-473): Springer.

Jaworowski, C., Heasler, H., Neale, C., Saravanan, S., Masih, A., 2013. Temporal and seasonal variations of the Hot Spring Basin hydrothermal system, Yellowstone National Park, USA. Remote Sensing, 5(12), 6587-6610.

Seielstad, C., Queen, L., 2009. Thermal Remote Monitoring of the Norris Geyser Basin, Yellowstone National Park. Final Report for the National Park Service Cooperative Ecosystem Studies Unit, Agreement(H1200040001), 38.

Simunek, J., Van Genuchten, M. T., Sejna, M., 2005. The HYDRUS-1D software package for simulating the one-dimensional movement of water, heat, and multiple solutes in variably-saturated media. University of California-Riverside Research Reports, 3, 1-240.

APPENDICES

APPENDIX A – Raw Data

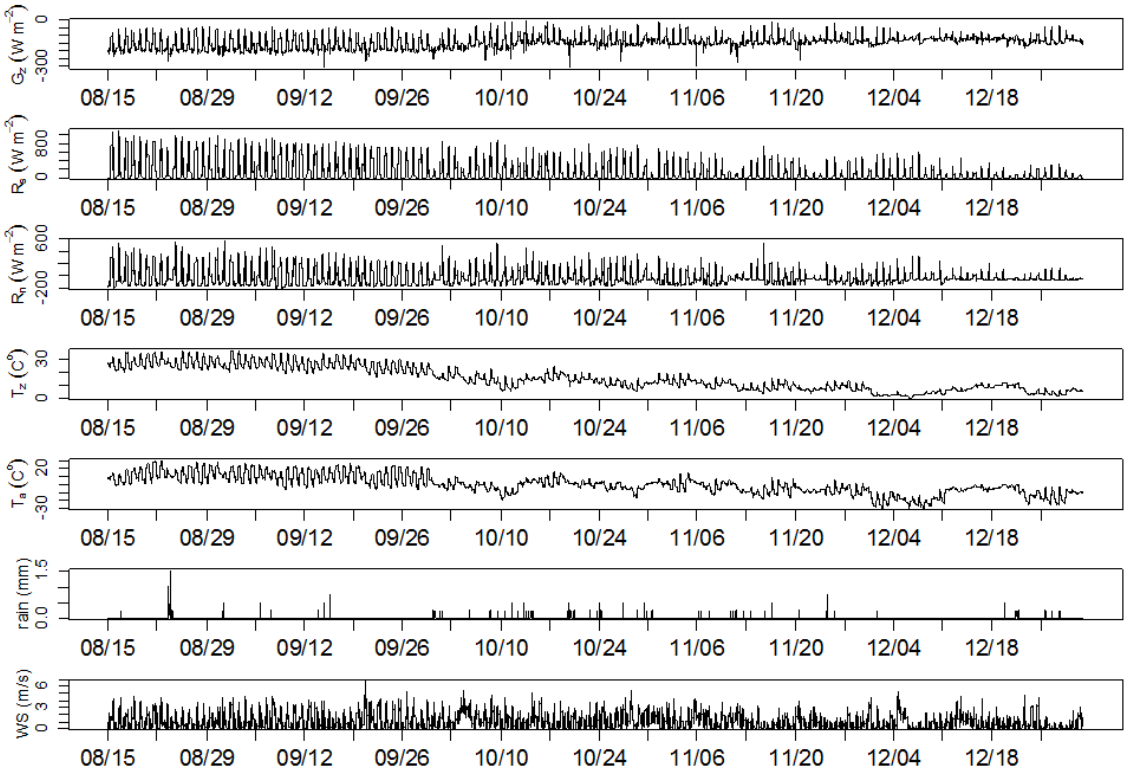

Fig. A.1 Plot showing raw data collected at CR3000 site during 2009, including ground heat flux (G_z), incoming solar radiation (R_s), net radiation (R_n), soil temperature at 0.05 m (T_z), air temperature (T_a), rain, and wind speed (WS).

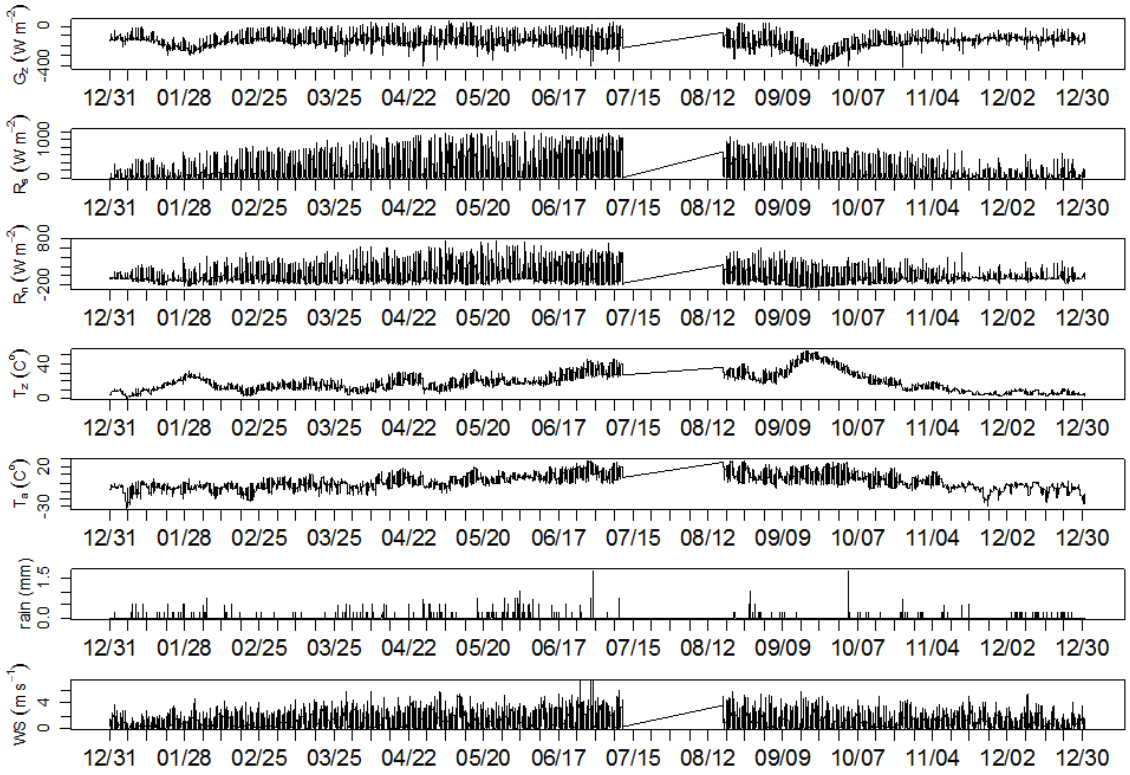

Fig. A.2 Plot showing raw data collected at CR3000 site during 2010, including ground heat flux (G_z), incoming solar radiation (R_s), net radiation (R_n), soil temperature at 0.05 m (T_z), air temperature (T_a), rain, and wind speed (WS).

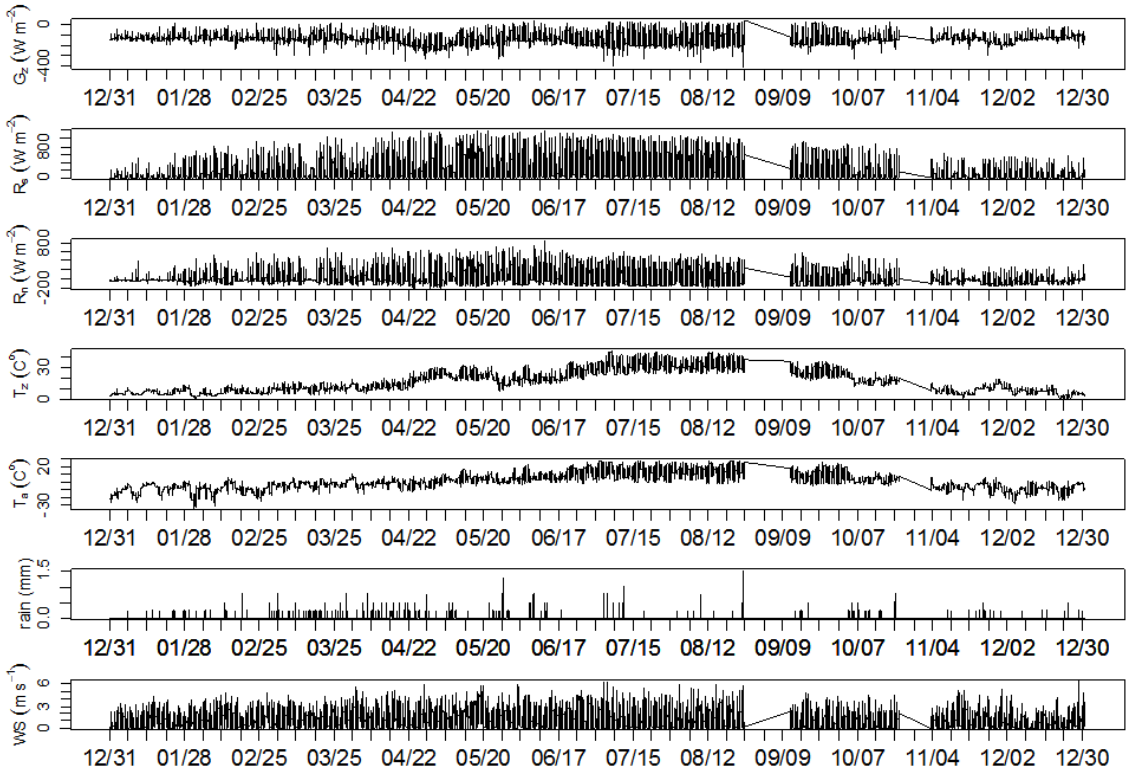

Fig. A.3 Plot showing the raw data collected at CR3000 site during 2011, including ground heat flux (G_z), incoming solar radiation (R_s), net radiation (R_n), soil temperature at 0.05 m (T_z), air temperature (T_a), rain, and wind speed (WS).

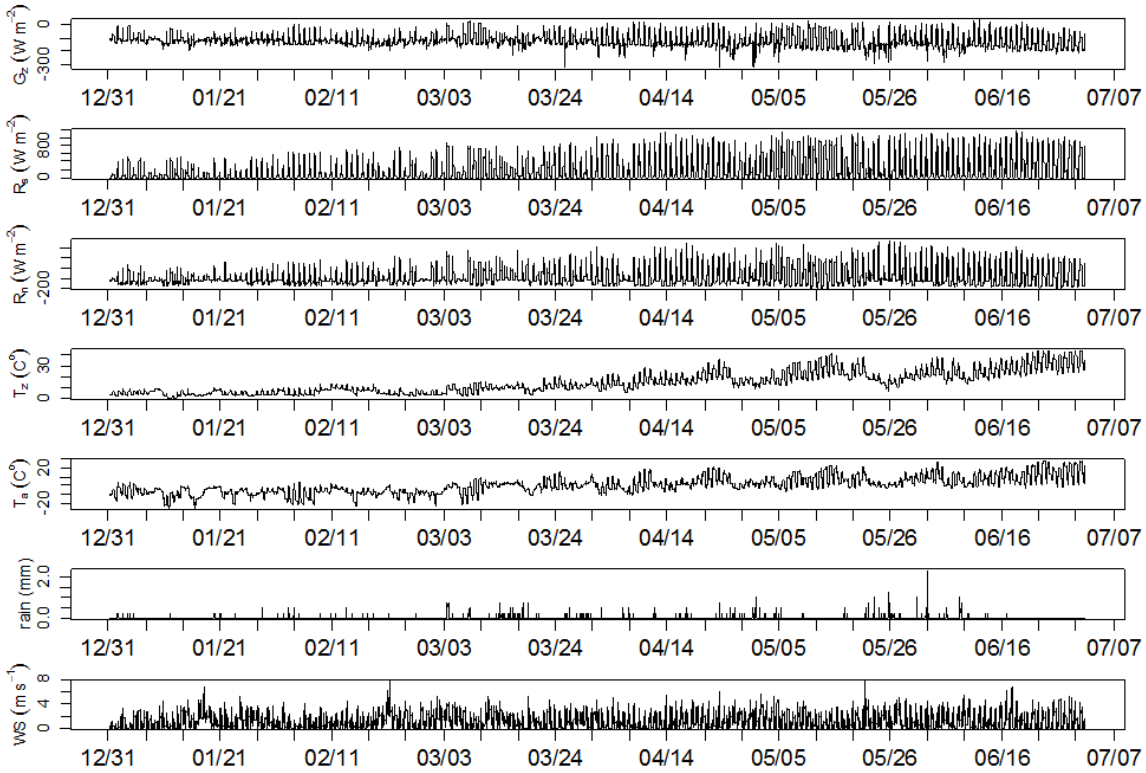

Fig. A.4 Plot showing the raw data collected at CR3000 site during 2012, including ground heat flux (G_z), incoming solar radiation (R_s), net radiation (R_n), soil temperature at 0.05 m (T_z), air temperature (T_a), rain, and wind speed (WS).

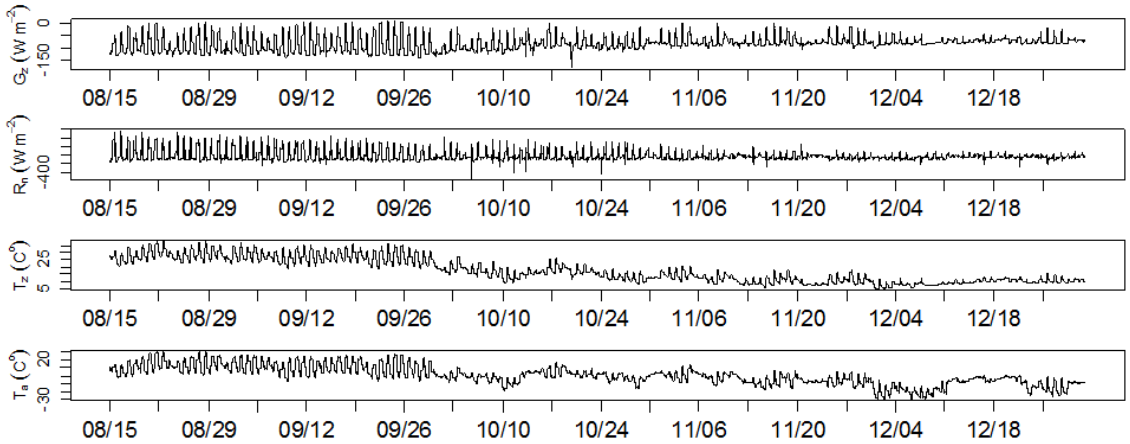

Fig. A.5 Plot showing raw data collected at CR1000 Side in 2009, including ground heat flux (G_z), net radiation (R_n), soil temperature at 0.05 m (T_z), and air temperature (T_a).

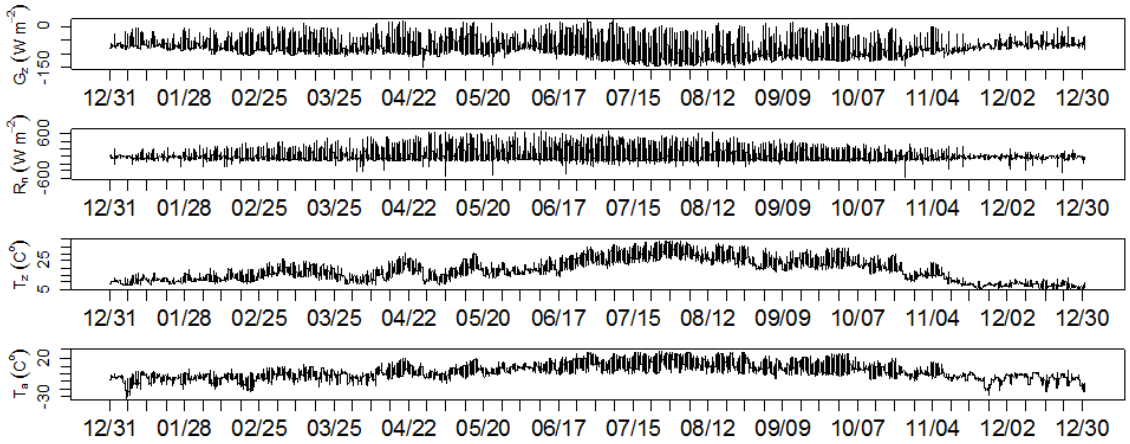

Fig. A.6 Plot showing raw data collected at CR1000 Side in 2010, including ground heat flux (G_z), net radiation (R_n), soil temperature at 0.05 m (T_z), and air temperature (T_a).

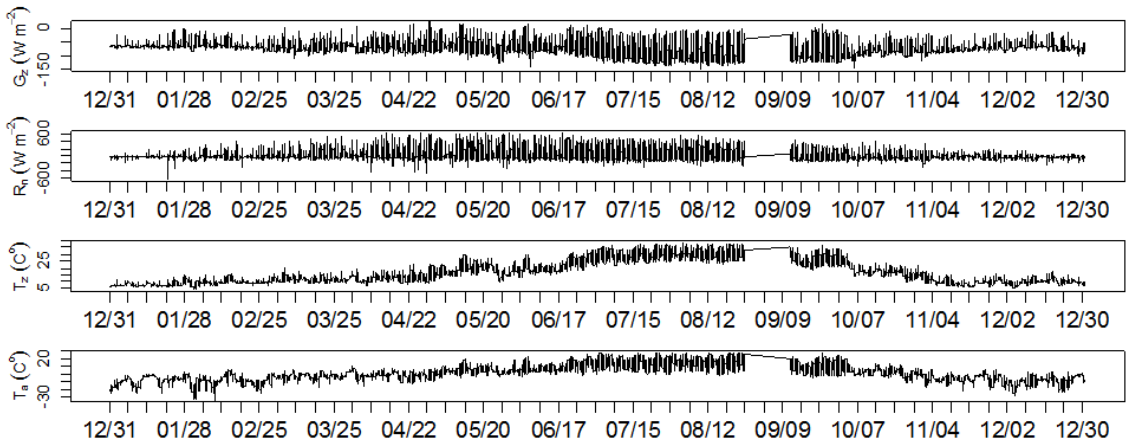

Fig. A.7 Plot showing raw data collected at CR1000 Side in 2011, including ground heat flux (G_z), net radiation (R_n), soil temperature at 0.05 m (T_z), and air temperature (T_a).

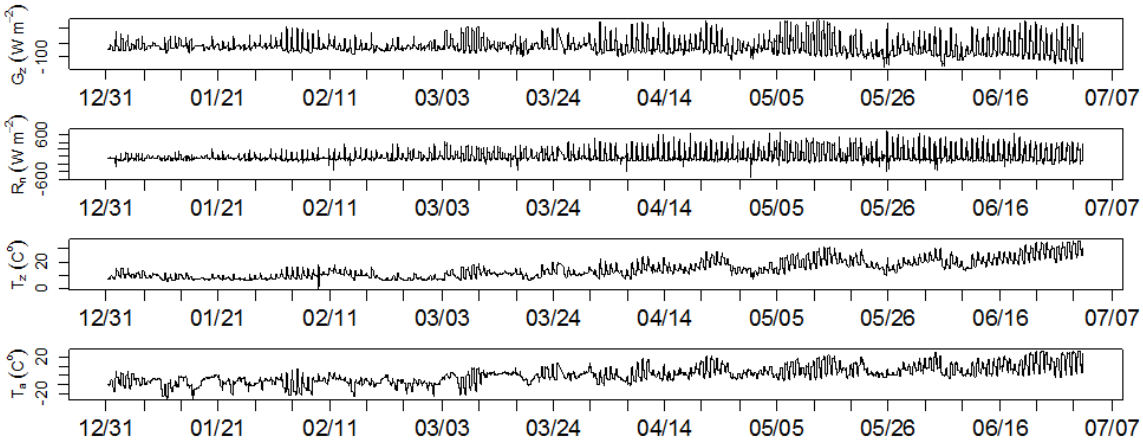

Fig. A.8 Plot showing raw data collected at CR1000 Side in 2012, including ground heat flux (G_z), net radiation (R_n), soil temperature at 0.05 m (T_z), and air temperature (T_a).

CURRICULUM VITAE

Ruba A. M. Mohamed
ruba.mohamed@aggiemail.usu.edu

EDUCATION:

Ph.D. Civil and Environmental Engineering **(May 2017)**
Water Resources Engineering (3.67/4.0 GPA)
Utah State University

Dissertation: A Study of Spatial and Temporal Mass and Heat Transport of Hydrothermal Features in Norris Geyser Basin, Yellowstone National Park

Adviser: Christopher M. U. Neale

M.Sc. Degree, Civil and Environmental Engineering **(May 2012)**
Environmental Engineering (3.7/4.0 GPA)
Utah State University

Thesis: Integration of Water-Column and Benthic Processes and Their Effect on Dissolved Oxygen Fluctuations in Small Northern Utah Streams.

Adviser: David K. Stevens

B.S., Civil Engineering (**Nov. 2003)**
University of Khartoum (6.02/10.00 GPA)

Research Skills:

- Remote Sensing Imagery processing and analysis
- GIS Application and programing
- Time Series analysis
- Coding with Matlab and R
- Technical Writing
- Technical Presentation
- Hydrologic Modeling
- Physical Hydrology
- Groundwater Engineering
- Volcanology
- River Basin Planning and Management
- Organic and inorganic environmental analysis
- Research Design
- Environmental data analysis
- Physical/Chemical environmental processes
- Water quality and pollution

- Biological environmental processes

SOFTWARE:

- QUAL2K (River and Stream Water Quality Model)
- WEAP (Water Evaluation and Planning Model)
- MODFLOW (Groundwater simulation model)
- GMS (Groundwater and subsurface simulation model)
- HEC-RAS (Hydrologic Engineering Centers River Analysis System Model)
- AutoCAD
- Microsoft Office

EMPLOYMENT:

- Graduate Research Assistant (June 2009-May 2017)
  Civil and Environmental Engineering Department. Utah State University, Utah, USA
- Design Engineer (Designed reinforced-concrete deep foundations) (Jun. 2006-Jun. 2007). Bauer Spezialtiefbau GmbH. Khartoum, Sudan
- Site Engineer (Supervised construction of deep foundation) (Oct. 2004-Jun. 2006). Bauer Spezialtiefbau GmbH. Khartoum, Sudan
- Teaching Assistant (Strength of Materials and Sanitary Engineering courses) (Nov. 2003-Oct. 2004). Department of Civil Engineering. University of Khartoum, Khartoum, Sudan

INTERNSHIP EXPERIENCE:

- Water Quality Educator Intern (May 2015 – Aug 2015), College of Natural Resources, Utah State University
- Deep Foundation Design Intern (Jun. 2005-Jul. 2005), Bauer Spezialtiefbau GmbH. Schrobenhausen, Germany
- Structural Design and Cost Estimation Intern (Mar. 2004-Jul. 2004), Newtech Industrial & Engineering Group Ltd. Khartoum, Sudan
- Sanitary Engineer Intern (Oct. 2003-Dec. 2003), Khartoum Company for Water Services. Khartoum, Sudan
- Site Engineer Intern (Jul. 2001-Aug. 2001), DAL Construction Group Co. Ltd. Khartoum, Sudan

PUBLICATIONS:

- Mohamed, R., and Stevens, D. K.: Primary Production in Northern Utah Streams as Related to Nutrients Availability and Turbidity (in preparation)
- Mohamed, R., and Stevens, D. K.: Comparison of stream metabolism parameters estimates from field measurements and dissolved oxygen modeling (in preparation)
- Mohamed, R., Neale, C., Jaworowski, C., Heasler, H., Ban, H., and Geli, H., 2017: Using High Resolution Thermal Infrared Images to Estimate Radiant Geothermal Flux from Measurement of Conductive Heat Flux at Norris Geyser Basin, Yellowstone National Park. The Journal of Volcanology and Geothermal Research (submitted).
- Mohamed, R., Jones, S., Neale, C.: Numerical Simulation of Soil Water and Heat Transport with Vapor Flow in Bare Ground in Norris Geyser Basin, Yellowstone National Park (in preparation)
- Mohamed, R., Neale, C., Jaworowski, C., Heasler, H.: Monitoring Spatial and Temporal Changes in Hydrothermal Features at Norris Geyser Basin (in preparation)
- Xing, C., Mohamed, R., Ban, H., Geli, H.: An Approach to Obtain Soil Heat Flux at the Surface from Buried Heat Flux Sensor Measurement (in preparation)

CONFERENCE PAPERS:

- Mohamed, R. A., and Stevens, D. K., 2011: Measuring Stream Productivity for the Purpose of a TMDL Assessment. Spring Runoff Conference, Logan, UT
- Mohamed, R. A., Stevens, D. K., 2011: A Study of the Comparison of Primary Production with In-situ Monitoring in Northern Utah Streams. Water Environment Association of Utah (WEAU) Annual Conference, Saint George, UT
- Mohamed, R. A., Neale, C., Jaworowski, C, and Heasler, H. 2014: Estimation of Temporal and Spatial Heat Budget in Norris Geyser Basin. Spring Runoff Conference, Logan, UT
- Mohamed, R. A., Neale, C., and Jaworowski, C., 2014: Heat Budget Monitoring in Norris Geyser Basin, Yellowstone National Park. AGU Fall Meeting, San Francisco, CA
- Mohamed, R. A., Alafifi, A., Salha, A., Bitar, A., Jarret, K., McFarland, M., 2015: Upgrade of South Davis Sewer District in Northern Utah. Water Environment Association of Utah (WEAU) Annual Conference, Saint George, UT
- Mohamed, R. A., Alafifi, A., Salha, A., Bitar, A., Jarret, K., McFarland, M., 2015: Alternative Solutions to Remove Total Phosphorous from The Effluent of South Davis Sewer District. Water Environment Federation's Annual Technical Exhibition and Conference (WefTec), Chicago, IL

- Mohamed, R. A., Jones, S., and Neale, C., 2016: Numerical Modeling of Coupled Heat Transport and Liquid Water and Water Vapor Flow in Geothermally Heated Ground at Norris Geyser Basin. AGU Fall Meeting, San Francisco, CA

OTHER RESEARCH PROJECTS:

- Analyses of Pharmaceuticals in Logan Lagoons, Utah
- Modeling the Temperature of Logan River and First Dam in Logan, Utah
- Management of Dams Operation in the Nile River Basin. Africa
- Design Alternatives to Remove Total Phosphorous from the Effluent of South Davis Sewer District North Plant. Utah

VOLUNTEER AND OUTREACH EXPERIENCE:

- UWW (Utah Water Reach): Certified Tier 2 volunteer used advanced monitoring techniques following the Utah DWQ Standard Operating Procedures including collection and handling of water quality samples, Stream flow/discharge measurements, E. coli IDEXX sampling and analysis, Macroinvertebrate sampling and handling, Photo point monitoring
- STAR (Student Teaching Arithmetic and Reading): volunteered to tutor math and reading at Hillcrest Elementary School.
- SWE (Society of Women Engineers): Professional Development Coordinator for the school year 2015-2016. Volunteered with Expanding Your Horizons (EYH) outreach activities for grades 6-9 elementary school girls.

ACADEMIC AWARDS AND GRANTS:

- The Ivanhoe Foundation Scholarship (2011 and 2012): The grant was awarded to selected thesis with economically feasible method that can be applied in developing countries to help solve water quality problems.
- AGU Travel Grant (2014): The grant was awarded to selected students from under representative countries whose abstracts submitted to AGU showed scientific merit to application reviewers in applicable fields.
- Blue Goes Green Grant (2015): The grant was awarded to the best proposal submitted to upgrade the toilet flush system in Utah State University's campus to a sustainable system
- WEAU Student Design Competition (2015): Scored first place in the State of Utah with

a team of students from Utah State University for designing alternative solutions to remove total phosphorous from the effluent of South Davis Sewer District North Plant in northern Utah.